TRANSPORT AND STORAGE PROPERTIES OF INHOMOGENEOUS ROCK SYSTEMS

A DISSERTATION

SUBMITTED TO THE DEPARTMENT OF GEOPHYSISCS

AND THE COMMITTEE ON GRADUATE STUDIES

OF STANFORD UNIVERSITY

IN PARTIAL FULFILLMENT OF THE REQUIREMENTS

FOR THE DEGREE OF

DOCTOR OF PHILOSOPHY

By

Philippe Marie Doyen

April 1987

ABSTRACT

In the first chapter of this thesis, a review is given of models of flow through natural porous media. The emphasis is on the relationship between the pore space geometry and the effective transport properties of rocks.

In the second chapter, an extension of an existing self-consistent effective medium theory is developed to evaluate the bulk d.c. electrical conductivity and the hydraulic permeability of water saturated rocks in terms of the frequency distribution of pore and crack conductances in the void space. Based on this theory, the transport properties of Fontainebleau sandstone are calculated as a function of porosity from a quantitative study of the evolution of the pore space morphology. Throat and pore size distributions are constructed with an image analyser from digitized thin sections, and the variations of permeability and conductivity with porosity are estimated, based on the change of the ratio between two characteristic lengths which are inferred from the size histograms.

In the third chapter, the transport and elastic properties of igneous rocks under hydrostatic confining stresses are analysed in terms of their spectra of crack dimensions. First, the decrease of the transport coefficients, resulting from the elastic closure of the cracks under pressure, is expressed self-consistently by averaging the crack hydraulic and electrical contributions over the unknown crack spectrum. In addition, the pressure-dependent compressibility is shown to depend on the average over the spectrum of the square of the crack cross-sectional length. Next, the maximum entropy inversion method is used to infer the spectrum of crack dimensions in Westerly granite from measurements under confining stresses of its permeability, conductivity and compressibility. Finally, the predicted spectrum is compared to the distribution of crack dimensions observed with a scanning electron microscope and it is interpreted in light of a

model of growth of the microfissures during cooling of the granite.

In the last chapter, a linear mean square prediction method, integrating well measurements and seismic interval velocity data, is studied for the areal mapping of the porosity in oil-bearing rock formations. This estimation technique, based on spatial correlation functions, is first tested on a numerically simulated reservoir model. It is then applied to predicting the spatial distribution of the porosity in an oil-bearing channel-sand in Alberta. It is shown that the correlation-based method performs better than the conventional least-squares fitting procedures derived from the cross-plot velocity against porosity.

TABLE OF CONTENTS

Chapter 4:

Porosity Mapping From Seismic Velocity Data,

An Approach Based on Spatial Correlation Functions

CHAPTER 1:

MODELS OF FLOW IN POROUS MEDIA:

A REVIEW

Abstract

Models of flow through porous sandstones and trough cracked rocks are reviewed. The emphasis is on the relationship between the microstructure and the hydraulic and d.c. electrical properties of rocks as measured at the scale of laboratory samples. The microgeometric characteristics of rocks relevant to the transport phenomena are first underlined. Next, some methods of calculation of the effective conductivity and permeability are reviewed. Variational methods are briefly discussed. The dilute and mean field approximations for transport in continuous media are then reviewed. Percolation models are also discussed. Finally, network models of the pore space are presented and some theories of transport through disordered lattices are reviewed.

Introduction

In this introductory chapter, we review some theoretical models of flow through natural porous media. We will emphasize the shortcomings of the models which result mainly from unrealistic assumptions about the microgeometry of rocks.

In the next two chapters of this thesis, we will be concerned with some important aspects of fluid and electrical current flows through porous media. In particular, we will consider a steady state, low Reynolds number flow of an incompressible viscous fluid trough a porous medium. Locally, at the scale of a fluid particle moving in the pore space, the flow is governed by the linearized Navier-Stokes equations and by the continuity equation:

$$\mu \nabla^2 \mathbf{v} = \nabla p \tag{1}$$

$$\nabla . \mathbf{v} = 0 \tag{2}$$

where μ is the viscosity of the fluid and p and $\mathbf{v}$ are respectively the pressure and velocity at one point in the fluid. The boundary condition requires that the

velocity vanishes at the pore-grain interface. At the scale of a macroscopically homogeneous and isotropic rock sample whose size is large compared with the pore dimensions, the flow is governed by Darcy's law which states that the average volume flow rate per unit area $<\mathbf{q}>$ is proportional to the imposed uniform average pressure gradient $<\nabla \mathrm{p}>$:

$$<\mathbf{q}> = -\frac{\kappa^*}{\mu} <\nabla \mathrm{p}> \tag{3}$$

The constant of proportionality κ^* is the scalar effective permeability independent of $<\mathbf{q}>$ and $<\nabla \mathrm{p}>$. κ^* depends only upon the geometry of the porous medium.

We will also consider the steady state d.c. conduction of electricity through porous rocks whose void phase is fully saturated with an electrolyte of conductivity σ_f . The grain phase will be assumed to be homogeneous with conductivity σ_g . The electrostatics equations governing the flow of current are:

$$\mathbf{j} = \sigma \mathbf{E} \tag{4}$$

$$\mathbf{E} = -\nabla \mathrm{V} \tag{5}$$

$$\nabla . \mathbf{j} = 0 \tag{6}$$

where $\mathbf{j}$, $\mathbf{E}$, and V are respectively the current density, the electric field and the potential at one point in the material where the conductivity σ is equal to σ_f or σ_g . Equations (4), (5) and (6) are equivalent to Laplace's equation $\nabla^2 V = 0$ which must be solved in the two phases with boundary conditions requiring the continuity of the voltage and of the normal component of the current density at the pore-grain interface. At the macroscopic level, Ohm's law relates the average current density $<\mathbf{J}>$ to the applied uniform average voltage gradient $<\nabla \mathrm{V}>$:

$$<\mathbf{J}> = -\sigma^* <\nabla \mathrm{V}> \tag{7}$$

where σ^* is the effective d.c. electrical conductivity.

One of the basic question which will be addressed in this thesis is the relation

between the effective transport coefficients κ^* and σ^* and the rock microgeometry. In principle, κ^* and σ^* can be calculated by solving the appropriate equations of motion provided that the boundary conditions are specified. In practice, the complexity of these conditions which must be imposed at the irregular pore surface renders this approach intractable. More realistically, the problem is approached by relating the transport coefficients to a small number of measurable parameters which characterize statistically the microstructure of rocks.

The study of transport through porous rocks may be treated as a special case of transport in inhomogeneous systems. In fact, most of the theoretical work reviewed below is based on studies of the transport properties of composites [Beran, 1968; Batchelor, 1974] and of disordered systems in solid state physics [Elliott et al. 1973, Garland and Tanner, 1978; Ziman, 1979; Shklovskii and Efros, 1984]. Rocks form a special class among heterogeneous systems. In the next section, we review a few characteristics of rocks which are relevant to the study of their transport properties. We insist especially on the microstructural properties which explain the macroscopic behaviour of rocks.

Microgeometry and transport properties

In clean sandstone or in crystalline rocks like granite, the electrical conductivity of the minerals σ_g is usually several orders of magnitude smaller than the conductivity σ_f of the brine saturating the pore space. To a good approximation, a rock saturated with an electrolyte can be considered as a conductor-insulator mixture.

There is a great contrast between the geometry of conducting and nonconducting phases in rocks. The insulating solid phase is a continuous aggregate of crystals

with polyhedral shapes. The electrolyte filled void phase participating in the flow usually forms a multiply connected branching network between the grains which remains continuous to porosities much lower than expected from simple mixture models. The continuity of the void phase is explained by the formation processes of rocks. In low porosity cracked rocks like granite, the connectedness of the void phase follows from the large density and from the large specific surface area of the sheetlike cracks which were formed during cooling at the boundaries between the mineral grains [Kranz, 1983]. In sandstones, the continuity of the pore space at low void volume fraction suggests that the porosity reducing mechanisms acting during diagenesis do not completely block the microscopic flow channels. Self-limiting models of cementation and compaction have been proposed to explain the persistence of the pore space continuity at low porosity [Sen et al., 1981]. More recently, Cohen and Anderson [1985] explained this feature by the existence during diagenesis of an antisintering regime characterized by an anomalously low interfacial energy at the pore-grain boundary.

In general, the geometry of the pore system where the flow of fluid and the flow of electricity are confined is strongly heterogeneous. This heterogeneity reflects the irregularity of the grain-pore interface. The randomness of the pore wall geometry is in contrast with many composites where the boundaries between phases has a regular shape. In the study of rock transport properties, one of the most difficult problem is to give a compact statistical chararcterization of the microgeometry in terms of measurable parameters. A binary random variable $\omega(\vec{x})$ can be defined which takes a value 1 at a point $\vec{x}$ in the pore space and a value 0 at a point in the solid phase [Matheron, 1967; Beran, 1968]. The porous material is then in principle completely characterized by the joint spatial probability density function $p_{\omega_1\omega_2\cdots\omega_n}(\vec{x}_1,\vec{x}_2,\cdots,\vec{x}_n)$ when, for $n\to\infty$, the n points are allowed to describe independently all positions in the material. In

practice, beyond the second order moments, the spatial statistics are not accessible to measurements. Experimental measurements of two-point correlation functions were performed by Berryman and Blair [1986] and by Thompson et al. [1987]; the latter authors showed that the pore surface of some sandstones is fractal.

We will see that correlation functions are not very useful as far as the transport properties are concerned. More relevant information is obtained by considering the sizes of pores and cracks in rocks. The pore geometry of sandstones is characterized by an alternation of large open regions called pore chambers and narrow passages called pore throats. Pore casts, thin section microscopy and mercury porosimetry clearly demonstrate the existence of a large range of pore dimensions in sandstones [Dullien, 1979; Pittman, 1984]. Scanning electron micrographs of cracked rocks like granite show that the spectrum of crack dimensions may extend over several orders of magnitudes [Sprunt and Brace, 1974; Hadley, 1976]. When attempting to describe quantitatively the variability of pore dimensions in sandstones, one faces the problem that there is no natural definition the size of a pore [Scheidegger, 1960; Dullien, 1979]. In the next chapter, we will introduce some simple concepts of mathematical morphology [Matheron, 1967; Serra, 1982] which are useful to quantify the complex microstructure of sandstones.

In addition to being microscopically heterogeneous, rocks are also strongly heterogeneous on a macroscopic scale. Within a single sandstone formation. spatial variations of core permeability by many powers of ten are the rule rather than the exception. Jacquin [1964] found that the permeability of a sequence of samples of Fontainebleau sandstone varies by a factor of almost 10^4 while the porosity ϕ ranges only from 5 to 35%. In general it is not the porosity which

determines the transport properties but the size of the narrowest passages through which the fluid must percolate. Models of fluid flow involving only ϕ as parameter are generally not adequate. However, within a rock formation characterized by a uniform diagenetic history, there usually exists a good empirical correlation between κ^* or σ^* and ϕ [Jacquin 1964; Bourbier and Zinszner, 1985]. In particular, clay-free detrital sedimentary rocks originating from the same formation and fully saturated with an electrolyte of conductivity σ_f are known to obey approximately Archie's law. This empirical law relates the bulk conductivity σ^* to some power of the porosity:

$$\sigma^* \approx \sigma_f \phi^m \tag{8}$$

where Archie's exponent m depends on the texture of the porous material. The degree of cementation is known to affect the value of the exponent [Parkhomenko, 1967], m varying from about 1 for loosely packed granular materials to more than 2 for well consolidated rocks. For unconsolidated sands, m also depends on the shape of the grains [Jackson et al., 1978]. We will see that many models, most of them unsatisfactory, have been proposed to explain this empirical power law. The significance of Archie's law is twofold. First, it implies that the pore space remains continuous to very low porosity. As we have already mentioned, this absence of percolation thershold is in contradiction with most simple mixture models. Secondly, the regularity of macroscopic behaviour suggested by this empirical law indicates that a continuous evolution of the pore structure must take place during diagenesis. Archie's exponent may be interpreted as the signature of the diagenetic history common to rock samples coming from a uniform formation. In the second chapter, the origin of Archie's law will be explained from the evolution of the pore space morphology as a function of porosity.

Starting from a statistical description of rock structure at the microscale, we will

model the transport properties at the scale of laboratory samples whose volume is typically of the order of a few cm^3. At this laboratory scale, which is large with respect to the dimensions of the grains but small with respect to the dimensions of a rock formation, the porous medium can be considered as a statistically homogeneous system characterized by constant bulk properties independent of the sample volume. As the correlation length -typically of the order of the grain size- characterizing the fluctuations of the pore dimensions is small compared with this intermediate scale, the concept of effective transport coefficient is meaningfull. When studying flow at the scale of an aquifer, the permeabilities measured on cores appear as punctual properties of the medium. The problem of composing those local measurements to characterize transport at the scale of the aquifer is beyond the scope of our study. At this last scale, the correlation length characterizing the spatial variations of the local permeability is typically on the order of the dimensions of the aquifer field and the concept of effective permeability breaks down.

Rocks are not only characterized by geometrical disorder but also by a great chemical complexity of the mineral phase. The interactions of fluids with the chemically heterogeneous pore surface are not well understood at the present time. Clays, which are found in many sandstones, have complex conduction mechanisms which act in parallel with electrolytic conduction trough the fluid. We will limit ourselves to clean materials for which surface conduction can be neglected.

Models of flow in porous media

In view of the empirical correlation existing in many rock formations between the transport coefficients and ϕ and considering the fact that the porosity ϕ is one of the most easily measurable rock parameter, many flow models have been

proposed whose behaviour can be summarized in terms of ϕ and a few additional parameters. Unfortunately, except for some simple arrangements of the two phases or for small contrast between the properties of the two constituents in rocks, we will see that the porosity alone is not enough to determine the transport coefficients. We now review some of these models insisting on the underlying geometrical assumptions.

Perturbation and Variational Methods

When the two phases of an isotropic and statistically homogeneous system have approximately the same electrical conductivity, perturbation theory [Beran, 1968] can be used to express σ^* in terms of the volume fraction and conductivity of the two phases. In most aquifer or crystalline rocks, the ratio between the conductivity of the fluid and that of the minerals is very large ($\sigma_f / \sigma_g \geq 10^{10}$) and perturbation methods can not be applied.

Variational techniques [Hashin and Shtrikman, 1962; Beran, 1968] exist to derive bounds on the effective conductivity σ^* from the phase conductivities and volume fractions. For a rock whose solid matrix is composed of insulating mineral grains ($\sigma_g = 0$), Hashin-Shtrikman upper bound is given by:

$$\sigma^* \leq \sigma_f \frac{2\phi}{(3-\phi)} \tag{9}$$

This bound is the most restrictive one which can be derived from the porosity. This stems from the fact that a material can be constructed which has exactly the conductivity predicted by the bound. In (10), the equality would hold if the rock was formed by arbitrarly sized spherical grains coated with the electrolyte in such a way that the ratio between the inner and outer radius of all the composite spheres is equal to $(1-\phi)^{1/3}$. The geometry of this assembly of coated spheres may be close to that of fluid saturated unconsolidated sands where the contacts between quartz grains are pointlike. Unfortunately, Hashin-Shtrikman lower

bound, which is constructed by permuting the role of the two phases, reduces to zero for insulating minerals. The wide contrast existing between the conductivity of the two phases in rocks implies that the bounds involving only ϕ are useless and that more detailed information about the microgeometry is necessary to calculate the effective conductivity. Variational principles can be also used to derive improved bounds involving higher order spatial statistics [Beran, 1968]. A recent review by Berryman [1985] shows that Prager and Doi upper bounds which involve two-point correlation functions do not give a much more accurate estimate of the hydraulic permeability in the porosity range $\phi \leq 30\%$ of practical interest.

Dilute and effective media approximations

In many manufactured two phase composites, one phase is in the form of discrete inclusions dispersed in a homogeneous matrix of another material. Simple mixing laws involving only the volume fractions and the properties of the two phases predict accurately transport in such systems [Beran, 1968; Batchelor, 1974]. In the dilute suspension approximation, one calculates for example the effective electrical conductivity of a two phase disperse system from the perturbation of the uniform electrical field which results from the introduction of a single inclusion in the homogeneous matrix of the second phase [Bottcher, 1973]. By contrast with simple composites, the pore space of sandstone can not be described as regularly shaped void inclusions dispersed in a solid matrix. Except in some carbonates or in some volcanic rocks, the pore space is generally completely interconnected.

Many binary metallic alloys are random aggregates of round equidimensional grains where the two phases play a symmetrical role. The transport properties of such symmetrical binary random mixtures are described accurately from effective

media approximations (EMA) [Bruggeman, 1935; Landauer, 1952; Landauer, 1978]. In Bruggeman's mean field approximation for the effective conductivity, the electrical interactions between grains are taken approximately into account by treating the medium surrounding one grain as a uniform medium whose conductivity is that of the mixture. The field outside each grain is then written as the sum of the uniform applied external field and a dipole field which results from the apparent suface charge at the boundary between the grain and the hypothetical uniform matrix of conductivity σ^* surrounding it. As a self-consistency condition, the spatial average of the dipole fields is required to vanish. In the special case of a a mixture of insulating and conducting grains, this self-consistency condition becomes:

$$\sigma^* = \frac{1}{2}\sigma_f \ (3\phi - 1) \tag{10}$$

and the mixture is predicted to behave as an insulator when the fraction ϕ of conducting material with conductivivity σ_f is reduced to a critical value $\phi_c = 1/3$. Experimentally, a uniformely mixed binary aggregate where conducting and insulating regions have the same average shape and size is expected to exhibit a conductivity percolation threshold when the fraction of conducting material is about $\phi_c = 15\%$ [Zallen, 1983]. The EMA clearly overestimates the critical volume fraction. In addition, the onset of conductivity is known to be described by $\sigma^* \alpha(\phi - \phi c)^t$ where the exponent t is larger than one. In a wide range of concentration above ϕ_c, the EMA is known to perform very well [Kirkpatrick, 1973], but as most consolidated rocks have a porosity much smaller than 30%, this approximation is not very useful. We have seen that the EMA treats the two components in the mixture on a symmetrical basis. To be applicable, the geometry of the composite must also exhibit that symmetry between conducting and non conducting regions. We have mentioned above that cracks and pores are generally shettlike openings which bear no morphological

resemblance to the round mineral grains.

To explain the absence of percolation thershold manifest in most rocks, Sen et al. [1981] have proposed a rock model formed by a self-similar assembly of water coated grains. Using a differential effective medium approximation they showed that this model yields Archie's law with an exponent which depends on the aspect ratio of the grains. Their model may provide with a good representation of a fluid saturated assembly of sand grains with a very wide distribution of size but it is hard to see its relation to the geometry of most sandstones. In addition, for consolidated sedimentary rocks, there is no experimental evidence of a relationship between the grain shape and Archie's exponent. Archie's law must instead be understood from the geometry of the flow channels.

Percolation models

Greenberg and Brace [1969] and Shankland and Waff [1974] constructed large analog regular networks of resistors to model the conductivity in fluid-bearing rocks. Identifying the porosity with the fraction of conducting resistors, they simulated a porosity reduction by random removal of conducting branches. In this picture, identical to the bond percolation model [Shante and Kirkpatrick, 1971; Kirkpatrick, 1973; Stauffer, 1985], a percolation threshold arises when the porosity is reduced to a critical value, $\phi_c \approx 1.5/z$, z being the coordination number of the three-dimensional network. Below ϕ_c, the network is disconnected and the rock is an insulator. Shankland and Waff [1974] explained the conduction of current in low-porosity rocks by the presence of an unrealistically large value of the coordination number. In fact, the model proposed by Shankland and Waff fails to consider the contrasting geometrical characteristics of the two phases in rocks. As conducting and nonconducting branches play a symmetrical role in the bond percolation model, this simple

lattice idealization is only appropriate to model a continuous medium where conducting and insulating regions exhibit the same symmetry like in the random binary mixture described above.

One approach to maintaining the continuity of the electrolyte-filled pore space to lower porosity consists in introducing spatial correlation between resistor values in the random network [Webman et al., 1975]. However, in our discussion of the variational methods, we have already indicated that two-point correlation functions do not contain enough information to describe the complicated and contrasting shapes of cracks and grains in rocks.

In a continuous medium, the thershold volume fraction ϕ_c of conducting material depends strongly on the geometry and arrangement of the two phases [Zallen, 1983; Deutscher et al., 1983]. In igneous rocks, the connectedness of the void phase follows from the large density of cracks and from their sheetlike geometry. The study of the onset of connectivity has been extended to objects whose shapes are closer to that of the thin elongated cracks observed in rocks [Pike and Seager, 1974; Balberg et al, 1984]. A recent work [Charlaix et al., 1984] shows that the percolation threshold of a random assembly of flat disks of radius r, thickness $\tau \ll r$, and density N_V per unit volume is attained when the dimensionless product $N_V\ r^3$ reaches some critical value. So, disk-shaped cracks distributed randomly in a rock matrix can form a continuous network with a vanishingly small porosity contribution, $\phi \propto N_V r^2 \tau$, provided that τ is small enough.

In contrast to the strong dependence of the critical volume fraction ϕ_c on the geometry of the mixture, the behaviour of the conductivity in the vicinity of this critical concentration is expected to be independent of the details of the geometry of the constituents. Close to ϕ_c, a power law relationship is expected to hold between σ^* and the fraction of conducting material ϕ:

$$\sigma^* \alpha \sigma_f (\phi - \phi_c)^t \qquad (11)$$

where the conductivity exponent depends only on the dimensionality of the system. Balberg [1985] identified this exponent, which is about 1.9 for a three dimensional system, with Archie's exponent. The critical power law holds only in the direct vicinity of ϕ_c which is close to zero for most rocks. One must expect a cross-over to a mean field regime in the wide porosity range over which Archie's law is usually claimed to hold. In hot pressed calcite [Bernabe and Brace, 1982] and in some sandstones [Bourbier and Zinszner, 1985], there is experimental evidence for the existence of such a cross-over at porosities of the order of a few percents. However, the experimental exponents are larger than the conductivity exponent t which was derived from the study of discrete-lattice percolation networks. Halperin et al. [1985] constructed a 'swiss cheese' continuum model where transport takes place between spherical holes randomly distributed in a conducting matrix. They showed that the critical exponents characterizing the onset of conductivity and permeability are larger than the exponent t for the standard lattice percolation model.

Network models of the pore space

Most of the flow models reviewed untill now attempted to represent the continuous medium formed by the void and solid phase in rocks. Some of these models have the shortcoming that they do not yield a connected pore system at low porosity. In addition, they do not account for the strong heterogeneity of the pore structure. A better approach is to concentrate on modelling only the pore space where the flow is confined.

The simplest and oldest pore space model is probably the Kozeny-Carman equivalent channel model (for a review see Paterson [1983] or Walsh and Brace [1984]). In the simplest version of this model, the pore space is replaced by a

single channel of length L_t larger than the length L of the sample in the flow direction. The cross-section of this equivalent channel has a constant shape and an area proportional to the porosity of the sample. The permeability and the electrical conductivity can be readily expressed in terms of ϕ, the specific surface area S_v and the tortuosity $(L/L_t)^2$ as:

$$\kappa^* = c\ (\frac{L}{L_t})^2\ \frac{\phi^3}{S_v{}^2} \tag{12}$$

$$\sigma^* = \sigma_f\ (\frac{L}{L_t})^2\ \phi \tag{13}$$

where c is a constant which depends on the cross-sectional shape of the channel. By combining (12) and (13), the tortuosity is usually eliminated and an expression is obtained for the permeability which depends only on S_v, ϕ and σ^*/σ_f which are all parameters that can be measured independently [Berryman and Blair, 1986]. From the irregularity of the pore walls, it follows that widely different values of S_v can be obtained depending on the size of the probe which is used in measuring the internal surface of the pore space [Faris et al.,1985; see also ch. 2 of this thesis]. This constitutes a severe limitation for any model involving the specific surface area. Traditionally, in deriving Kozeny-Carman model, the multiple connectivity of the pore space is completely neglected. In the next chapter, we will see that this model is also applicable in the limit of a branching but microscopically homogeneous pore system as shown in figure 7 (chapter 2). In general however, the behaviour of most rocks deviates from that predicted from Kozeny-Carman equations. In particular, for rocks obeying Archie's law, the exponent m is generally significantly larger than 1.

More recent pore space models accounting for its branching nature involve three-dimensional networks of cracks and pores. The most widely used approach which takes advantage of the insulating nature of the mineral phase consists in representing the fluid saturated pore space by an interconnected network of

conducting branches. The conductance values of the branches depend upon the dimensions of segments of pores and cracks [Fatt, 1956; Madden, 1976]. The nodes in the network represent the junctions between three or more pore channels. The differential equations governing the flow (eqs. (1), (2) or (4) to (6)) are then replaced by a system of linear finite difference equations for the voltage or fluid pressure, v_i at each internal node i in the network (where there is no external source of current or of fluid):

$$\sum_j g_{ij} \ (v_i - v_j) = 0 \tag{14}$$

In (14), g_{ij} is the conductance of the microchannel connecting the node i to node j. The above equation is simply Kirchoff's current law which requires that there be no current or fluid accumulation at the junctions between channels. The electrical current in each branch of the network is related to the voltage drop by Ohm's law, $i_{ij} = g_{ij} \ (v_i - v_j)$, where the channel electrical conductance g_{ij} is approximately proportional to the ratio between its mean cross-sectional area and its length, i.e., $g_{ij} \approx \sigma_f \ s_{ij}/l_{ij}$. The flow of fluid is treated analogously by considering the hydraulic conductances of the flow channels.

Madden [1976] calculated numerically the effective conductivity of large regular lattices of random valued conductances, the distribution of which reflects the fluctuations of crack and pore dimensions. Koplik [1982] also performed Monte Carlo simulations of the permeability of large regular lattice arrays of variable-sized channels and variable coordination number. More recently, Seeburger and Nur [1984] investigated numerically the effect of confining pressure on the transport properties of regular arrays of cracks and pores. Long and Witherspoon [1985] studied the permeability of computer-simulated networks of fractures with variable size, orientation, and density.

Several approximate theories exist to relate the distribution of crack and pore

conductances to the bulk transport coefficients. Conductivity and permeability are respectively given by:

$$\sigma^* \approx \frac{1}{l^*} g_e^* \tag{15}$$

$$\kappa^* \approx \frac{1}{l^*} g_h^* \tag{17}$$

where g_e^* and g_h^* are some characteristic average of the local electrical and hydraulic conductance distributions. In (15) and (16), l^* is some microscopic length characteristic of the 3-di lattice supporting the flow process. This length is readily calculated for periodic arrays with constant coordination number [Koplik, 1982]. In chapter 2, we will see how to calculate l^* for topologically disordered networks.

From Monte Carlo simulations and from the analysis of a system of embedded networks, Madden [1976] concluded that the geometric mean of the local conductances generally gives a reasonable estimate of g^*. He also showed that Archie's law can be reproduced by using broad electrical conductance distributions. Wong et al. [1984] studied numerically the conductivity of 3-di network of tubes which were shrunk by different amounts so as to generate very skewed conductance distributions which obey Archie's law. It is easy to show that the conductance distributions in their model are asymptotically log normally distributed [Aitchison and Brown, 1963; Montroll and Shlesinger, 1984] and that the characteristic local conductance g_e^* is the geometric mean and not the most probable value as they claimed. In fact, the geometric mean is an exact result for a two-dimensional flow with a log normal conductance distribution [Matheron, 1967; Marchant and Gabillard, 1975].

Kirkpatrick [1973] extended Bruggeman's effective medium approximation to describe the transport properties of random valued conductance networks. In this approximation, the field interactions between cracks or branches in the

network are approximately accounted for by considering that each crack is part of a homogeneous network which models the average effect of all the other cracks. Monte carlo data [Kirkpatrick, 1973; Koplik, 1981] show that this approximation is very accurate except for conductance distributions which are strongly weighted near very low values (e.g., for a system close to a percolation thershold) or for distribution which are extremely broad. This network version of the EMA has been applied by several authors [Shankland and Waff, 1974; Madden, 1976; Koplik, 1982; Koplik et al., 1984] to model the transport properties of rocks.

When the local conductance distribution spreads over more than about four orders of magnitude, the critical percolation path method [Ambegaokar et al., 1971; Seager and Pike, 1974; Shklovskii and Efros, 1984] may be used. In this last approximation, the characteristic conductance g^* which determines the bulk conductivity or the permeability of the rock is taken to be of the order of the largest local conductance value g_c^* such that the subset of cracks and pores with $g \geq g_c^*$ forms a connected network spanning the entire system. By measuring the thershold capillary pressure in a mercury injection experiment, Katz and Thompson [1987] determined the value of the critical conductances g_c^*, for the flow of fluid and for the flow of current and they sucessfully predicted the transport coefficients of several sandstones.

The applicability of the EMA and of the critical path method is limited to networks where the conductance values are spatially uncorrelated. In practice, this is not a limitation for rocks where the correlation length is of the order of the grain size [Berryman and Blair, 1986] which is also approximately equal to the length of the branches in the network idealization of the pore space.

Except in the differential EMA [Sen et al., 1981], all the theories reviewed above

treat all cracks or pores on equal footing independently of their length scale. Madden [1983] studied embedded crack networks and he used a renormalization group technique to relate the onset of conductivity and fracture to the crack population. This technique treats more rigourously the interactions between cracks at different scales.

References

Aitchison, J., and J.A.C. Brown, *The Lognormal Distribution,* Cambridge Univ. Press, Cambridge, 1963.

Ambegaokar, V., B.I. Halperin, and J.S. Langer, Hopping conductivity in disordered systems, *Phys. Rev. B, 4,* 2612-2620, 1971.

Balberg, I., C.H. Anderson, S. Alexender, and N. Wagner, Excluded volume and its relation to the onset of percolation, *Phys. Rev. B, 30,* 3933-3943, 1984.

Balberg, A., Excluded-volume explanation of Archie's law, *Phys. Rev. B Communications, 33* 3618-3620, 1986.

Batchelor, G.K., Transport properties of two-phase materials with random microstructure, *Ann. Rev. Fluid Mech., 6,* 227-255, 1974.

Beran, M.J., *Statistical Continuum Theories,* p. 424, Interscience, New York, 1968.

Bernabe, Y., W.F. Brace, and B. Evans, Permeability, porosity and pore geometry of hot pressed calcite, *Mech. of Materials, 1,* 173-183, 1982.

Berryman, J.C., Bounds on fluid permeability for viscous flow through porous media, *J. Chem. Phys., 82,* 1459-1467, 1985.

Berryman, J.G., and S.C. Blair, Use of digital image analysis to estimate fluid permeability of porous materials I. Application of two-point correlation functions, J. Appl. Phys., 60, 1930, 1986.

Bottcher, C.J.F., *Theory of Electric Polarization,* pp. 377, 2^d edition, Elsevier, Amsterdam, 1973.

Bourbier, T., and B. Zinszner, Hydraulic and acoustic properties as a function of porosity in Fontainebleau sandstone, *J. Geophys. Res., 90,* 11524-11532, 1985.

Bruggeman, D.A.G., Berechnung verschiedener physikalisher konstanten von heterogenen substanzen, *Annalen der Physik, 5,* 636-664, 1935.

Charlaix, E., E. Guyon, and N. Rivier, A criterion for percolation threshold in a random array of plates, *Solid State Communications, 50,* 999-1002, 1984.

Cohen, M.H., and M.P. Anderson, Geometry and topology of porous media, in *The chemistry and physics of composite media,* edited by M. Tomkiewicz and P.N. Sen, p. 1-9, The Electrochemical Society, Pennington, New Jersey, 1985.

Deutscher, G., A. Kapitulnik, and M. Rappaport, Percolation in metal-insulator systems, in *Percolation Structures and Processes,* edited by G. Deutscher, R. Zallen and J. Adler, p. 207-228, Annals of the Israel Physical Society, v.5, Israel Physical Society, 1983.

Dullien, F.A.L., *Porous Media, Fluid Transport and Pore Structure,* Academic, New York, 1979.

Elliot, R.J., J.A. Krumshansl, and P.L. Leath, The theory and properties of randomly disordered crystals and related physical systems, *Rev. Mod. Phys., 46,* 465-543, 1974.

Faris, S.R., D.E. Woessner, and J.C. Melrose, Surface area data for sandstones with low clay mineral content - a comparison of results obtained by different techniques, in *The chemistry and physics of composite media,* edited by M. Tomkiewicz and P.N. Sen, p. 271-281, The Electrochemical

Society, Pennington, New Jersey, 1985.

Fatt, I., The network model of porous media: III. Dynamic properties of networks with tube radius distribution, *Trans. AIME, 207,* 164, 1956.

Garland, J.C., and D.B. Tanner, *Electrical Transport and Optical Properties of Inhomogeneous Media,* AIP Conf. Proc., 40, American Institute of Physics, New York, 1978.

Greenberg, R., and W.F. Brace, Archie's law for rocks modeled by simple networks, *J. Geophys. Res., 74,* 2099-2102, 1969.

Hadley, K., Comparison of calculated and observed crack densities and seismic velocities in Westerly granite, *J. Geophys. Res., 81,* 3484-3494, 1976.

Halperin, B.I., S. Feng, and P.N. Sen, Differences between lattice and continuum percolation transport exponents, *Phys. Rev. Letters, 54,* 2391-2394, 1985.

Hashin, Z., and S. Shtrikman, A variational approach to the theory of the effective magnetic permeability of multiphase materials, *J. Appl. Phys., 33,* 3125-3131, 1962.

Jackson, P.D., D. Taylor-Smith, and P.N. Stanford, Resistivity-porosity-particle shape relationships for marine sands, *Geophysics, 41,* 1250-1268, 1978.

Jacquin, C., Corrélations entre la perméabilité et les caractéristiques géométriques du grès de Fontainebleau, *Revue de l'IFP, 19,* 921-937, 1964.

Katz, A.J., and A.H. Thompson, Prediction of rock electrical conductivity from mercury injection measurements, *J. Geophys. Res., 92,* 599-607, 1987.

Kirkpatrick, S., Percolation and conduction, *Rev. Mod. Phys., 45,* 574-588, 1973.

Koplik, J., On the effective medium theory of random linear networks, *J. Phys. C, 14,* 4821-4837, 1981.

Koplik, J., Creeping flow in two-dimensional networks, *J. Fluid Mech., 119,* 219-247, 1982.

Koplik, J., C. Lin, and M. Vermette, Conductivity and permeability from microgeometry, *J. Appl. Phys., 56,* 3127-3131, 1984.

Kranz, R.L., Microcracks in rocks: a review, *Tectonophysics, 100,* 449-480, 1983.

Landauer, R., The electrical resistance of binary metallic mixtures, *J. Appl. Phys., 23,* 779-784, 1952.

Landauer, R., Electrical conductivity in inhomogeneous media, in *AIP Conf. Proc., 40,* edited by J. Garland and D. Tanner, p. 2-43, American Institute of Physics, New York, 1978.

Long, J.C.S., and P.A. Witherspoon, The relationship of the degree of interconnection to permeability in fracture networks, *J. Geophys. Res., 90,* 3087-3098, 1985.

Madden, T.R., Random networks and mixing laws, *Geophysics, 41,* 1104-1125, 1976.

Madden, T.R., Microcrack connectivity in rocks: a renormalization group approach to the critical phenomena of conduction and failure in crystalline rocks, *J. Geophys. Res., 88,* 585-592, 1983.

Marchant, J., and R. Gabillard, Sur le calcul d'un réseau résistif aléatoire, *C.R. Acad. Sc. Paris B, 261-264, 1975.*

Matheron, G., *Eléments Pour Une Théorie Des Milieux Poreux,* p. 166, Masson, Paris, 1967.

Montroll, E.W., and M.F. Shlesinger, On the wonderful world of random walks, in *Nonequilibrium Phenomena II From Stochastics to Dynamics,* edited by J.L. Lebowitz and E.W. Montroll, p. 5-117, Studies in Statistical Mehanics, vol. XI, North-Holland Physics Publishing, Amsterdam, 1984.

Parkhomenko, E.I., *Electrical Properties of Rocks,* p. 314, Plenum Press, New York, 1967.

Paterson, M.S., The equivalent channel model for permeability and resistivity in fluid-saturated rock - a re-appraisal, *Mech. of Materials, 2,* 345-352, 1983.

Pike, G.E., and C.H. Seager, Percolation and conductivity: A computer study. I., *Phys. Rev. B, 10,* 1421-1446, 1974.

Pittman, E.D., The pore geometries of reservoir rocks, in *Physics and Chemistry of porous media,* AIP Conf. Proc., 107, p. 1-19, edited by D.L. Johnson and P.N. Sen, American Institute of Physics, New York, 1984.

Scheidegger, A.E, *The Physics of Flow Through Porous Media,* p. 353, University of Toronto Press, Toronto, 1960.

Seager, C.H., and G.E. Pike, Percolation and conductivity: a computer study. II, *Phys. Rev. B, 10,* 1435-1446, 1974.

Seeburger, D.A., and A. Nur, A pore space model for rock permeability and bulk modulus, *J. Geophys. Res., 89,* 527-536, 1984.

Sen, P.N., C. Scala, and M.H. Cohen, A self-similar model for sedimentary rocks with application to the dielectric constant of fused glass beads, *Geophysics, 46,* 781-795, 1981.

Serra, J., *Image Analysis and Mathematical Morphology,* p. 610, Academic, London, 1982.

Shankland, T.J., and H.S. Waff, Conductivity in fluid-bearing rocks, *J. Geophys. Res., 79,* 4863-4868, 1974.

Shante, V.K.S., and S. Kirkpatrick, An introduction to percolation theory, *Adv. Phys., 20,* 325-357, 1971.

Shklovskii, B.I., and A.L. Efros, *Electronic Properties of Doped Semiconductors.* Springer-Verlag, Berlin, 1984.

Sprunt, E.S., and W.F. Brace, Direct observation of microcavities in crystalline rocks, *Int. J. Rock Mech. Min. Sci. Geomech. Abstr., 11,* 139-150, 1974.

Stauffer, D., *Introduction to Percolation Theory,* p. 124, Taylor & Francis, London, 1985.

Thompson A.H., A.J. Katz, and C.E. Krohn, The microgeometry and transport properties of sedimentary rock, to appear in *Adv. Phys.,* 1987.

Webman, I., J. Jortner, and M.H. Cohen, Numerical simulation of electrical conductivity in microscopically inhomogeneous materials, *Phys. Rev. B, 11,* 2885-2891, 1975.

Wong, P.Z., J. Koplik, and J.P. Tomanic, Conductivity and permeability of rocks, *Phys. Rev. B, 30* 6606-6614, 1984.

Zallen, R., *The Physics of Amorphous Solids,* p. 297, Wiley, New York, 1983.

Ziman, J.M., *Models of Disorder,* p. 492, Cambridge University Press. Cambridge, 1979.

CHAPTER 2

PERMEABILITY, CONDUCTIVITY AND PORE GEOMETRY OF FONTAINEBLEAU SANDSTONE

Abstract

Based on an effective medium approximation, the hydraulic permeability and the d.c. electrical conductivity of Fontainebleau sandstone are predicted from a quantitative study of the pore space morphology. A series of epoxy-impregnated thin sections of Fontainebleau sandstone was prepared from cores with porosity ranging between 5 and 22%. Using an image analyser, throat and pore size distributions were constructed from the digitized and segmented microsections. For each sample, the transport coefficients are calculated from the ratio of two characteristic lengths which are inferred directly from the experimental histograms. The change of permeability with porosity is predicted within a factor of two without any adjustable parameters. The variations of the transport properties with porosity are interpreted from the contrasting path of evolution of pores and throats during diagenesis. Large pore chambers alternate with narrow passages in Fontainebleau sandstone. With decreasing porosity, some of the large pores remain stable while the throats gradually shrink and are finally eliminated. It is shown that the effective medium approximation reduces to Kozeny-Carman formulas in the limit of a microscopically homogeneous pore system. As a result of the heterogeneity of its pore space, the behaviour of Fontainebleau sandstone deviates from Kozeny-Carman predictions.

Introduction

The d.c. electrical conductivity and the hydraulic permeability of clay-free sandstone are known to be controlled by the geometry of the pore space. In the recent past, using image processing techniques, many researchers have tried to estimate the transport properties of sedimentary rocks from geometrical characteristics of the pore complex measured from thin sections. In weakly

cemented sandstone, the pore complex appears in 2-di as a series of long chains of large pore chambers connected by narrow passages. Rink and Schopper [1978] used erosion and dilation [Matheron, 1967] to remove the small bridges relating the pores and to subdivide the 2-di pore system into a collection of compact 'void particles' with simple convex shapes. Using the 'bundle of tubes' model, they then calculated the permeability from pore size histograms constructed by measuring the dimensions of the artificially individualized pore elements. Order of magnitude agreement was obtained between measured and predicted permeability values. Rink and Schopper [1978] failed to realize that the narrow throats which they partially eliminated from the 2-di pore complex actually control the flow properties. In addition, they did not take advantage of the information about the pore volume topology carried by the connectedness of the 2-di pore complex.

Using digitized scanning electron microscope images of rock microsections, Berryman and Blair [1986] estimated porosity and specific surface area from measured two-point spatial correlation functions. These two parameters were then combined with known values of the electrical formation factor to predict permeability from Kozeny-Carman formulas (eqs (12) and (13), ch. 1). The specific surface area is directly proportional to the slope of the two-point correlation function evaluated at the origin (see for example Matheron [1967]). In a digitized image, a point is replaced by a pixel and the slope of the correlation function at the origin tends to increase with decreasing pixel size or with increasing microscope magnification. This feature has been studied in geostatistics where it is related to the 'regularization' of correlation functions under change of length scale [Journel and Huijbregts, 1978]. Berryman and Blair [1986] changed the magnification of the microscope to estimate the specific surface area of different samples. This makes the accuracy of their permeability

predictions hard to evaluate.

Pore casts of sandstone [Pittman, 1984] reveal that the void space forms a complicated multiply connected 3-di volume and it is not clear a priori that a 2-di section across a rock sample contains enough information about the geometry and topology of the pore system to predict the macroscopic flow properties. Using image analysis techniques, Ehrlich et al. [1984] studied empirical correlations between permeability and various geometrical attributes of the pore space extracted from digitized and segmented thin sections of sandstone. They were able to show that a significant degree of correlation exists between the macroscopic transport properties and geometrical features like throat size histograms or 2-di pore connectedness. One important conclusion of their work is that the changes in the 3-di pore structure which control the changes in the transport coefficients are reflected in the 2-di microsections.

Following the work of DeHoff et al. [1971] in metallography, Lin and Cohen [1982] studied the topology of the pore space from a series of closely spaced and parallel microsections of rocks. More recently, Koplik et al. [1984] constructed a network model of the pore space from serial sections of one sample of Massillon sandstone. Based on an effective medium theory, their prediction of permeability was off by a factor of 10.

In the studies reviewed above, no systematic attempt was made to predict the transport properties of a sequence of rock samples originating from the same formation but differing by their degree of cementation. As the theoretical predictions involve measuring several parameters from the microsections, the sparseness of the data makes it difficult to assess the validity of the proposed models. This study is based on a sequence of samples of Fontainebleau

sandstone with porosity spanning a large range. Based on an extension of an existing effective medium approximation (EMA), the variations of the transport coefficients as a function of porosity are estimated from a quantitative study of the evolution of the pore structure morphology as seen in planar microsections.

Laboratory measurements were made of the permeability and conductivity of a sequence of 7 samples of the sandstone with the porosity ranging from 5 to 22 %. The Fontainebleau sandstone was choosen because the large variation of ϕ is achieved without any change of composition or of grain size. Fontainebleau sandstone is made exclusively of well sorted quartz grains with diameters between 150 and 300 μm and cemented by silica [Jacquin, 1964; Bourbier and Zinszner, 1984]. Epoxy-saturated thin sections of the sandstone were prepared for each of the 7 samples and the microstrutural evolution of the pore structure was studied as a function of porosity using an image analyser. The quantitative study of the pore complex is based on the construction of pore and throat size distributions which characterize the fluctuations of the dimensions of the pore chambers and pore necks observed in the rock. The size histograms are constructed by implementing an erosion operation on digitized images of the 2-di microsections of the sandstone. The conductivity and permeability of each sample are then predicted from two characteristic lengths which are inferred from the experimental histograms.

Quantitative Analysis of The Pore Space Geometry

In order to study the pore structure of Fontainebleau (FTB) sandstone, samples of the rock were first impregnated with a blue dyed epoxy. Then, thin sections were prepared and imaged with a conventional transmitted light petrographic microscope coupled to an image analyser via a TV camera [Ehrlich et al., 1984]. Figure 1 shows the evolution of the pore space morphology of Fontainebleau

sandstone as a function of porosity, ϕ. Each figure is a binary image resulting from the segmentation [Crabtree et al., 1984] of a digitized thin section scene into porous (black) and nonporous (white) regions. It is known that the void phase in FTB forms a intergranular network which remains continuous to very low porosity [Bourbier and Zinszner, 1985]. In 2-di sections, the pore complex of high porosity samples appears as a collection of subnetworks with convoluted shapes extending over a large fraction of the scene. The weekly cemented quartz grains are clearly visible as the contact areas are small. In tighter samples, the 2-di pore system is formed by smaller and more compact porosity regions surrounded by aggregates of well cemented quartz grains. All the views reveal the occurrence of *pore chambers of large dimensions connected by smaller pore necks*. This feature is typical of sandstone [Dullien, 1979; Pittman, 1984]. The large pores account for most of the rock porosity while the dimensions and connectedness of the pore throats control the flow properties. For large ϕ, the thin sections show long chains of pore chambers connected by relatively large necks. When ϕ is reduced, the 2-di pore system appears much less well connected; large pores remain visible but the interconnecting throats are more narrow and less numerous.

Our predictions of the hydraulic permeability and the d.c. electrical conductivity are based on a quantitative analysis of the pore structure as seen in microsections. This analysis contains two steps. First, a study of the *metric properties* is necessary to characterize the shape and size of the porous zones. Secondly, an analysis of the *connectivity* of the pore system is required.

Size Distributions from Erosion

Some authors [Rink and Schopper, 1978; Dullien, 1979] tried to describe the pore space of sandstone as an ensemble of 'void particles' with simple convex

shapes dispersed in the rock matrix. For ellipsoidal or spherical particles, a natural definition of size is possible and the distribution of particle dimensions can be recovered from the apparent size distribution measured in a planar section across the porous material [Underwood 1970; Ripley, 1981]. The images presented in figure 1 show that this model is inappropriate to describe the complex morphology of the pore system. A more general concept of size based on a mathematical operation called *erosion* [Matheron, 1967; Serra 1982] is useful to study the complicated geometry of the pore space [Delfiner et al., 1972; Ehrlich et al., 1984]. Erosion leads naturally to defining *pore and throat size distributions* independently of the existence of pores with simple convex shape.

When describing the morphology of irregularly shaped objects, it must first be recognized that there is no objective definition of size. The size is always defined by comparing the object to be measured with a reference figure which is called a structuring element [Serra, 1982] in mathematical morphology. In this study, the reference object is a circle C of variable radius r. The 2-di pore complex observed in a scene (the black areas in figure 1) can be divided into a collection of connex components which are called the pore elements of the scene. The size of each pore element is defined as the radius of the largest circle which remains wholly included within that element. The pore size distribution is then defined as the proportion of pore elements as a function of their size r. Experimentally, this distribution is measured by implementing an erosion operation with an image analyser [Delfiner, 1972; Ehrlich, 1984]. The concept of erosion is illustrated with one pore element in figure 2. The eroded pore element is by definition composed of all the points of the original element where it is possible to implant the reference figure C in such a way that it remains fully included in that element. Letting the radius r of the eroding circle increase, the pore element shrinks more and more. The size of the pore

element is simply the radius r for which the eroded element reduces to a point. As r increases, the pore element may split into several parts. The size of the pore element always refers to the radius of the eroding circle for which the last fragment of the element disapears from the eroded pore system. Figure 3 shows the evolution of the digitized pore structure of FTB sandstone under progressively more severe erosion with a digital structuring element whose shape approaches that of a circle. In a digital implementation, eroding the pore system may be described intuitively as an operation which removes more and more layers of pixels from the boundaries of the pore elements. A pore size histogram is constructed by counting the number of connex components of the original pore system which vanish at each erosion as the radius of the structuring element is increased by steps of one pixel.

Figure 3 demonstrates that erosion artificially cuts the small bridges relating the pore chambers. Rink and Schopper [1978] used erosion for the purpose of subdividing the 2-di pore system into a collection more compact pore elements whose size can be described by conventional measurements. Here, following Ehrlich et al. [1984], we take advantage of the erosion operation to construct a throat size histogram. By counting the number of throat breaks occuring at each erosion with the expanding circle, a throat size distribution is calculated which gives the proportion of throats as a function of their radius.

Figures 4 and 5 show respectively the experimental throat and pore size frequency distributions measured for two samples of FTB, one with ϕ=22.1% (figure 4a and 5a) and the other with ϕ=7.5% (figure 4b and 5b). These histograms were obtained by measuring the size of several thousands pore elements and pore throats in an image area of about $2cm^2$. The histograms were constructed by pooling together the observations corresponding to about

30 views from a single thin section. The statistical homogeneity of the pore structure was checked by comparing the histograms obtained independently from several thin sections coming from the same rock sample. The spacing between bins in the histograms and their width is equal to $5\mu m$ which is also the size of one pixel in the digitized images. The first bin in figure 4 gives the relative number of throats which are between 5 and $10\mu m$ wide. Smaller throats probably exist in FTB. However, capillary pressure curves [Bourbier and Zinszner, 1984] show that the connected pathways controlling the flow properties of FTB are established at capillary pressures which correspond to throats with $2r \geq 5\mu m$. It follows that the small throats unresolved in the digitized images contribute only marginaly to the flow. Figure 4a shows that the throat size distribution spans more than two orders of magnitude in a high porosity sample of FTB. As the hydraulic conductance of a cylindrical throat is proportional to the fourth power of its radius, the broadness of the size distribution implies that the throat conductance distribution spreads over many orders of magnitude [Katz and Thompson, 1987]. In a low ϕ sample (figure 4b), the large throats have disapeared and most throats have a diameter between 5 and 20 μm. In contrast to the variability of the throat size histograms, there is no marked evolution in the pore size distributions with decreasing ϕ. The very small pores ($2r \leq 10\mu m$ observed in figure 1 are not considered in the histograms. Most of these micropores appearing as small isolated black patches within the quartz grains are artifacts resulting from the missegmentation of small metal particles produced during polishing of the microsections. To avoid parasitic phenomena related to the presence of a great number of small particles of a foreign material, one can construct a size distribution giving the fractional area of the pore space as a function of the radius r of the structuring element [Matheron, 1967; Delfiner, 1972; Ehrlich et al., 1984]. But, when modelling the

transport coefficients of rock, it is important to consider histograms 'in number'. This stems form the fact that flow is controlled by the number of occurrence of porous zones with a given conductance in the fluid pathways and not by the volume of such zones.

In summary, erosion is useful to characterize the complex morphology of sandstone pore structure which can not be studied with standard size measurements. This method provides with a natural measure of the size distribution of the pore chambers and pore necks which are typically observed in sandstone. Erosion is also useful to characterize the topology of the pore complex.

Topological Properties of The Pore Space

Early models of flow in porous media were based on systems of capillary tubes connected in series or in parallel. These models contradict all the experimental evidences like SEM studies or pore casts of sandstone which [Pittman, 1984] reveal that the pore space has a complex 3-di branching structure with large connectivity. The pore space microsections dispayed in figure 1 show clearly that the reduction of ϕ in FTB is accompanied by a reduction of the connectedness of the pore system. Using erosion, we will characterize semi-quantitatively changes in the pore space coordination number.

Rigourously, the topology of the 3-di pore structure can be studied from a series of closely spaced parallel microsections [DeHoff et al., 1972; Lin and Cohen, 1982]. In particular, serial sectioning can be used to visualize the *skeleton* of the pore space which is a network of branches and nodes having the same connectivity as the pore structure. Mathematically, there are several ways of defining the skeleton [See for example Serra, 1982; Barrett and Yust, 1970]. We

can imagine a fire propagating at uniform speed from all points at the pore-grain interface toward the inside of the pore volume [Duda and Hart, 1973]. The pore space is so retracted onto a network of branches which is by definition the locus of all the points which are reached simultanuously by fire fronts coming at least from two points on the original pore-grain boundary. Figure 6 illustrates a simple pore structure and its skeleton.

One important topological parameter for the flow properties is the *average coordination number* $\bar{z}$ which is defined as the average number of branches meeting at one node in the skeleton. $\bar{z}$ is not directly measurable from a single planar section across the rock. In 2-di, the pore system of large ϕ samples appears as a collection of long chains of pore chambers singly connected by pore throats. In low ϕ samples, the number of throats per pore element is much smaller. The changing 2-di pore connectedness is indicative of the decrease in the 3-di connectivity of the pore space skeleton with decreasing ϕ. We define a pseudo 2-di coordination number as the total number of throats divided by the total number of pore elements in a thin section and we make the ad hoc assumption that this pseudo coordination number is proportional to $\bar{z}$. We also assume that the FTB sample which has the largest porosity (ϕ=22%) has a coordination number $\bar{z}$=6. This last number is a reasonable estimate for the weekly cemented high ϕ sample. For broad conductance distributions, the transport coefficients calculated from the effective medium approximation are not strongly sensitive to a small change in the coordination number. This implies that our prediction of the transport properties will not be very sensitive to the error in evaluating $\bar{z}$ from the microsections.

Transport Properties and Pore Space Geometry

In this section, using an effective medium approximation (EMA), the hydraulic

permeability and the d.c. electrical conductivity of sandstone are expressed in terms of the throat and pore size distributions.

As the solid framework of sandstone is composed of insulating mineral grains, the transport of current is limited to the pore space, supposed to be fully saturated with a conducting fluid. The permeability κ^* and the conductivity σ^* both reflect the geometry and the topology of the network of microscopic flow channels in sandstone. In principle, κ^* or σ^* can be calculated by solving Navier-Stokes equations or Laplace's equation in the pore space. Practically, this approach is hopeless because of the complexity of the conditions to be imposed at the irregular pore-grain boundaries.

To estimate the transport coefficients, we consider instead an *equivalent homogeneous rock* which, by construction, has the same pore space skeleton and the same κ^* or σ^* as the real rock sample. The homogenized rock is obtained by smoothing the irregularities of the pore-grain interface. The equivalent pore system is constructed, as shown in figure 7, by expanding uniformely the flow channels about the branches forming the skeleton of the pore network. This dilation operation gives rise to a microscopically homogeneous pore system where all the flow channels are cylinders with the same radius r^*. It is clear that there exists a value of r^* for which the homogenized rock has the same σ^* or κ^* as the real microscopically heterogeneous rock sample (figure 6). Based on an effective medium approximation, the values of r^*, r_h^* and r_e^*, defining respectively the equivalent homogeneous networks for the flow of fluid and that of the electrical current, will be determined self-consistently from the experimental throat size distribution.

Locally, at the scale of a pore throat in the heterogeneous pore space, the Poiseuille's flow is determined by the pore channel hydraulic conductance which

is defined as the ratio between volumetric flux and fluid pressure drop across the channel. Similarly, the flow of current in a throat depends on its electrical conductance defined as the ratio between current and voltage drop across the throat. The local conductances are a function of the throat geometry. For straight cylindrical throats of length l and circular cross-section of radius r, the

$$g_e(r) = \sigma_f \frac{\pi r^2}{l} \tag{1}$$

$$g_h(r) = \frac{\pi}{8} \frac{r^4}{l} \tag{2}$$

where σ_f is the electrical conductivity of the fluid filling the tube. In what follows, it is assumed that the throat length l is approximately constant. This assumption is not essential in our derivation but in well-sorted sandstones, the length of the narrow throats connecting the pore-chambers is a constant of the order of the grain diameter. We also neglect the small pressure or voltage drops occuring in the large pore chambers interconnected by the narrow pore throats. The flow properties of the heterogeneous pore space are then determined by the throat size distribution $n_t(r)$ which characterizes the variability of the local conductances in the disordered pore system.

In the equivalent homogeneous pore space (figure 7), all the flow channels have the same hydraulic and electrical conductances given by $g_h^* \alpha r_h^{*4}$ and $g_e^* \alpha r_e^{*2}$. The characteristic throat radius r_e^* which determines the electrical conductivity of the equivalent homogenized rock is obtained self-consistently from $n_t(r)$ as follows. A throat channel with radius r_e^* in the homogeneous pore structure is replaced by a throat with radius r. Across that throat, this replacement induces a voltage perturbation with respect to the voltage distribution in the homogeneous pore space. By construction, the homogenized rock must have the same σ^* as the heterogeneous rock sample. As a self-consistency condition, we then require that the perturbation introduced by the throat with radius r

averages to zero over the throat size distribution $n_t(r)$. This condition gives r_e^* as the solution of the following implicit equation [Kirkpatrick, 1973]:

$$\sum_r n_t(r) \frac{g_e^*(r_e^*) - g_e(r)}{g_e(r) - (\frac{z}{2}-1)\, g_e^*(r_e^*)} = 0 \qquad (3)$$

The derivation of (3) requires that the pore network supporting the flow process be isotropic and that there be no spatial correlation between the throat radii. The constant length l assigned to all the throats in our model is assumed to be of the order of the correlation length characterizing the fluctuations in the throat channel cross-sectional dimensions. Equation (3) was derived from a regular lattice of randomly variable conductances with constant coordination number z. Numerical simulations [Koplik, 1982] show that for a topologically disordered network, z can be replaced by its average value $\bar{z}$. The throat radius r_e^* and the conductance $g_e^* = \sigma_f \pi r_e^{*2}/l$ increase monotonically with z. In particular, for $z=2$ and $z \to \infty$, (3) reduces respectively to the series and parallel averages. For $z=4$ it is easy to see that r_e^* is the geometric mean when the throat size distribution is log normal. The geometric mean is known to be an exact result for two-dimensional flow with a log normal conductance distribution [Matheron, 1967]. Finally, for a very broad throat size distribution, the self-consistency condition (3) for r_e^* reduces to:

$$\textit{Proportion}\,(r \geq r_e^*) = \sum_{r \geq r_e^*} n_t(r) \approx 2/z$$

which is analogous to the critical path analysis [Ambegaokar et al., 1971] except for the mislocation of the percolation thershold. More will be said about this point in the next chapter.

Using Newton's method for finding the zero of a function, the self-consistency condition (3) can be solved for the characteristic throat radius r_e^* which is by definition the radius of all the flow channels in a homogenized rock having a

conductivity σ^* equal to that of the real rock. Replacing g_e by g_h in (3), a similar condition is obtained for the throat radius r_h^* controlling the flow of fluid. This last radius is different from r_e^* since the power of r appearing in (3) is 4 instead of 2.

In the appendix, it is shown that the conductivity of the homogenized rock with throat radius r_e^* is given by:

$$\sigma^* \approx \sigma_f \ <\cos^2\theta> \ \phi_e^* \tag{4}$$

where $\phi_e^* \alpha \ r_e^{*2}$ is the porosity of the homogenized system, smaller than ϕ and where $<\cos^2\theta>$ is the average square cosine of the angle between the branches of the pore space skeleton and the direction of the spatial average electrical field (figure 7). The tortuosity, $<\cos^2\theta>$, is equal to 1/3 when the branches of the skeleton are randomly oriented. Using a similar derivation, we arrive at the permeability κ^* of the equivalent homogenized rock where all flow channels have a radius r_h^*. It is given by:

$$\kappa^* \approx \frac{1}{8} <\cos^2\theta> \ \phi_h^* \ r_h^{*2} \quad \alpha \ r_h^{*4} \tag{5}$$

By construction of the two equivalent homogenized rocks, (4) and (5) are also respectively equal to the conductivity and permeability of the real heterogeneous sandstone characterized by the throat size distribution $n_t(r)$. Finally, using the equality $\phi_{e,h}^* / \phi = r_{e,h}^{*2} / <r^2>$, where $<r^2>$ is the average of r^2 over the pore size distribution, we obtain for the transport coefficients:

$$\sigma^* \approx \frac{1}{3} \sigma_f \ \phi \ \frac{r_e^{*2}}{<r^2>} \tag{6}$$

and:

$$\kappa^* \approx \frac{1}{24} \phi \ \frac{r_h^{*4}}{<r^2>} \tag{7}$$

where the tortuosity term was replaced by 1/3.

In summary, σ^* or κ^* are expressed in terms of two characteristic lengths. r_e^* and r_h^* are characteristic throat sizes which control respectively the flow of current and the flow of fluid. Both radii are determined self-consistently from the experimental throat size histogram and from the coordination number $\bar{z}$ (equation (3)). These two characteristic lengths have a clear physical meaning. r_e^* (or r_h^*) is defined as the radius of all the flow channels in an electrically (or hydraulically) equivalent homogenized rock constructed by smoothing the irregularities of the pore walls. The second characteristic length appearing in (6) and (7) is $<r^2>^{1/2}$ which is a characteristic pore radius determined from the experimental pore size histogram. The porosity ϕ is directly proportional to $<r^2>$.

It is interesting to mention the limiting case where the pore space of the real rock with porosity ϕ is microscopically homogeneous. By homogeneity, we mean that the actual pore system can be represented, as in figure 7, by a topologically disordered network of cylindrical capillaries with constant radius r_0. Practically this situation arises when the distribution of microchannel dimensions in the rock is very narrow. In that case, the conductivity and permeability are given respectively by (4) and (5) where $\phi_{e,h}^*$ are replaced by the actual porosity ϕ and where $r_{e,h}^*$ are replaced by r_0. Equations (3) and (4) are then identical to Kozeny-Carman equations, i.e., $\sigma^* \approx 1/3\sigma_f \phi$ and $\kappa^* \approx 1/24\phi r_0^2 \alpha\phi^3$. Traditionally (see for example Paterson, 1983 or Walsh et al., 1984), Kozeny-Carman formulas are derived from a model where the multiply connected pore space is replaced by a single cylindrical channel having a cross-sectional area proportional to ϕ and a length L_t larger than the sample length L in the direction of flow. The tortuosity term $(L/L_t)^2$ in that model is equivalent to the term $<\cos^2\theta>$ appearing above. In the appendix, our derivation of equations (3) and (4) is based on the analysis of the trajectory of a fluid particle moving in a

homogeneous interconnected pore system under the effect of a uniform applied external pressure or electrical field. The hypothesis of homogeneity is crucial in the derivation. Only in that case can we make the assumption that the pressure or voltage field are approximately linear everywhere with a gradient equal to the spatial average gradient. The traditional 'equivalent tortuous channel' used in deriving Kozeny-Carman formulas represents accurately the average motion of a fluid particle only when the pore system is homogeneous. In general, the pore space of rock is characterized by a wide distribution of channel dimensions and Kozeny-Carman equations must be replaced by (3) and (4) which are formally identical with the important difference that ϕ is replaced by $\phi^*_{e,h}$, the porosity of an equivalent homogenized rock. ϕ_e^* and ϕ_h^* are always smaller than ϕ and Kozeny-Carman formulas give at best an upper bound on the transport coefficients.

Prediction of The Transport Properties of Fontainebleau Sandstone

Figures 8 and 9 show respectively the evolution of permeability and conductivity as a function of porosity for a sequence of seven samples of FTB. The symbols * represent the experimental measurements. The liquid permeability κ^* was measured with a steady state permeameter. The electrical conductivity σ^* was measured with a four electrodes system at 1, 5 and 20 khz. No significant frequency dependence was observed. For the electrical measurements, the samples were fully saturated with a 10% NaCl brine. The accuracy of all the experimental data is about $\pm 5\%$.

The variation of ϕ from 22 to 5 % is accompanied by a decrease of κ^* and σ^* by a factor of the order of 10^3 and 10^2 respectively. Two porosity ranges can be distinguished with a different porosity-conductivity relationship. For $\phi \geq 10\%$, this relationship can be approximated by $\sigma^* \alpha \phi^{1.9}$, while in the range $\phi \leq 10\%$

we have $\sigma^* \alpha \phi^{3.7}$. A similar porosity-conductivity empirical correlation was observed by Jacquin [1964]. The porosity-permeability relationship can be roughly described by $\kappa^* \alpha \phi^{3.8}$ over the whole range of porosity. In their study of FTB based on a broader and more continuous porosity range, Bourbier and Zinszner [1984] were able to distinguish two ranges of ϕ where the power law relationship between κ^* and ϕ is characterized by a different exponent. They showed that for $\phi >> 10\%$ an exponent slightly larger than 3 is necessary while for $\phi < 10\%$ an exponent larger than 7 is required. The large powers of ϕ in the empirical correlation between porosity and the transport coefficients implies that FTB deviates from Kozeny-Carman predictions. It was shown in the last section that we can only expect $\sigma^* \alpha \phi$ and $\kappa^* \alpha \phi^3$ when the pore strucure is microscopically homogeneous and remains so when the porosity is reduced. Bourbier and Zinszner's measurements show that $\kappa^* \alpha \phi^3$ holds only when the porosity is very high. This follows from the uniformity of the void space between the weekly cemented and equal sized quartz grains. Compaction and cementation of the grains during diagenesis produce an inhomogeneous pore system whose behaviour departs from Kozeny-Carman model. The pore space heterogeneity implies that we have $\sigma^* \alpha \phi_e^*$ and $\kappa^* \alpha \phi_h^{*3}$ where the two 'effective' porosities are smaller than ϕ. Consequently, the empirical correlation between ϕ and the transport coefficients requires larger powers of ϕ than those expected from Kozeny-Carman model. In general, the relationship between porosity and the transport properties can not be described by a simple power law over the whole range of porosity. It is better to interpret the variation of the transport coefficients with ϕ in terms of the evolution of the ratio of the two characteristic lengths appearing in (6) and (7).

The circles in figures 8 and 9 correspond to the prediction of the transport coefficients based on equations (6) and (7). The EMA prediction of κ^* (figure 8)

is accurate within a factor of two over the whole range of porosity. In addition. there is no systematic estimation error. The EMA prediction of the conductivity (figure 9) is accurate at low porosities but σ^* is underestimated for $\phi \geq 10\%$. Globally, considering the two-dimensional nature of the information available from the microsections, the prediction of the macroscopic transport properties is reasonably good. It is worth stressing that the calculation of the predicted values does not involve any adjustable parameter.

The fact that σ^* and κ^* decrease by several orders of magnitudes while ϕ decreases only by less than 30% must be explained by the relative change between r_e^* or r_h^* and $<r^2>^{1/2}$. Table 1 shows that the characteristic throat radii r_e^* and r_h^* decrease much more with ϕ than $<r^2>^{1/2}$. The pore space of FTB is characterized by an alternation between open regions or pore chambers and narrow passages or pore throats. The pore chambers with typical dimension $<r^2>^{1/2}$ account for most of the porosity while the throats with radii r_h^* and r_e^* control respectively the flow of fluid and that of the electrical current. With decreasing porosity, pore chambers and throats evolve differently. The throats shrink considerably and are eventually destroyed as evidenced by the decrease of the coordination number with decreasing ϕ (see table 1). By contrast, some pore chambers are more stable and retain large dimensions even at very low porosity (see figure 1). It is the contrasting path of evolution of pores and throats during diagenesis which determines the change of the transport properties with decreasing porosity. A similar conclusion was reached by Wong et al.[1984] who studied numerically the evolution of a simulated network of channels which were shrinked by different amounts.

Table 1 shows that, as long as ϕ is larger than 10%, our estimate of the coordination number $\bar{z}$ does not decrease substantially. In this high porosity

range, the reduction of the transport coefficients with ϕ is due almost entirely to the gradual reduction of the throat dimensions. Below 10% porosity, $\bar{z}$ decreases dramatically as a result of the closure and eliminitation of the throats. This pinching off of the throats starting at about ϕ=10% correlates well with the cross-over observed in the log-log plot of conductivity versus porosity (figure 9). It is also consistent with the data of Bourbier and Zinszner [1984] which show a cross-over from a small to a large exponent in the permeability-porosity power law at $\phi \approx 10\%$. In an elegant experiment with hot-pressed calcite, Bernabe et al. [1982] observed a rapid decrease of the permeability at low porosity which they also interpreted from the closure of tubular pores.

Table 1 also suggests that at very low ϕ, the pore network becomes singly connected ($\bar{z} \rightarrow 2$). Using serial sectioning analysis, Aigeltinger and DeHoff [1975] were able to quantify the reduction of pore space connectivity occuring during sintering of copper particles. In particular, they showed that the pore space of the sintered mass becomes singly connected when the pore volume fraction is reduced to about 8%. From a single thin section of FTB, one can not infer rigourously the coordination number of the pore space skeleton. It follows that the values of $\bar{z}$ given in table 1 as a function of ϕ must only be considered as indicative of the decaying connectivity of the pore space of FTB. This topological decay of the pore space skeleton is clearly visible in figure 1.

Conclusion

The variations of the hydraulic permeability and of the d.c. electrical conductivity of Fontainebleau sandstone were successfully predicted from a quantitative description of the evolution of the pore space morphology as a function of porosity. The prediction of κ^* or of σ^* is based on the the change with ϕ of the ratio between two microscopic lengths wich are the dimensions of a

characteristic throat and of a characteristic pore. In Fontainebleau sandstone, the large decrease of the transport coefficients accompanying the porosity reduction reveals the differing evolution of pores and throats during diagenesis. The porosity is controlled by pore chambers which retain large dimension even at very low porosity. The flow properties are controlled by the dimensions of the small necks relating the pores. With decreasing porosity, the throats gradually shrink and are eventually eliminated by complete closure when ϕ is reduced below 10%.

Appendix

We consider the homogenized pore system, represented in Figure 7, saturated with an electrolyte of conductivity σ_f . All the cylindrical channels have a length l and a radius r_c^* determined from the EMA self-consistency condition (5). A potential difference ΔV is applied along the x-axis between the two end surfaces of the network separated by a distance L. The resulting spatial average electric field is $<\mathbf{E}>=\Delta V/L\ \hat{\mathbf{x}}$. The trajectory of a fluid particle of charge q moving in the pore space is determined by the imposed electric field and by the geometry of the pore system. The average drift velocity of the charged particle in a pore channel, $\mathbf{v}$, is proportional to the local electric field $\mathbf{E}$:

$$\mathbf{v} = \frac{\sigma_f}{nq}\mathbf{E} \tag{a-1}$$

where n is the number of ions per unit volume in the electrolyte. As the network is homogeneous and as it has an approximately constant coordination number, the local electric field can be approximated by the component of the spatial average electric field in the direction of the channel axis. Introducing θ the angle between the axis of the cylindrical channel and the direction $\hat{\mathbf{x}}$, we obtain for the drift velocity:

$$v(\theta) = \frac{\sigma_f}{nq}<E>\cos\theta \tag{a-2}$$

In this approximation which becomes exact for a regular network, the drift velocity depends only on the channel orientation relative to $<\mathbf{E}>$. Following the trajectory of the charged fluid particle, the spatial average of the x-component of its velocity is given by:

$$<v_x> = \frac{\sigma_f}{nq}<\cos^2\theta><E> \tag{a-3}$$

where the average is over all channel orientations. The network being isotropic,

the component of the average velocity in the plane perpendicular to the average electric field is identically zero. Next, the average current density, $<J_z>$, across a surface of rock normal to $<\mathbf{E}>$ is obtained by multiplying the average channel current density, $nq <v_z>$, by the porosity ϕ_e^* of the homogenized rock:

$$<J_z> = \sigma_f <\cos^2\theta> \phi_e^* <E> \qquad \text{(a-4)}$$

The constant of proportionality between the bulk current density and the average electric field is by definition the conductivity σ^* of the homogenized rock. So, from (a-4), we have:

$$\sigma^* = \sigma_f <\cos^2\theta> \phi_e^* \qquad \text{(a-5)}$$

which, by construction of the homogenized rock, is also the conductivity of the real rock. It is worth mentioning that Hashin-Shtrikman [1962] upper bound requires that the tortuosity term $<\cos^2\theta>$ be smaller than 2/3.

The derivation of (a-5) is analogous to Scheidegger's analysis [Scheidegger, 1960] of the random walk of a fluid particle moving in the pore space under the effect of a fluid pressure gradient. However, Scheidegger makes the implicit assumption that the pore space of the real rock is homogeneous so that $\phi_e^*=\phi$ in (a-5) and his expression for σ^* reduces to the prediction of Kozeny-Carman model [Walsh et al., 1984; Paterson, 1983].

ϕ_e^* can also be expressed in terms of $g_e^*=\sigma_f \pi r_e^{*2}/l$ which is the electrical conductance of the cylindrical channels forming the homogenized pore space. Defining N_V as the number of branches in the pore space skeleton per unit volume, (a-5) becomes:

$$\sigma^* = <\cos^2\theta> N_V l^2 g_e^* \qquad \text{(a-6)}$$

which shows that the conductivity is expressed as the product of a characteristic local conductance times a length factor which depends on the topology of the pore space skeleton. It is easy to show that (a-6) has exactly the same form as

Batchelor and O'Brien 's formula [1977] giving the electrical conductivity of a disordered isotropic assembly of conducting spheres in good contact. The sphere assembly is electrically equivalent to a disordered resistor network where the nodes are at the particle centers and the branches are associated with the contacts between particles. In Batchelor's work, the length of the branches l corresponds to the diameter of the spheres, 2 N_V corresponds to the number of contacts between particles per unit volume and g_e^* is the conductance at the contact between two particles.

References

Aigeltinger, E.H., and R.T. DeHoff, Quantitative determimation of topological and metric properties during sintering, Met. Trans., 6A, 1853-1862, 1975.

Ambegaokar, V., B.I. Halperin, and J.S. Langer, Hopping conductivity in disordered systems, *Phys. Rev. B, 4,* 2612-2620, 1971.

Barrett, L.K., and C.S. Yust, Some fundamental ideas in topology and their application to problems in metallography, *Metallography, 3,* 1-33, 1970.

Batchelor, G.K., and R.W. O'Brien, Thermal or electrical conduction through a granular material, *Proc. Roy. Soc. Lond., A 355,* 313-333, 1977.

Bernabe, Y., W.F. Brace, and B. Evans, Permeability, porosity and pore geometry of hot pressed calcite, *Mech. of Materials, 1,* 173-183, 1982.

Berryman, J.G., and S.C. Blair, Use of digital image analysis to estimate fluid permeability of porous materials. I. Application of two-point correlation functions, *J. Appl. Phys., 60,* 1930, 1986.

Bourbier, T., and B. Zinszner, Hydraulic and acoustic properties as a function of porosity in Fontainebleau sandstone, *J. Geophys. Res., 90,* 11524-11532, 1985.

Crabtree, S.J., R. Ehrlich, and C. Prince, Evaluation of strategies for segmentation of blue-dyed pores in thin sections of reservoir rocks, *Comput. Graphics Image Process., 28,* 1-18, 1984.

Delfiner, P., A generalization of the concept of size, *J. Microsc., 95,* 203-216, 1972.

DeHoff, R.T., E.H. Aigeltinger, and K.R. Graig, Experimental determination of the topological properties of three-dimensional microstrucures. *J. Microsc., 95,* 69-91, 1972.

Duda, R.O., and P.E. Hart, *Pattern Classification and Scene Analysis,* p. 482. Wiley, New York, 1973.

Dullien, F.A.L., *Porous Media, Fluid Transport and Pore structure,* Academic. New York, 1979.

Ehrlich, R., S. Kennedy, S.J. Crabtree, and R.L. Cannon, Petrographic image analysis, I. Analysis of reservoir pore complexes, *J. Sed. Petrol., 54,* 1365-1378, 1984.

Hashin Z., and S. Shtrikman, A variational approach to the theory of the effective magnetic permeability of multiphase materials, *J. Appl. Phys., 33* 3125-3131, 1962.

Jacquin, C., Corrélations entre la perméabilité et les caractéristiques géométriques du grès de Fontainebleau, *Revue de l'IFP, 19,* 921-937. 1964.

Journel, A.G., and C.J. Huijbregts, *Mining Geostatistics,* p. 600, Academic, London, 1978.

Katz, A.J., and A.H. Thompson, Prediction of rock electrical conductivity from mercury injection measurements, *J. Geophys. Res.,* 92, 599-607, 1987.

Kirkpatrick, S., Percolation and conduction, *Rev. Mod. Phys., 45,* 574-588, 1973.

Koplik, J., Creeping flow in two-dimensional networks, *J. Fluid Mech., 119,*

219-247, 1982.

Koplik, J., C. Lin, and M. Vermette, Conductivity and permeability from microgeometry, *J. Appl. Phys., 56,* 3127-3131, 1984.

Lin, C., and M.H. Cohen, Quantitative methods for microgeometric modeling, *J. Appl. Phys., 53,* 4152-4165, 1982.

Matheron, G., *Eléments Pour Une Théorie Des Milieux Poreux,* p. 166, Masson, Paris, 1967.

Paterson, M.S., The equivalent channel model for permeability and resistivity in fluid-saturated rock - a re-appraisal, *Mech. of Materials, 2,* 345-352, 1983.

Pittman, E.D., The pore geometries of reservoir rocks, in *Physics and Chemistry of Porous media,* AIP Conf. Proc., 107, p. 1-19, edited by D.L. Johnson and P.N. Sen, American Institute of Physics, New York, 1984.

Rink, M., and J.R. Schopper, On the application of image analysis to formation evaluation, *The Log Analyst,* 12-22, 1978.

Ripley, B.D., *Spatial Statistics,* p. 252, Wiley, New York, 1981.

Scheidegger, A.E, *The Physics of Flow Through Porous Media,* p. 353, University of Toronto, 1960.

Serra, J., *Image Analysis and Mathematical Morphology,* p. 610, Academic, London, 1982.

Underwood, E.E., *Quantitative Stereology,* Addison-Wesley, Reading, Massachusetts, 1970.

Walsh, J.B., and W.F. Brace, The effect of pressure on porosity and the

transport properties of rock, *J. Geophys. Res., 89,* 9425-9431, 1984.

Wong, P.Z., J. Koplik, and J.P. Tomanic, Conductivity and permeability of rocks, *Phys. Rev. B, 30,* 6606-6614, 1984.

Table 1

Porosity, coordination number, throat sizes and pore size
used in predicting
the permeability and conductivity of Fontainebleau sandstone

ϕ (%)	$\overline{z}$ (#)	r_e^* (μm)	r_h^* (μm)	$<r^2>^{1/2}$ (μm)
5.2	2.3	5.8	4.8	16.1
7.5	3.0	5.8	5.2	13.2
9.7	4.4	10.4	10.6	18.9
15.2	5.6	13.7	14.6	27.3
18.0	5.9	11.7	12.7	21.8
19.5	5.7	16.0	17.3	20.0
22.1	6.0	18.7	20.3	30.2

Figure 1:

Binary images of 7 microsections of Fontainebleau sandstone with different porosity ϕ. The black areas are the porous zones and the white areas are the quartz grains. Each scene is about 2.7 x 2.0 mm^2.

Figure 2:

Erosion of one pore element with a circle C whose radius r increases.

Figure 3:

Progressive erosion of the digitized pore structure of Fontainebleau sandstone with a digital structuring element whose shape approximates that of an expanding circle.

Figure 4:

Experimental throat size frequency distribution measured from thin sections of Fontainebleau sandstone (a) with $\phi = 22.1\%$ and (b) with $\phi = 7.5\%$.

Figure 5:

Experimental pore size frequency distribution measured from thin sections of Fontainebleau sandstone (a) with $\phi = 22.1\%$ and (b) with $\phi = 7.5\%$.

Figure 6:

Microscopically heterogeneous pore system and its

skeleton.

Figure 7:

The homogenized pore system is obtained by dilating uniformely the skeleton (figure 6) into a network of cylindrical flow channels with radius r^*. Also represented is the trajectory of a charged fluid particle moving in the uniform pore space in response to the applied external field $<\mathbf{E}>$.

Figure 8:

Log-log plot of the permeability of Fontainebleau sandstone as a function of porosity. The *'s represent the experimental measurements. The o's represent the predicted values based on the effective medium approximation. The slope of the dashed line fitting the measurements is 3.8.

Figure 9:

Log-log plot of the formation factor σ_f / σ^* of Fontainebleau sandstone as a function of porosity. The *'s represent the experimental measurements. The o's represent the predicted values based on the effective medium approximation. The slopes of the two dashed lines fitting the measurements are -1.9 and -3.7.

Figure 1

$\phi = 5.2\%$

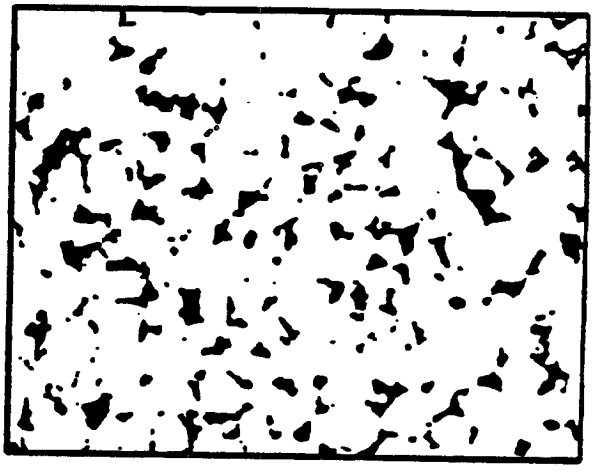

$\phi = 7.5\%$

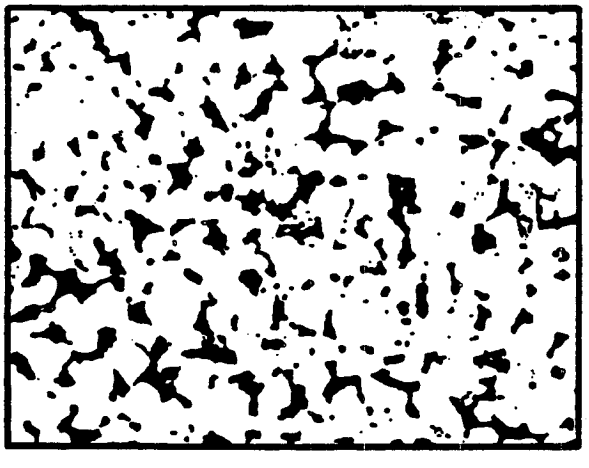

$\phi = 9.7\%$

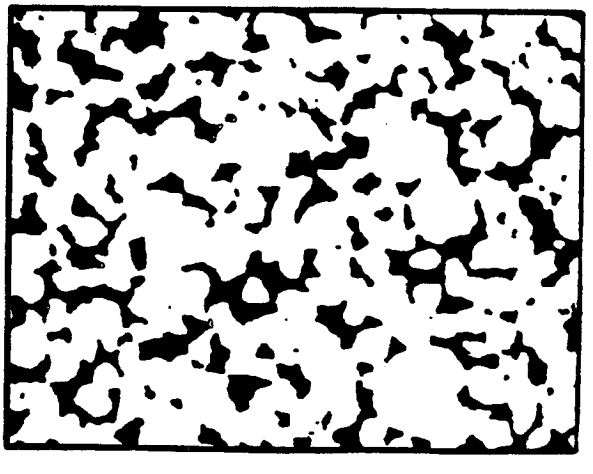

$\phi = 15.2\%$

Figure 1 (cont.)

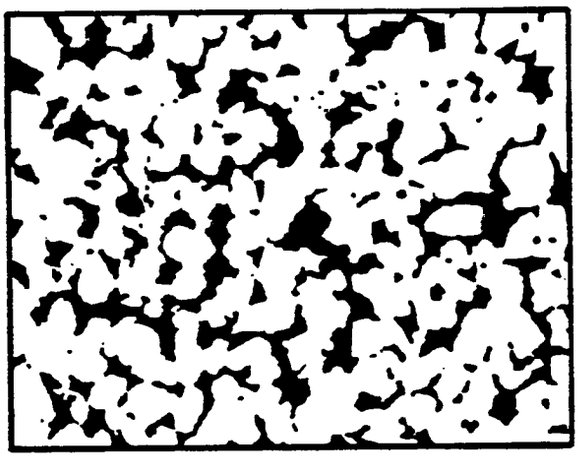

$\phi = 18.0\%$

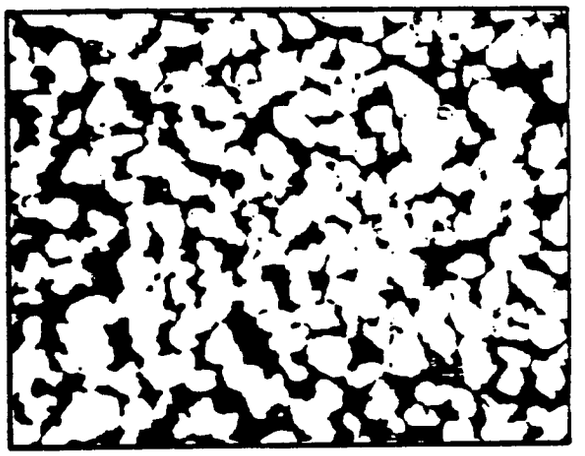

$\phi = 19.5\%$

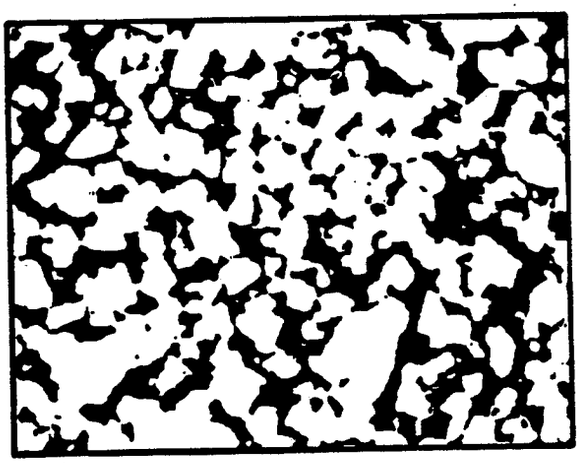

$\phi = 22.1\%$

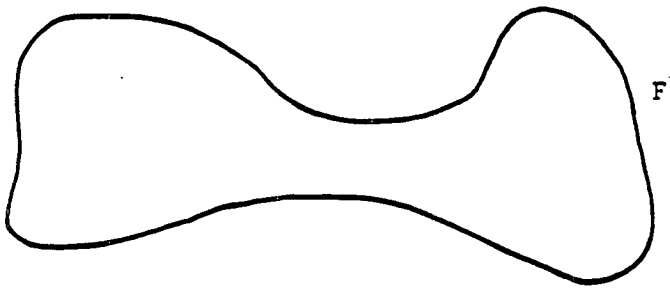

Figure 2

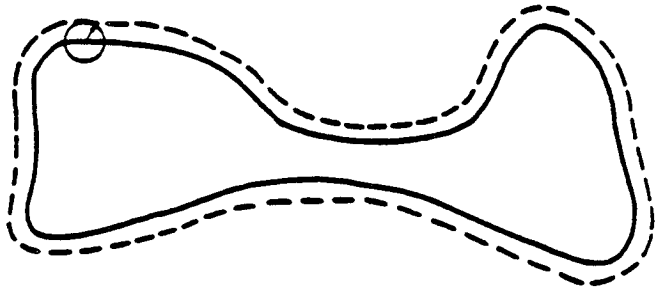

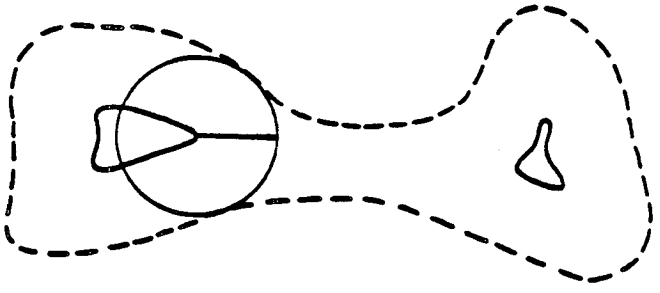

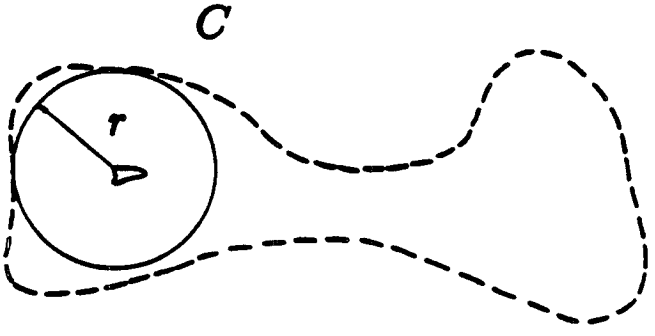

Figure 3

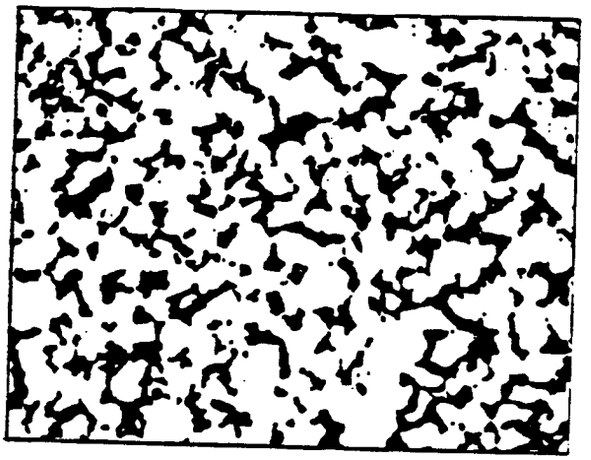

(a)

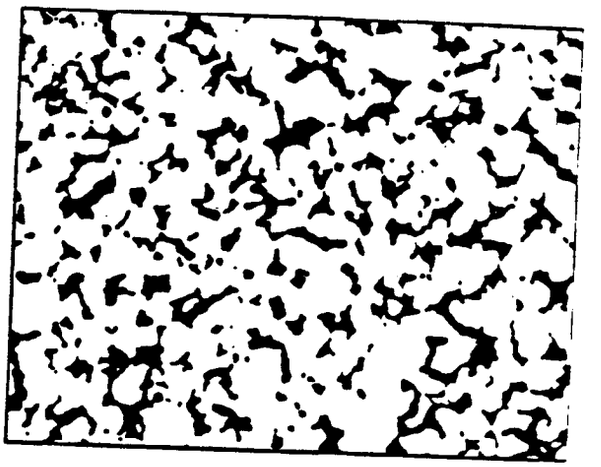

(b)

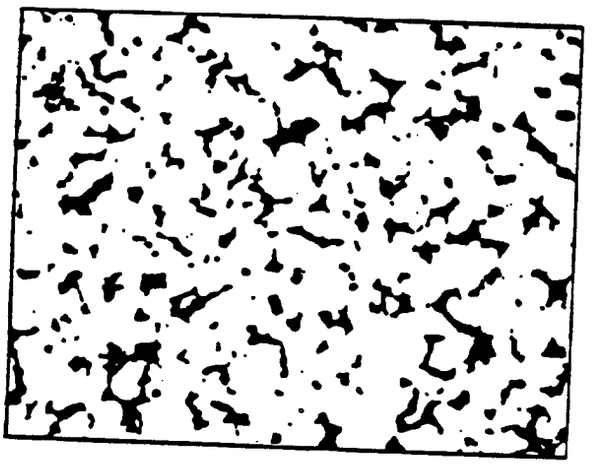

(c)

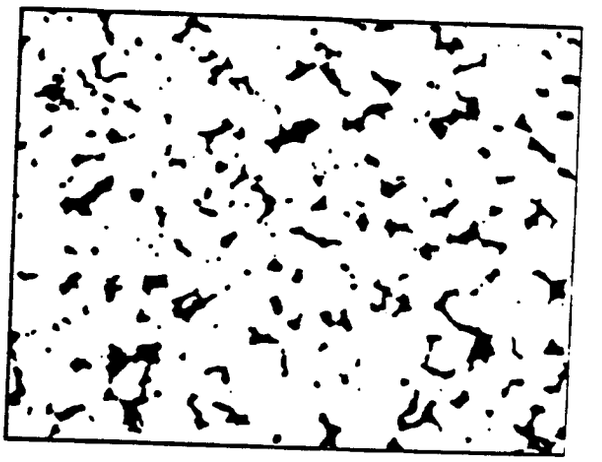

(d)

Figure 4

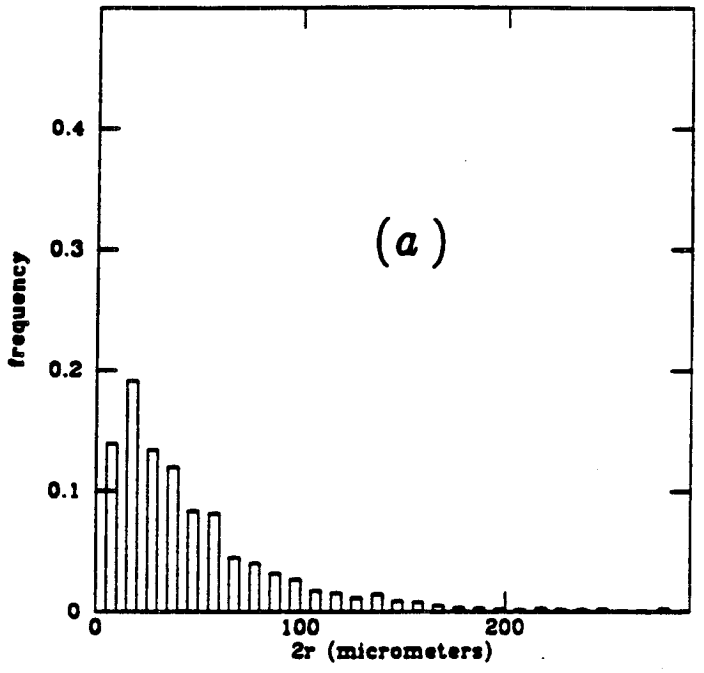
(a)
frequency
0.4
0.3
0.2
0.1
0
0
100
200
2r (micrometers)

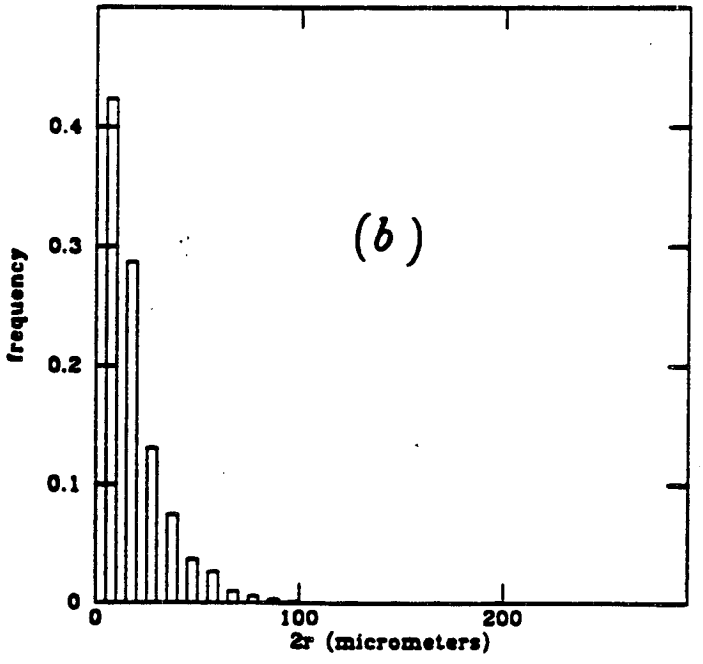
(b)
frequency
0.4
0.3
0.2
0.1
0
0
100
200
2r (micrometers)

Figure 5

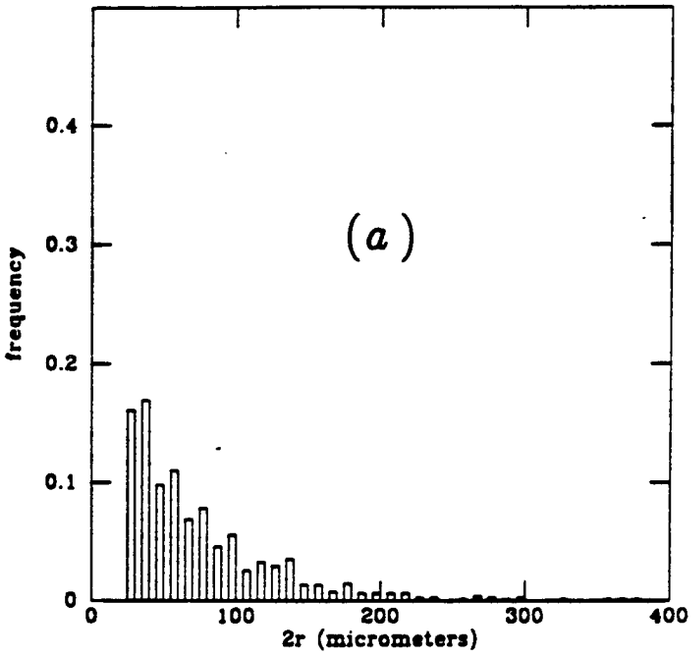
(a)
frequency
0.4
0.3
0.2
0.1
0
0
100
200
300
400
2r (micrometers)

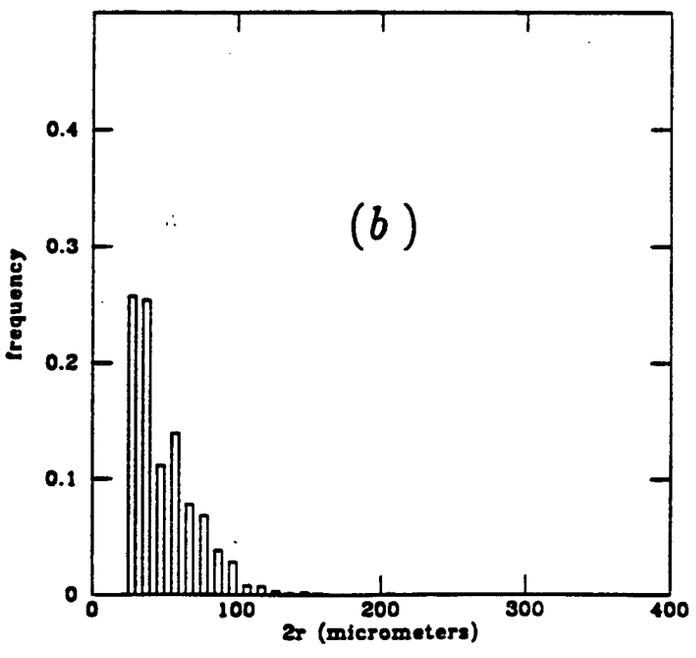
(b)
frequency
0.4
0.3
0.2
0.1
0
0
100
200
300
400
2r (micrometers)

Figure 6

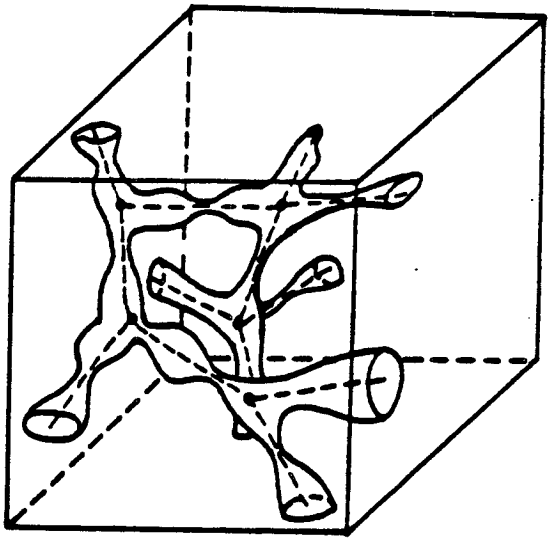

Figure 7

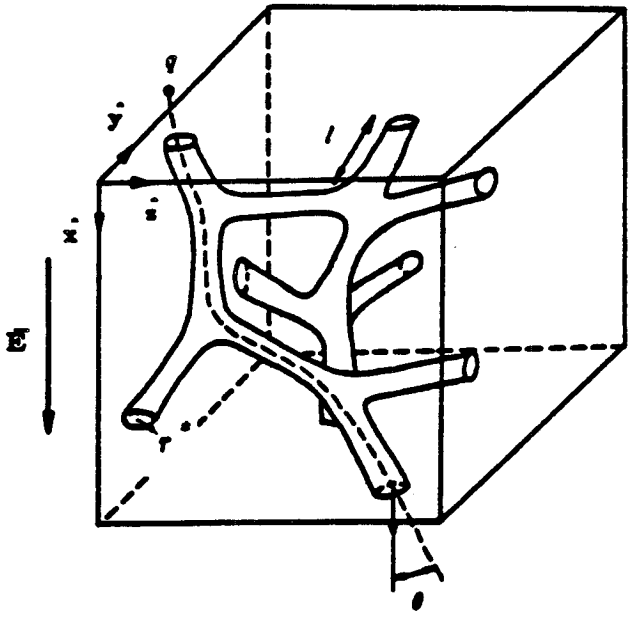

Figure 8

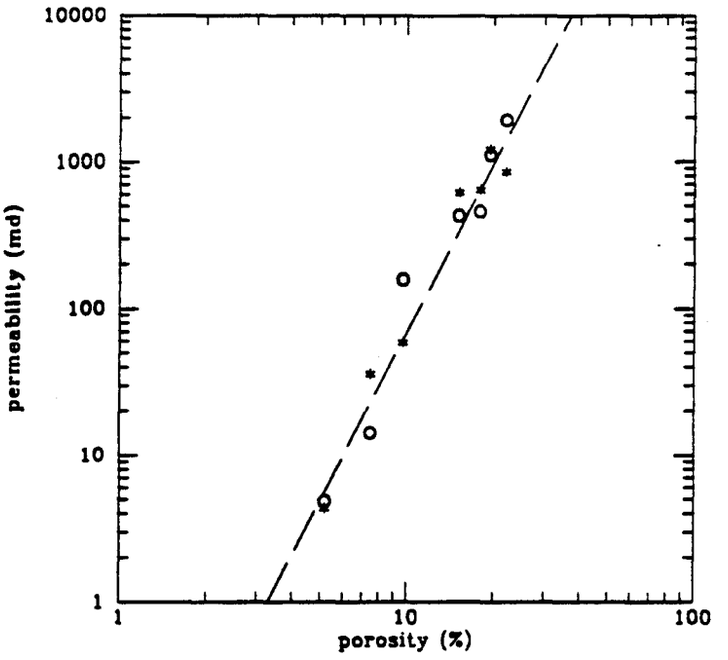

Figure 9

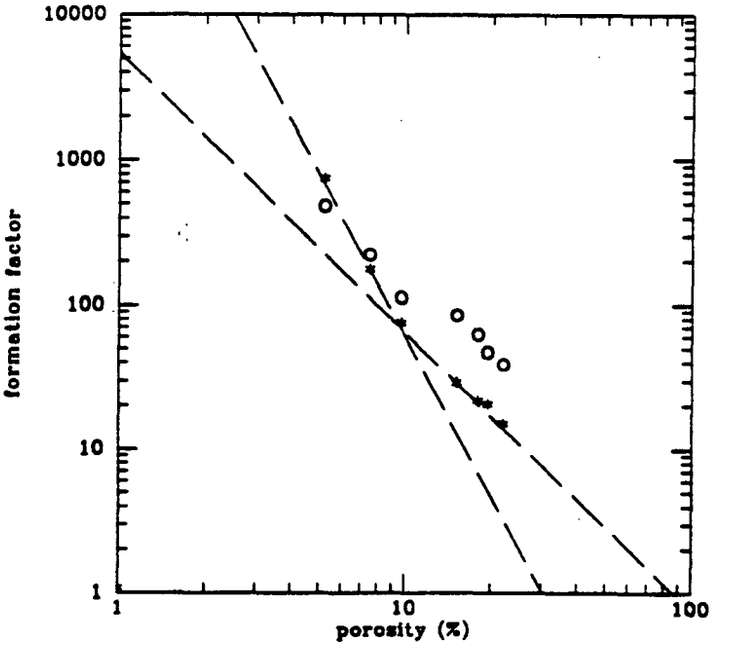

CHAPTER 3:

CRACK GEOMETRY IN IGNEOUS ROCKS, A MAXIMUM ENTROPY INVERSION OF ELASTIC AND TRANSPORT PROPERTIES

Abstract.

The maximum entropy method is used to infer the dimensions of cracks in igneous rocks from measurements made under confining pressure of their compressibility, d.c. electrical conductivity, and hydraulic permeability. The fluctuations of crack dimensions are characterized by a crack spectrum which gives the frequency of occurrence of cracks as a function of their cross-sectional length and aspect ratio in the absence of stress. The cracks deform elastically and close under pressure. The resulting variations of the bulk properties are obtained by averaging the pressure-dependent crack contributions over the unknown crack spectrum. The compressibility depends on the average of the square of the crack cross-sectional length. The transport coefficients are proportional to some characteristic crack conductances which are expressed self-consistently at each pressure in terms the spectrum. The maximum entropy crack spectrum in Westerly granite is determined from laboratory measurements of the elastic and of the transport coefficients as a function of pressure. The predicted spectrum is comparable with the distribution of dimensions estimated from direct observations of cracks with a scanning electron microscope. The wide range of crack length contrasts with the existence of a constant crack width. The main features of the calculated spectrum are interpreted from a model of growth of the microfissures during cooling of the granite.

1. Introduction

In a series of laboratory experiments in the 1960s, W.F. Brace and his coworkers studied the behavior of igneous rocks under external confining pressure. In particular, they measured the compressibility of dry rocks [Brace, 1965] the hydraulic permeability [Brace et al., 1968] and the d.c. electrical conductivity [Brace et al., 1965] of rock samples saturated with a conducting electrolyte. For

pressure increasing from 0 to 10^3 MPa, very pronounced correlated variations were observed: the compressibility dropping typically by almost 1 order of magnitude and the transport coefficients decreasing by factors of 10^2 to 10^3. The effect of confining pressure on igneous rocks is surprisingly large considering their small porosity, usually less than 1%. This large effect reflects the presence of microcracks. Crack closure under pressure stiffens the rocks considerably. The cracks also serve as conduction paths for the flow of fluid and the flow of electrical current. When a rock sample saturated with a conducting electrolyte is compressed, the closure of cracks eliminates conducting paths in the pore space. A decrease of transport coefficients results, which parallels the reduction of compressibility. However, at pressure as high as 10^3 MPa the conductivity of electrolyte-saturated rocks remains several orders of magnitude greater than the conductivity of dry rocks. At high pressure the fluid still percolates and a small residual porosity still exists, forming an interconnected network of stiff microscopic flow channels.

In this study we first explore theoretically the relationship between the pressure-dependent transport and elastic properties of igneous rocks and the crack population. Then, using the maximum entropy method [Jaynes, 1957], the spectrum of crack dimensions is inferred from measurements made under confining stresses of compressibility, conductivity, and permeability.

The pore space is portrayed by a topologically disordered network of interconnected tubular cracks of approximately constant length l but variable cross-sectional dimensions (Figure 1). In the absence of stress the crack cross-sectional dimensions are described by two parameters: the half length and the half width, c and b, respectively. The aspect ratio defined as the ratio $\alpha = b/c$ measures the ellipticity of the crack cross section. The fluctuations of

crack dimensions are characterized by a crack spectrum or size distribution $n(\alpha,c)$ which gives the frequency of occurrence of cracks as a function of α and c. The cracks are assumed randomly oriented and positioned so that the crack assembly is homogeneous and isotropic at a macroscopic scale. For cracks occurring at grain boundaries as in Westerly granite, this condition is met if the minerals are uniformly mixed. In the absence of confining pressure the crack network is supposed fully interconnected with a spatial average coordination number $\overline{z} \approx 4$ to 6. The great density of cracks and their sheetlike geometry justifies the hypothesis of continuity of the crack assembly.

The rock matrix is assumed homogeneous and isotropic at a macroscopic scale. At the grain size scale the crystalline framework is formed of anisotropic minerals with different elastic properties. But when averaged over a large number of randomly mixed crystals, the matrix properties are expected to be independent of orientation and position. It is further assumed that the rock matrix obeys linear elasticity with elastic constants being simple averages of the elastic constants of the minerals forming the aggregate. At room temperature and for laboratory pressures less than 10^3 MPa this hypothesis is justified by the smallness of the change (typically a few percent) of elastic moduli of the minerals compared with the variation of rock compressibility by more than 100% [Walsh, 1980]. In fact, small deviations from the assumptions about the rock matrix are unimportant as the low-pressure dependence of the bulk properties of igneous rocks is thought to be controlled by the pore space geometry rather than by the mineralogical composition.

The last but important assumption is that at room temperature, the rock as a whole deforms elastically in the pressure range (0 to 10^3 MPa) considered. The relatively small hysteresis observed in the macroscopic response of igneous rocks

under hydrostatic loading suggests that this last hypothesis is reasonable [Walsh, 1980]. On a microscopic scale, reversibility entails that the dimensions of a crack at a given pressure level are uniquely related to the dimensions in the unstressed state. This in turn implies that the macroscopic behavior of rock under pressure can in principle be determined from the original crack size distribution $n(\alpha,c)$ at zero pressure.

In the first part of this study the macroscopic rock properties are obtained by averaging the crack contributions over the distribution $n(\alpha,c)$, and their variations with confining pressure are interpreted in terms of the deformation and closure of the cracks. In section 2, the model of elastic deformation is presented. Under the assumption of elastically noninteracting cracks the compressibility at a given pressure depends on the average of the square of the crack cross-sectional length. In section 3, using the effective medium theory discussed in chapter 2, the transport coefficients are expressed at each pressure in terms of $n(\alpha,c)$ and in terms of the pressure-dependent crack electrical and hydraulic conductances. The change of the network connectivity with pressure is also analyzed.

In the second part of this chapter the inverse problem is addressed. Section 4 deals with the formalism of the maximum entropy inversion method. The crack spectrum $n^*(\alpha,c)$ representing a condition of maximum entropy is inferred from pressure-dependent macroscopic averages. In section 5, the maximum entropy method is used to estimate the spectrum of cracks in Westerly granite from measurements of the transport and elastic coefficients under pressure. The calculated spectrum is then compared with the distribution of crack dimensions estimated from micrographs of Westerly granite.

2. Elastic Volumetric Deformation of Igneous Rocks Under Pressure

At room temperature, when a confining pressure p_c is applied uniformly over the external boundary of dry igneous rocks, the resulting volumetric strain is essentially reversible but not linear. It follows that the effective compressibility β^*, which is proportional to the local derivative to the strain curve, varies with confining pressure. The $\beta^*(p_c)$ is defined as

$$\beta^*(p_c) = -\frac{1}{V_0}\frac{dV}{dp_c} \tag{1}$$

which is the rate of change with p_c of the rock volume V normalized to the volume at zero pressure V_0. Typically, a two-stage response to the application of pressure is observed for igneous rocks [Brace, 1965]. The effective compressibility decreases first very rapidly. Then, at pressures of the order of a few hundred megapascals, β^* reaches a constant value, the rock behaving essentially like a linear elastic solid. The nonlinear character of elastic deformation and the high compressibility at low confining stresses indicate the presence of microcracks in igneous rocks. The effect of cracks can be explained from the relation existing between the rock compressibility β^*, the compressibility of the solid phase β_s, and the rate of change of the void volume V_p with p_c [Walsh, 1965; Zimmerman, 1984]:

$$\beta^*(p_c) = \beta_s - \frac{1}{V_0}\frac{dV_p}{dp_c} \tag{2}$$

The derivation of (2) requires only that the solid framework be homogeneous, isotropic, and linearly elastic. At room temperature and for $p_c \leq 10^3$ MPa, β_s is approximately constant. The large variation of β^* must then be explained by the rate of decrease dV_p/dp_c of the pore space volume with pressure. At low p_c, the large value of β^* reflects the large closing rate of thin elongated cracks. At high confining stresses the residual porosity corresponds to small round openings deforming at very small rate; β^* then approaches β_s, the

compressibility of the crack-free solid.

To model the change of the void volume with pressure, the deformation of the system of tubular cracks (Figure 1) must be calculated. Following Seeburger and Nur [1984], cylindrical cracks with either tapered or elliptical cross sections are considered (Figures 2 and 3). They are treated classically as two-dimensional void inclusions in plane strain imbedded in a solid, homogeneous, and isotropic elastic matrix. Furthermore, the stress fields around the cavities are assumed not to interact. Each opening deforms then independently under pressure at a rate determined only by the elastic moduli of the matrix and by the aspect ratio α in the unstressed configuration. In particular, for a thin ($\alpha \leq 0.1$) tapered crack, the half length C and the half width B of the cross section decrease according to the following expressions [Mavko and Nur, 1978]:

$$C(p;\alpha,c) = c\left(1 - \frac{4(1-\nu^2)}{3E\alpha}\, p\right)^{1/2} \tag{3}$$

$$B(p;\alpha,c) = \alpha c \left(1 - \frac{4(1-\nu^2)}{3E\alpha}\, p\right)^{3/2}$$

where E and ν are the Young's modulus and the Poisson's ratio, respectively, of the solid elastic matrix. We use the C and B to denote the crack dimensions at $p > 0$. In (3), $p = p_c - p_f$ is the effective confining pressure defined as the difference between the hydrostatic confining pressure applied uniformly over the outer surface of the rock, p_c, and the hydrostatic pressure in the fluid filling the crack p_f. This definition of the effective pressure is valid only under the three following assumptions [Nur and Byerlee, 1971; Zimmerman, 1984]. The rock matrix must be elastic, homogeneous, and isotropic. The number of cracks per unit volume must be large. The volumetric strain must depend only on the final values of p_c and p_f and not on the path followed in the (p_c, p_f) plane. The fluid pressure will play a role in section 3, where the transport coefficients of rock saturated with a conducting electrolyte are studied. Under the plane strain

assumption a crack closes uniformly over its entire length, and the change of l with pressure is neglected.

For cavities with an elliptical cross section of any aspect ratio, the half length and half width, C and B, vary exponentially with p [Bernabe et al., 1982]. But for $p \leq 10^3$ MPa and for typical values of matrix moduli ($E \approx 8.13\ 10^4$ MPa and $\nu \approx 0.27$ for Westerly granite) the exponentials can be approximated by terms linear in the effective pressure. $C(p)$ and $B(p)$ are then given respectively by

$$C(p;\alpha,c) \approx c \left(1 - \alpha \frac{2(1-\nu^2)}{E} p\right) \tag{4}$$

$$B(p;\alpha,c) \approx \alpha c \left(1 - \frac{2(1-\nu^2)}{\alpha E} p\right)$$

for $p/E << 1$. In the calculations, however, we will use the exact exponential formulas.

The pressure-dependent crack volume can now be expressed in terms of B and C as

$$v(p;\alpha,c) = \frac{3}{4}\pi l\ B(p;\alpha,c)\ C(p;\alpha,c) \tag{5}$$

for a crack with tapered cross section and as

$$v(p;\alpha,c) = \pi l\ B(p;\alpha,c)\ c(p;\alpha,c) \tag{6}$$

for a crack with elliptical cross section. In both cases the rate of decrease of the crack volume is controlled by the aspect ratio in the unstressed configuration α. The pressure at which a thin tubular crack completely closes, p_{clo}, is given by

$$p_{clo}(\alpha) = \frac{3}{4} \frac{\alpha E}{(1-\nu^2)} \tag{7}$$

for a tapered crack (equation (3)) and by

$$p_{clo}(\alpha) = \frac{1}{2} \frac{\alpha E}{(1-\nu^2)} \tag{8}$$

for an elliptical crack (equation (4)). So, independently of the exact shape, a flat

convex cavity closes rapidly at low confining stresses of the order of αE, while a more equidimensional opening ($\alpha > 0.1$) requires pressures of the order of Young's modulus of the solid matrix to deform substantially.

In section 1 the crack size frequency distribution $n(\alpha,c)$ was defined by

$$n(\alpha,c) = \frac{N(\alpha,c)}{N} \tag{9}$$

where $N(\alpha,c)$ is the number of cracks with aspect ratio α and half length c in a rock volume V_0 containing a total number N of cracks. Neglecting the change of rock volume with p_c ($V(p_c)=V_0$), we obtain the pressure-dependent porosity of dry rock, $\phi(p_c) = V_p(p_c) / V_0$, by summing the volume of each type of crack weighted by its frequency of occurrence $n(\alpha,c)$. From (5) or (6), we have

$$\phi(p_c) = a\ N_V l \sum_{\alpha,c} n(\alpha,c) B(p_c;\alpha,c)\ C(p_c;\alpha,c) \tag{10}$$

where the pressure-dependent crack dimensions B and C are given in (3) or (4) in terms of α and c, the crack parameters in the absence of stress. In (10), $N_V = N/V_0$, is the number of cracks per unit volume and a is a constant depending on the crack cross-sectional shape ($a = 3\pi/4$ for tapered cracks and $a = \pi$ for elliptical cracks). Finally, following Walsh [1965], we combine (2) and the derivative of (10) with respect to p_c, and we obtain the compressibility of the solid perforated by a family of elastically noninteracting dry cracks with size distribution $n(\alpha,c)$ as

$$\beta^*(p_c) = \beta_s + \frac{2\pi(1-\nu^2)}{E} N_V\ l \sum_{\alpha,c} n(\alpha,c)\ C^2(p_c;\alpha,c) \tag{11}$$

for thin tapered cracks [Mavko and Nur, 1978]. For elliptical cracks, the result is [Bernabe et al., 1982]

$$\beta^*(p_c) = \beta_s + \frac{2\pi(1-\nu^2)}{E} N_V\ l \sum_{\alpha,c} n(\alpha,c) \left[C^2(p_c;\alpha,c) + B^2(p_c;\alpha,c) \right] \tag{12}$$

In particular, for thin ellipses ($b < 0.1\ c$), the term B^2 in (12) is negligible. Equations (11) and (12) then both show that the introduction of a thin crack in a

solid of compressibility β_s increases the compressibility by an amount proportional to lC^2 and not to the crack volume (lBC). So, a very small amount of porosity in the form of long flat cracks can drastically enhance the compressibility of rock at low pressures. The dependence of β^* on the square of the crack major cross-sectional axis is in fact a general result independent of crack shape [Mavko and Nur, 1978].

To conclude this section, we underline the differences between the model elliptical or tapered cracks and real cracks in rock. The theory reviewed here is based on the elastic deformation and closure of the model cracks under pressure. In reality, the roughness of the crack walls prevents a complete closure of the microfissures [Batzle et al., 1980]. Walsh and Grosenbaugh [1979] proposed a model of crack deformation based on the theory of rough surfaces in contact. We do not think that this theory is appropriate at low confining stresses where the heights of the asperities are typically much smaller than the crack apertures. The effectiveness of crack closure under pressure in Westerly granite is supported by the large observed decrease of the transport coefficients [Brace et al., 1965, 1968]. However, at high pressure, our assumption of perfect crack closure may lead to an exaggeration of the population of round cavities.

In this section we have also considered regularly shaped model cracks. Real cracks are never elliptical or tapered. As the rate of deformation of a crack depends on its exact shape, the interpretation of the rock elastic response in terms of a crack spectrum $n(\alpha,c)$ may appear too much dependent on the selected model shape [Mavko and Nur, 1978]. For cracked rocks with a wide range of aspect ratio, we will see that the estimated crack spectrum is relatively insensitive to the exact model shape.

Finally, the deformation of the pore space was calculated by summing the

contributions of cracks deforming independently under pressure. In reality, the cracks are intersecting and their deformation cannot be completely independent [Batzle et al., 1980]. Self-consistent methods (see, for example, O'Connell and Budiansky [1974]) exist to account approximately for interactions between the stress fields of neighboring cavities. Application of a self-consistent scheme requires the knowledge of two effective static moduli. In the absence of such data for Westerly granite, this method was not considered. The consequence of neglecting crack interactions will be assessed in section 5.

3. Transport Properties of Igneous Rocks Under Pressure

In this section, using the effective medium approximation (EMA) discussed in chapter 2, the transport coefficients are expressed implicitly in terms of the crack size distribution $n(\alpha,c)$. The permeability κ^* and the conductivity σ^* are now functions of the effective confining pressure, $p = p_c - \bar{p}_f$, where $\bar{p}_f$ ($<< p_c$) is the average fluid pressure in the pore space.

Locally in the crack system, the flow is controlled by the value of the crack conductances. These local hydraulic and electrical conductances decrease when the effective pressure p is raised. This variation reflects the shortening of the crack cross-sectional dimensions C and B under pressure. In particular, the pressure-dependent electrical and hydraulic conductances of a tubular tapered crack of length l, saturated with a fluid of conductivity σ_f, are given respectively by [Seeburger and Nur, 1984]

$$g_e(p;\alpha,c) = \sigma_f \frac{3}{4}\frac{\pi BC}{l} \quad (\Omega^{-1}) \tag{13a}$$

and

$$g_h(p;\alpha,c) \approx \frac{\pi}{4l}\frac{B^3(\frac{3}{4}C)^3}{B^2+(\frac{3}{4}C)^2} \quad (m^3) \tag{13b}$$

where the pressure-dependent cross-sectional half length $C(p;\alpha,c)$ and half width $B(p;\alpha,c)$ are expressed in (3) in terms of α and c. For a tube with elliptical cross section the conductances are

$$g_e(p;\alpha,c) = \sigma_f \frac{\pi BC}{l} \tag{14a}$$

and

$$g_h(p;\alpha,c) = \frac{\pi}{4l} \frac{B^3C^3}{B^2 + C^2} \tag{14b}$$

where $C(p;\alpha,c)$ and $B(p;\alpha,c)$ are given in (4).

From the definitions (13) or (14) the crack size distribution $n(\alpha,c)$ can be converted at each pressure p to two frequency distributions $n(g_e;p)$ and $n(g_h;p)$, which characterize respectively the fluctuations of local electrical and hydraulic conductances on the network supporting the flow process. With g standing for g_e *or* g_h, we have

$$n(g;p) = \sum_{(\alpha,c) \mid g(p;\alpha,c) = g} n(\alpha,c) \tag{15}$$

where the summation is over all crack types (α,c) such that the equality $g = g(p;\alpha,c)$ holds. The conductances, g_e and g_h determine the flow at the scale of a microscopic channel in the rock. At the scale of a laboratory sample containing many cracks, the transport properties are controlled by the pressure dependent distributions of the crack conductances $n(g_e;p)$ and $n(g_h;p)$.

If the electrical conductance distribution is known at each pressure p, the conductivity σ^* can be calculated from the EMA self-consistency condition

$$\sum_{g_e} n(g_e;p) \frac{l^*\sigma^*(p) - g_e}{g_e + (\frac{z}{2} - 1)\, l^*\sigma^*(p)} = 0 \tag{16}$$

where the characteristic length of the crack network $l^* = (1/3\, N_V\, l^2)^{-1}$ was calculated in the appendix of chapter 2 (eq. (a-6)). Using (15), the self-consistency condition (16) expressed in terms of the distribution $n(g_e;p)$ can be

replaced by the following equivalent average over the crack size distribution $n(\alpha,c)$

$$\sum_{\alpha,c} n(\alpha,c)\,\frac{l^*\sigma^*(p)-g_e(p;\alpha,c)}{g_e(p;\alpha,c)+(\frac{z}{2}-1)\,l^*\sigma^*(p)}=0 \qquad (17)$$

where $g_e(p;\alpha,c)$ is the pressure-dependent conductance of a crack with cross-sectional aspect ratio α and half length c in the unstressed state. (See equation (13a) or (14a).) A condition similar to (17) is obtained for the pressure dependent permeability by replacing g_e by g_h and σ^* by κ^*.

It is important to mention that the EMA can only be applied at relatively low pressures where the fraction of conducting cracks is well above the critical concentration corresponding to the percolation thershold. In the absence of stress, all the cracks are open, and the crack system is fully interconnected. When the pressure is raised to a value p, all cracks with initial aspect ratio α less than approximately p/E (equation (7) or (8)) are closed and nonconducting. It follows that, with increasing p, the conductance distributions $n(g_e;p)$ and $n(g_h;p)$ become more weighted near zero. Letting $g=g_e$ or g_h, this can be expressed by

$$n(g;p)=f(p)\cdot h(g;p)+(1-f(p))\,\delta(g) \qquad (18)$$

where $f(p)$, the fraction of open cracks at pressure p, decreases monotonically with increasing pressure. This fraction can be expressed in terms of the aspect ratio distribution $n(\alpha)$ as the relative number of cavities with an initial aspect ratio larger than approximately p/E:

$$f(p)=\sum_{c,\alpha>p/E} n(\alpha,c)=\sum_{\alpha>p/E} n(\alpha) \qquad (19)$$

The fraction of open cracks $f(p)$ is an indicator of the connectivity of the crack network. When p is raised to some critical value, the fraction of conducting cracks reaches the critical concentration $f_c=f(p_{critical})$ at which the crack

network becomes disconnected. At the thershold, the average number of open intersecting cracks, zf_c, is known to be approximately invariant for all regular crack lattices. It is given by [Kirkpatrick, 1973]

$$z\ f_c \approx \frac{d}{d-1} \tag{20}$$

where d is the dimensionality of the lattice. This result is expected to hold for our topologically disordered crack network with the coordination number z replaced by the spatial average $\bar{z}$. Now, the EMA is known to fail in the direct vicinity of the percolation threshold. In particular, it predicts a zero conductivity or permeability ($g^*=0$ in equation (16)) at a concentration of conducting elements $f_c = 2/z$ independently of d. This prediction is clearly wrong for the three-dimensional crack network where, based on (20), the threshold is expected to occur at lower concentration of conducting cracks. In summary, as the pressure is raised, the conductance distributions become more strongly weighted near zero, $f\ (p)$ decreases and the accuracy of the EMA deteriorates. Using this approximation requires that a large fraction of openings still exists in the rock up to 10^3 MPa ($f\ (p=10^3 MPa) > 2/\bar{z}$) so that the critical region is not reached. Scanning electron microscopy (SEM) suggests that igneous rocks may indeed contain a large number of small stiff cavities which require pressures much larger than 10^3 MPa to close [Hadley, 1976; Batzle et al., 1980].

4. The Maximum Entropy Method

In this section the maximum entropy method (MEM) is introduced. This inversion method is used to infer the unique crack spectrum consistent with the experimental data which satisfies a condition of maximum entropy.

In the previous sections the pressure-dependent porosity, compressibility, and transport coefficients were calculated by averaging the crack contributions over the unknown crack spectrum $n\ (\alpha,c)$. Equations (10), (11), (12), and (17) can be

rewritten in a more compact generic form as follows:

$$<A_p> = \sum_{\alpha}^{N_\alpha} \sum_{c}^{N_c} n(\alpha,c)\, A(\alpha,c,p) = 0 \qquad (21)$$

$$\text{for } p = p_1, p_2, \ldots, p_m$$

where the normalization condition

$$\sum_{\alpha,c} n(\alpha,c) = 1 \qquad (22)$$

was used in (10), (11), and (12) to express all terms under the summation signs. To each rock property A (ϕ, β^*, κ^*, *or* σ^*) measured at pressure p corresponds a linear average $<A_p>$ over the unknown crack spectrum. $A(\alpha,c,p)$ refers to the contribution of a crack with dimensions (α,c) on the property A measured at p. In (21), m is the number of pressures at which an experimental measurement is available and $N_\alpha N_c$ represents the total number of crack types, each type being specified by a pair of crack parameters (α,c).

Considering the wide range of crack dimensions in igneous rocks [Sprunt and Brace, 1974; Hadley, 1976], there are many continuous crack spectra that could give rise to the same macroscopic response of the rock under pressure. In our discrete parameter space we choose $N_\alpha N_c$ to be much larger than the number m of linear constraints (equations (21) and (22)), and there exists an infinite number of $n(\alpha,c)$ compatible with the experimental averages $<A_p>$. To remove the undeterminacy, we must introduce a criterion by which a particular crack size frequency distribution is selected.

In the context of information theory, Shannon and Weaver [1949] introduced the entropy as a measure of the amount of uncertainty associated with a discrete frequency distribution. For the crack spectrum the entropy is defined by

$$S(n(\alpha,c)) = -\sum_{\alpha,c} n(\alpha,c) \ln n(\alpha,c) \geq 0 \qquad (23)$$

Shannon proved that S is the unique functional satisfying certain consistency

rules chosen as requirements in defining an information measure. The entropy has some simple and useful properies. In particular, S may be seen as a measure of the uniformity of the crack spectrum. S is maximum and equal to $\ln N_\alpha N_c$ when the spectrum is uniform, i.e., $n(\alpha,c)=1/N_\alpha N_c$. S is equal to zero when the spectrum is a delta function. Guided by the concept of entropy, we seek, among the infinite number of crack spectra consistent with the data, the one which maximizes S. The solution of this constrained maximization gives the spectrum that agrees with the measured $<A_p>$ but that is otherwise distributed as uniformly as possible. Under a postulate of equal a priori probability for all the configurations $(\alpha,c)_1, \cdots, (\alpha,c)_N$ of the N cracks reproducing the macroscopic data, it can also be shown [Tolman, 1938; Jaynes, 1968], based on a simple combinatorial argument, that the maximum entropy spectrum is the most likely and that its likelihood grows exponentially with the number of cracks. SEM studies [Hadley,1976] of igneous rocks show that the number N of microcracks may be at least on the order of 10^8 in a $10cm^3$ laboratory sample.

Introducing Lagrange's multipliers for the linear constraints (21) and (22), the maximum entropy crack spectrum is obtained by setting to zero the partial derivatives with respect to the $n(\alpha,c)$ of the following expression:

$$-\sum_{\alpha,c} n(\alpha,c)\ln n(\alpha,c) - \sum_{p}^{p_m} \lambda_p <A_p> - \mu \sum_{\alpha,c} n(\alpha,c) \tag{24}$$

The resulting well known formal solution is [Jaynes, 1957; Tribus, 1961]

$$n^*(\alpha,c) = \frac{1}{Z} \exp\left\{-\sum_p \lambda_p A(\alpha,c,p)\right\} \tag{25}$$

with

$$Z(\lambda_{p_1}, \ldots, \lambda_{p_m}) = \sum_{\alpha,c} \exp\left\{-\sum_p \lambda_p A(\alpha,c,p)\right\} \tag{26}$$

In (25) the Lagrange's multiplier μ was identified using the fact that the $n^*(\alpha,c)$ add to one.

The determination of the MEM frequency distribution $n^*(\alpha,c)$ still requires the identification of the m Lagrange's parameters $(\lambda_{p_1}^*, \ldots, \lambda_{p_m}^*)$ that satisfy the linear constraints (21). When the formal solution (25) for $n^*(\alpha,c)$ is substituted in (21), a system of m coupled, nonlinear, implicit equations results for the m unknown λ_p^*. To solve this system, we consider an objective function F defined by [Alhassid et al., 1978; Agmon et al., 1979]

$$F(\lambda_{p_1}, \ldots, \lambda_{p_m}) = \ln Z(\lambda_{p_1}, \ldots, \lambda_{p_m}) \tag{27}$$

where Z is given in (26). It can be shown [Alhassid et al., 1978] that F has a positive definite hessian at any point $(\lambda_{p_1}, \ldots, \lambda_{p_m})$ if the constraints (21) are linearly independent. Under this condition and provided that there exists a set of Lagrange's multipliers that minimizes F, the minimum is unique and global. Setting the partial derivatives of (27) with respect to the λ_p to zero, it is easy to verify that the conditions for the minimum are identical with the m linear constraints (21). We have indeed

$$\frac{\partial F}{\partial \lambda_p} = - <A_p> = 0 \tag{28}$$

$$\text{for } p = p_1, \ldots, p_m$$

It follows that the set of Lagrange's multipliers minimizing F corresponds also to the solution $(\lambda_{p_1}^*, \ldots, \lambda_{p_m}^*)$ of the constraints (21). Furthermore, the minimal value of the objective function $F(\lambda_{p_1}^*, \ldots, \lambda_{p_m}^*)$ is equal to the constrained maximum of the entropy $S^* = S(n^*(\alpha,c))$. Indeed, upon substitution of $n^*(\alpha,c)$ (25) into the formula (23) defining the entropy and using the stationarity condition (28) we have

$$S^* = F(\lambda_{p_1}^*, \ldots, \lambda_{p_m}^*) = \ln Z(\lambda_{p_1}^*, \ldots, \lambda_{p_m}^*) \tag{29}$$

The minimization of the objective function F is performed using a combination of the steepest descent and Newton's method [Gill et al., 1981]. Failure to converge may result from linear dependence of the constraints (21). This problem is avoided by eliminating some of the constraints after testing for their

linear dependence using a Gram-Schmidt orthogonalization [Alhassid et al., 1978]. The numerical procedure seeking the MEM distribution honouring exactly the data is suitable when the number of constraints, m, is small and when the data are noiseless. In this work, the maximum value of m is on the order of 25, and the experimental errors in the data are negligeable. Many other applications, such as image reconstruction, deconvolution of radioastronomical data, crystallographic inversion, deal with large volumes of noise contaminated data. In that case, exact fitting of the data is inappropriate. The constrained maximization can then be reformulated in terms of weak constraints that are not reproduced exactly by the MEM distribution [Ables, 1974; Wernecke and D'Addario, 1977; Gull and Daniell, 1978; Wilkins et al., 1983].

We saw that the MEM provides with the most uniform crack spectrum consistent with the data. The uniform distribution can be interpreted as representing a state of null information ($m = 0$ in equation (24)) or of 'complete ignorance' about the discrete crack spectrum [Jaynes, 1968; Tarantola and Valette, 1982]. In reality, the crack parameters α and c vary over a continuum of values and the discretization is introduced for computing purposes. The extension of the MEM to continuous distributions must be done with care as Shannon and Weaver's entropy is no longer the appropriate information measure [Jaynes, 1968; Hobson, 1971; Rietsch, 1977; Shore and Johnson, 1980]. For continuous distributions we can not, in general, represent the state of null information by a uniform distribution. This choice does not guarantee that the formulation of the problem is consistent with respect to natural changes of variables. If the parameters α and c are uniformly distributed, then other natural parameters for the problem such as the crack area αc^2 or α^{-1} are not and the level of information appears to depend on the chosen parametrization. To eliminate this inconsistency, we must require that the form of the prior distribution

representing the state of null information is invariant under certain changes of parametrization. The state of null information about the continuous positive variables α and c is chosen by assigning equal frequency of occurrence to the logarithm of the variables. This choice, known as Jeffrey's rule [Jaynes, 1968: Tarantola and Valette, 1982], guarantees that the product, $c^x \alpha^y$, of any power x and y of the two independent log uniformly distributed variables α and c is also log uniform. The practical consequence of this remark for the inversion is that we divide the two-dimensional space log α-log c into a collection of N_α-N_c elementary rectangular cells of equal area (Figure 4a). The crack spectrum $n^*(\alpha,c)$ defined in (25) will simply give the frequency of occupation of the different cells in this logarithmic space.

5. Crack Spectrum in Westerley Granite

Results of the Inversion

The MEM is now used to estimate the crack spectrum in Westerly granite from measurements of the elastic and transport coefficients under pressure. Figures 4a-4d show the evolution of the MEM spectrum for tapered cracks when the number of experimental constraints m is progressively increased. The data $<A_p>$ given in Table 1 are added in the inversion in order of decreasing pressure. This sequence of crack spectra illustrates well the criterion of maximum uniformity underlying the MEM. With increasing m the range of crack parameters compatible with the data narrows down, the entropy decreases monotonically, and the crack spectrum departs more and more from the original uniform distribution (Figure 4a). The relative entropy s given in Figure 4 is defined as the ratio $S(n^*(\alpha,c))/ln(N_\alpha N_c)$, where the denominator is the entropy of the uniform distribution corresponding to the state of null information $m = 0$. In Figure 4b, all the experimental data correspond to pressures $p \geq 200$

MPa and the associated MEM crack spectrum is still uniform for all cracks with $\ln(\alpha) \leq -2.5$. This uniformity expresses simply equal uncertainty about the frequency of occurrence of cracks closing at $p \approx \alpha E \leq 200$ MPa (equation (7)). Indeed, the transport or elastic coefficients measured at a certain pressure level are not sensitive to the dimensions of the cracks that are closed at that pressure. In Figure 4b the MEM gives then naturally equal frequency of occurrence to all the thin cracks and expresses the fact that their dimensions can not be distinguished from the given data. This tendency of the MEM distribution to spread as uniformly as possible is useful in deciding how finely to partition the parameter space in relation with the resolving nature of the data. The MEM gives equal weight to all cells of the parameter space that cannot be differentiated from the available constraints. In the absence of noise, spurious details for which there is no evidence in the data will not appear in the crack spectrum. Going from Figure 4b to 4d, we observe the extension to smaller α values of a linear trend in the spectrum. This evolution underlines the opening of the thinner cracks as the pressure is reduced. When the low-pressure information is taken into account, a large decrease of the entropy arises, and the crack spectrum becomes more sharply defined. The large decrease of s reflects the constraining nature on the spectrum of the large variations of the rock properties at low stresses.

The MEM spectrum (25) has the form of a product of exponentials, and each term in the product corresponds to a specific constraint $<A_p>$. The magnitudes of the Lagrange's multipliers control the smoothness of the spectrum. An informative constraint $<A_p>$ receives a Lagrange's multiplier of large magnitude. A large positive (or negative) λ_p^* weights preferentially the values (α, c) for which $A(\alpha, c, p) << 0$ $(or >> 0)$ and a significant decrease of s results. A redundant or noninformative datum is given a small λ_p^* which weights

evenly all (α,c) in the spectrum, and the entropy is not reduced substantially.

The sensitivity of the spectrum to the shape of the cracks was investigated by performing the inversion for cracks with elliptical cross sections. The spectrum for elliptical cracks shown in Figure 5 was also estimated from all the data in Table 1. It is similar to the spectrum calculated for the case of tapered cracks (Figure 4d). We conclude that the inversion is not very sensitive to the difference between the deformation rate of tapered (equation (3)) and elliptical (equation (4)) cracks. For cracked rocks like Westerly granite with a broad aspect ratio distribution the macroscopic response under confining stresses is controlled by the pressure at which the cracks close rather than by their exact deformation rate. The inverted spectrum is then expected to be similar for all convex cracks with smooth walls that close at a pressure on the order of αE. A close examination of Figure 5 shows that the maxima occur at slightly larger α values than in Figure 4d. This stems from the fact that for a given α an elliptical crack closes at smaller pressure than a tapered crack (equations (7) and (8)). For elliptical cracks the entropy s of the spectrum is larger than for tapered cracks. The length of an elliptical cavity does not substantially shorten under pressure ($C(p) \approx c$ in equation (4)) so that the pressure-dependent data are less informative about the spectrum of elliptical cracks.

The effect of the crack length l was also analyzed. In Figures 4 and 5, all the tubular cracks were assigned a length $l = 35\ \mu$m. Several inversions were performed for different values of l. With l increasing from 20 to 50 μm, the main features of the spectrum are unchanged except for an overall translation of approximately one-fourth of an order of magnitude toward larger c values. This effect results from the dependence of all the constraints on the ratio between c and l. Specifically, as the crack density N_V is proportional to l^{-3}, porosity,

compressibility, and conductivity are function of c^2/l^2, while permeability depends on the ratio c^4/l^2. In principle, l could be considered as a third variable parameter with a spectrum of allowed values. But as the crack deformation model does not account for the change of l with pressure and as all the constraints depend on $1/l^2$, this supplementary degree of freedom would not be resolved in the inversion.

Finally, the effect of the average coordination number $\bar{z}$ was investigated. Figures 4 and 5 correspond to $\bar{z}$=6. With $\bar{z}$ varying between 4 and 6, no substantial difference in the distribution $n^*(\alpha, c)$ was observed. It is easy to see from (16) that a small increase of $\bar{z}$ does not enhance markedly the transport coefficients of a rock like Westerly granite where the crack conductances have a wide range of values.

Comparison Between Inverted and Measured Crack Spectra

The MEM crack spectrum is now compared with direct experimental measurements of crack dimensions. Using scanning electron micrographs of Westerly granite, Hadley [1976] estimated the crack length and aspect ratio distribution from a population of 344 cavities in an area of about 1 mm^2. Figure 6 shows a perspective contour of this experimental crack spectrum. Figure 7a shows a perspective contour of the inverted spectrum represented in figure 4d. Several remarkable similarities exist between the two spectra: (1) the clustering of the two spectra about a line inclined at 45^o, (2) the correlation between the position of the maxima in the two spectra, and (3) the continuous spread of α and c over the same range of more than 3 orders of magnitude. Some differences also exist: (1) overall, the MEM spectrum predicts cracks with smaller α, (2) the MEM spectrum predicts some longer cracks (labeled 2 in Figure 7a), (3) the MEM spectrum is more sharply peaked, and (4) a small cluster of cavities (labeled 3 in

Figure 7a) does not appear in the experimental spectrum.

The most striking common feature is the negative correlation existing between the crack parameters. The two distributions tend to be symmetrical and concentrated about a line inclined at 45^o and given by

$$\log b_{ME}\ (\mu m) = \log \alpha + \log c \approx -1.6 \tag{30}$$

for the MEM distribution and by

$$\log b_{Ha}\ (\mu m) = \log \alpha + \log c \approx -1.3 \tag{31}$$

for the distribution measured by Hadley. The small spacing between the two parallel lines shows that the MEM distribution is translated to smaller aspect ratio with respect to the experimental distribution and that it predicts more compliant cracks than they are in reality. This discrepancy results from neglecting interactions in the calculation of crack deformations. The effect of adjacent cracks is to reduce the Young's modulus of the material surrounding a crack so that an interacting crack closes at lower confining stresses (equation (7)). Consequently, when crack interactions are considered, larger α cracks are necessary to explain the pressure-dependent data.

The main modes of the MEM spectrum (labelled 1 and 2 Figure 7a) occur at the edges of the diagonal feature. Mode 1 is also observed in the experimenal spectrum (Figure 6). Mode 2 corresponds to very long flat cracks. Only the flank of this second maximum is apparent in the experimental distribution. As the area of the micrograph studied by Hadley [1976] is only 1 mm in diameter, the very long cracks corresponding to the second mode may have been missed. Using a linearized least squares inversion of elastic data, Cheng and Toksöz [1979] obtained also a bimodal aspect ratio spectrum for Westerly granite. But their maxima are located at slightly lower α values. This difference follows from using in their inversion dynamic rather than static moduli, the latter being

substantially larger at low p_c [Simmons and Brace, 1965].

The modes in the experimental spectrum are less pronounced than in the calculated spectrum. There are two reasons for this difference. First, the SEM study was based on a collection of only a few hundred cracks. If a great number of cracks were counted in Westerly granite, the magnitude of the maxima would be enhanced. Second, as a consequence of the small number of cracks involved in Hadley's work, the crack parameter space was partitioned into much fewer classes. The SEM spectrum is then naturally smoother.

Finally, the group of rounder cavities labeled 3 in Figure 7a does not exist in the experimental measurements. This group is related to the behavior of the granite at high pressure (Figures 4b-4c). This spurious feature results certainly from the approximate nature of our model of complete crack closure under pressure. Real cracks retain a small but finite conductance at high pressure. Neglecting this effect results in overestimating the population of round cavities.

Interpretation of the Spectrum from a Model of Crack Growth

The clustering of the two spectra about a diagonal line (eq. (30) and (31)) indicates the existence of an approximately constant crack width $2b_{Ha} = 2\alpha c \approx 0.1\mu m$ in Westerly granite. This feature can easily be understood from a simple model of crack formation in granitic rocks. The origin of cracks must be found in the thermal history of the rock as well as in its mineral composition. SEM observations [Sprunt and Brace, 1974] show that microcracks in Westerly granite occur mainly at the boundaries between quartz grains and other minerals. The thermal expansivity contrast existing between quartz and other grains is believed to be responsible for the creation of microfissures. The microcrack growth is driven by intergranular stresses that are produced by the

cooling which arises when granite, formed at depth in the earth, is progressively uplifted to the surface [Nur and Simmons, 1970; Bruner, 1984]. The occurrence of a constant crack width $2b_{H_0}$ suggests that a crack, initiated by the separation of two grains, propagates along the grain boundary without changing its aperture.

The observed crack aperture is determined by the average grain diameter which is on the order of 2R = 750 μm in Westerly granite. A rough estimate of $2b$ is obtained by considering the porosity, in the form of a spherical shell of aperture ΔR = 2b, generated by the differential thermal contraction of a quartz grain of radius R. For a typical temperature decrease $\Delta T = 6 \times 10^2$ ^{o}C and thermal expansivity contrast $\Delta\gamma = 2 \times 10^{-5}$ $^o C^{-1}$ we have [Nur and Simmons, 1970]:

$$2b \approx R \left\{ 1 - (1 - 0.1\ \Delta\gamma\Delta T)^{1/3} \right\} \tag{32}$$

which for R = 375 μm gives an aperture on the order of 0.5 μm in agreement with the observed value.

It is now clear that the diagonal trend in the two crack size distributions represents the path of evolution of cracks during cooling as they extend along grain boundaries and coalesce with other cracks (Figures 7a and 7b). The initial small microfissures have lengths of a few micrometers close to the main mode in the spectrum (crack of type 1 in Figure 7). They then possibly grow from the tips to a maximum length $2c$ on the order of the grain diameter (type 2 in Figure 7). As not all the cracks extend during cooling, the spectrum shows cracks at different stages of evolution ranging from short round openings (type 1) to very long sheetlike cracks (type 2).

Figure 8 illustrates the variation of porosity with pressure calculated from equation (10) and from the inverted tapered crack spectrum (Figure 4d). Figure

8 shows that more than half the initial porosity persists at pressure as high as 10^3 MPa. Figure 9, 10, and 11 illustrate the pressure dependence of compressibility, conductivity, and permeability, respectively, computed from the same inverted spectrum. The smoothness of interpolation between the data used in the inversion (Table 1) shows that a small number of constraints is sufficient to determine the MEM crack spectrum reproducing the observed pressure changes. Additional constraints in the pressure range already represented in the inversion will not improve the resolution.

At low confining stresses the decrease of the transport coefficients is very pronounced, while at pressures exceeding 100 or 200 MPa the decrease appears more gradual. The dramatic decrease of the transport coefficients at low pressure is controlled by the closure of the long flat cracks which are also the most conducting. The constancy of the crack aperture implies in particular that the crack electrical conductance is inversely proportional to the aspect ratio ($g_e \approx b^2/\alpha \approx cste\ /\alpha$). The sheetlike cracks with $\alpha << 1$ are squeezed closed at low pressure, and the most conducting paths in the crack system are destroyed. At higher pressure the closure of rounder and less conducting cavities affects the transport properties less. A second reason for the two-stage response of Westerly granite under pressure is that the multiple connectivity of the crack system is reduced more sharply at low stresses. Figure 12 shows that the fraction of conducting cracks $f\ (p)$ decreases markedly at low p where a large number of thin cracks are closing. $f\ (p)$ was determined from the MEM aspect ratio distribution for tapered cracks (equation (19)). The positive curvature of $f\ (p)$ is explained by the skewness of the aspect ratio distribution. If $n\ (\alpha)$ was exactly log uniform, $f\ (p)$ would vary as log $(cste\ /p)$, while for a uniform distribution, $f\ (p)$ would be linear. At 10^3 MPa, the predicted fraction of conducting cracks is still on the order of 0.6, well above the critical concentration $f_c \approx 0.25$ for z

= 6. With our model of cracks closing perfectly under pressure, the fraction of round cavities open at high stresses is probably overestimated. In reality, the irregularly shaped thin cracks close only partially, and they still contribute to the conductivity at high pressure.

6. Conclusion

The maximum entropy method is useful in obtaining information about the pore space microstructure from measured bulk properties of rocks. The maximum entropy crack spectrum is the most conservative estimate of the actual distribution of crack dimensions in the sense that it is the most uniform distribution compatible with the data. Departure from uniformity indicates the sensitivity of macroscopic measurements to a particular range of crack dimensions. The MEM crack spectrum in Westerly granite was inferred from measurements made under confining pressure of compressibility, conductivity, and permeability. It was found in good agreement with the spectrum estimated from SEM observations. The wide variability of crack length and aspect ratio contrasts with the existence of an approximately constant crack aperture in the cavity population. The form of the crack spectrum underlines the path of propagation of the microfissures as they extended along grain boundaries during cooling of the granite. The large sensitivity of Westerly granite to confining pressure stems from the closure of the long thin cracks which are the most conducting and compliant cavities in the rock. This study suggests that the classical model of regularly shaped void inclusions deforming elastically is appropriate to describe the behavior of igneous rocks under low confining stresses. The irregularities of the crack walls occur at length scales much smaller than the typical crack aperture at low pressure so that the cracks effectively close under stresses. For the two model cracks studied, the crack shape has only a

small influence on the estimated crack spectrum. From the success of the inversion we also conclude that the effective medium approximation performs well in the pressure range studied. It is suspected that the discrepancies still existing between measured and inverted crack spectra follow from neglecting the roughness of the crack walls which inhibits the crack closure at high pressure and from neglecting crack interactions in the calculation of the deformations.

References

Ables, J., Notes on maximum entropy spectral analysis, *Astron. Astrophys. Suppl., 15,* 383-393, 1974.

Agmon, N., Y. Alhassid, and R.D. Levine, An algorithm for finding the distribution of maximum entropy, *J. Comp. Phys., 30,* 250-258, 1979.

Alhassid, Y., N. Agmon, and R.D. Levine, An upper bound for the entropy and its application to the maximal entropy problem, *Chem. Phys. Lett., 53,* 22-26, 1978.

Batzle, M.L., G. Simmons, and R.W. Siegfried, Microcrack closure in rocks under stress: direct observation, *J. Geophys. Res., 85,* 7072-7090, 1980.

Brace, W.F., Some new measurements of linear compressibility of rocks, *J. Geophys. Res., 70,* 391-398, 1965.

Brace, W.F., Permeability from resistivity and pore shape, *J. Geophys. Res., 82,* 3343-3349, 1977.

Brace, W.F., A.S. Orange, and T.R. Madden, The effect of pressure on the electrical resistivity of water-saturated crystalline rocks, *J. Geophys. Res., 70,* 5669-5678, 1965.

Brace, W.F., J.B. Walsh, and W.T. Frangos, Permeability of granite under high pressure, *J. Geophys. Res., 73,* 2225-2236, 1968.

Bruner, W, Crack growth during unroofing of crustal rocks: effects of thermoelastic behavior and near-surface stresses, *J. Geophys. Res., 89,* 4167-4184, 1984.

Cheng, C.H., and M.N. Toksöz, Inversion of seismic velocities for the pore aspect ratio spectrum of a rock, *J. Geophys. Res., 84,* 7533-7543, 1979.

Gill, P.E., W. Murray, and M.H. Wright, *Practical Optimization,* p. 401. Academic, London, 1981.

Gull, S.F., and G.J. Daniell, Image reconstruction from incomplete and noisy data, *Nature, 272,* 686-690, 1978.

Hadley, K., Comparison of calculated and observed crack densities and seismic velocities in Westerly granite, *J. Geophys. Res., 81,* 3484-3494, 1976.

Hobson, A., *Concepts in Statistical Mechanics,* p. 172, Gordon and Breach, New York, 1971.

Jaynes, E.T., Information theory and statistical mechanics, *Phys. Rev., 106,* 620-630, 1957.

Jaynes, E.T., Prior probabilities, *IEEE Trans. Syst. Sci. Cybern., 4,* 227-241, 1968.

Kirkpatrick, S., Percolation and conduction, *Rev. Mod. Phys., 45,* 574-588, 1973.

Mavko, G.M., and A. Nur, The effect of nonelliptical cracks on the compressibility of rocks, *J. Geophys. Res., 83,* 4459-4468, 1978.

Nur, A., and J.D. Byerlee, An effective stress law for elastic deformation of rocks with fluids, *J. Geophys. Res., 76,* 6414-6419, 1971.

Nur, A., and G. Simmons, The origin of small cracks in igneous rocks, *Int. J. Rock Mech. Min. Sci., 7,* 307-314, 1970.

O'Connell, R.J., and B. Budiansky, Seismic velocities in dry and saturated cracked solids, *J. Geophys. Res., 79,* 5412-5426, 1974.

Rietsch, E., The maximum entropy approach to inverse problems, *J. Geophys., 42,* 489-506, 1977.

Seeburger, D.A., and A. Nur, A pore space model for rock permeability and bulk modulus, *J. Geophys. Res., 89,* 527-536, 1984.

Shannon, C.E., and W. Weaver, *The Mathematical Theory of Communication.* p. 117, University of Illinois, Urbana, 1949.

Shore, J.E., and R.W. Johnson, Axiomatic derivation of the principle of maximum entropy and the principle of minimum cross-entropy, *IEEE Trans. Inform. Theory, 26,* 26-37, 1980.

Simmons, G., and W.F. Brace, Comparison of static and dynamic measurements of compressibility of rocks, *J. Geophys. Res., 70,* 5649-5656, 1965.

Sprunt, E.S., and W.F. Brace, Direct observation of microcavities in crystalline rocks, *Int. J. Rock Mech. Min. Sci. Geomech. Abstr., 11,* 139-150, 1974.

Tarantola, A., and B. Valette, Inverse problems = quest for information, *J. Geophys., 50,* 159-170, 1982.

Tolman, R.C., *The Principles of Statistical Mechanics,* p. 661, Oxford University Press, New York, 1938.

Tribus, M., *Thermostatics and Thermodynamics,* p. 649, Van Nostrand, New York, 1961.

Walsh, J.B., The effect of cracks on the compressibility of rock, *J. Geophys.*

Res., 70, 381-389, 1965.

Walsh, J.B., Static deformation of rock, *J. Eng. Mech. Div., ASCE, 106,* 1005-1019, 1980.

Walsh, J.B., and W.F. Brace, The effect of pressure on porosity and the transport properties of rock, *J. Geophys. Res., 89,* 9425-9431, 1984.

Walsh, J.B., and M.A. Grosenbaugh, A new model for analyzing the effect of fractures on compressibility, *J. Geophys. Res., 84,* 3532-3536, 1979.

Wernecke, S.J., and L.R. D'Addario, Maximum entropy image reconstruction, *IEEE Trans. Comput. 26,* 351-364, 1977.

Wilkins, S.W., J.N. Varghese, and M.S. Lehmann, Statistical geometry. I. A self-consistent approach to the crystallographic inversion problem based on information theory, *Acta Cryst., A39,* 47-60, 1983.

Zimmerman, R.W., The effect of pore structure on the pore and bulk compressibilities of consolidated sandstones, Ph.D. thesis, University of California, Berkeley, 1984.

Table 1

Static compressibility, normalized conductivity, permeability and porosity
of Westerly Granite
as a function of pressure (from Brace, 1965; Brace et al, 1965, 1968).

p (Mpa)	β^* ($10^{-5} Mpa^{-1}$)	$\frac{\sigma^*}{\sigma_f}$ x 10^4 (#)	κ^* ($10^{-9} \mu m^2$)	ϕ (%)
0	8.3	-	-	0.9
2.5	7.6	-	-	
5.0	6.8	9.68	345.	
10	5.4	-	-	
20	3.8	-	-	
25	-	4.62	116.	
50	2.89	-	62.	
100	2.46	2.14	35.	
200	2.16	1.20	15.3	
400	-	0.612	4.2	
500	1.99	-	-	
600	-	0.37	-	
1000	-	0.17	-	

Figure legends

Figure 1. In the absence of stress, the pore space is represented by a fully interconnected network of tubular cracks of approximately constant length l but variable cross-sectional half length c and half width b.

Figure 2. Tubular crack of length l with a tapered cross section. c and b are the half length and the half width, respectively, of the crosssection in the absence of stress.

Figure 3. Tubular crack of length l with an elliptical cross section.

Figure 4. Evolution of the maximum entropy spectrum for tapered cracks in Westerly granite as the number of constraints m is increased; s is the relative entropy of the spectrum. The pressure range indicated is that of the experimental data used in each inversion (See Table 1). The underlying grid has (N_α= 65) x (N_c = 40) nodes.

Figure 5. Maximum entropy spectrum for elliptical cracks in Westerly granite; s is the relative entropy of the spectrum. All the data given in table 1 were used in this inversion. The underlying grid has (N_α= 65) x (N_c = 40) nodes.

Figure 6. Contouring of the experimental spectrum measured by Hadley [1976] in Westerly granite. The original data divided into 9x7 classes were interpolated on a 65x40 grid to allow the comparison with the inverted spectrum.

Figure 7. (a) Contouring of the inverted spectrum for tapered cracks in Westerly granite. This figure represents the same spectrum as Figure 4d. The contouring interval is 0.005. (b) During cooling of the granite, cracks of type 1 may grow,merge with others and produce very long cracks of type 2 extending over a large portion of the grain boundary.

Figure 8. Porosity of Westerly granite as a function of confining pressure. This prediction is calculated from the maximum entropy spectrum of tapered cracks.

Figure 9. The solid line is the maximum entropy interpolation of the compressibility of Westerly granite as a function of confining pressure. This curve is calculated from the inverted spectrum of tapered cracks. The circles are the experimental data used in the inversion.

Figure 10. The solid line is the maximum entropy interpolation of the normalized electrical conductivity of Westerly granite as a function of pressure. This curve is calculated from the inverted spectrum of tapered cracks. The circles are the experimental data used in the inversion.

Figure 11. The solid line is the maximum entropy interpolation of the permeability of Westerly granite as a function of pressure. This curve is calculated from the inverted spectrum of tapered cracks. The circles are the experimental data used in the inversion.

Figure 12. Pressure dependence of the fraction of open cracks in Westerly granite. This curve is calculated from the inverted spectrum of tapered cracks.

Figure 1

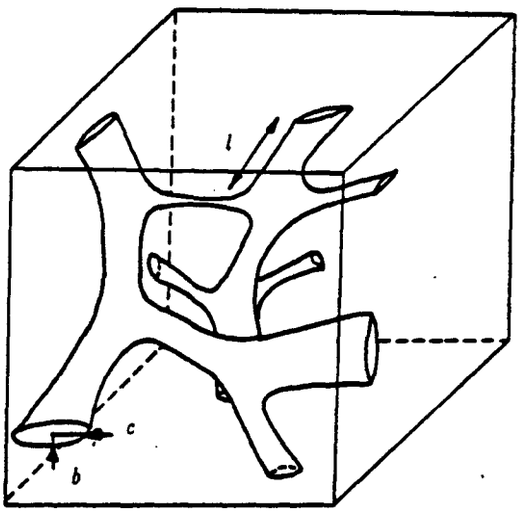

Figure 2

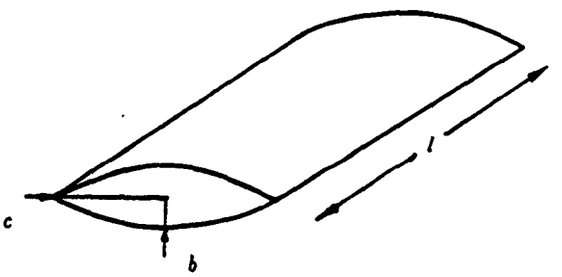

Figure 3

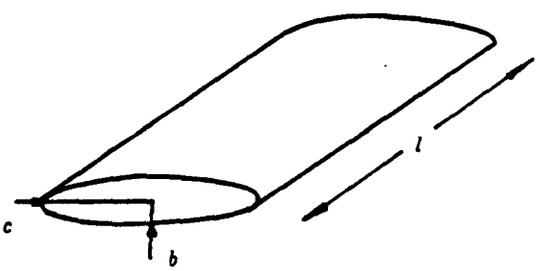

$s = 1.0$

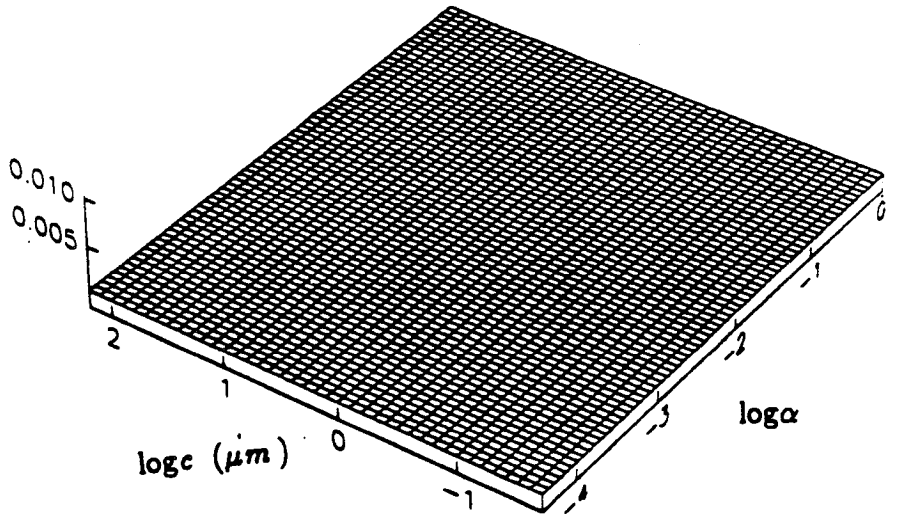

(a)

Figure 4

$s = 0.94 \qquad p \geq 200\ MPa$

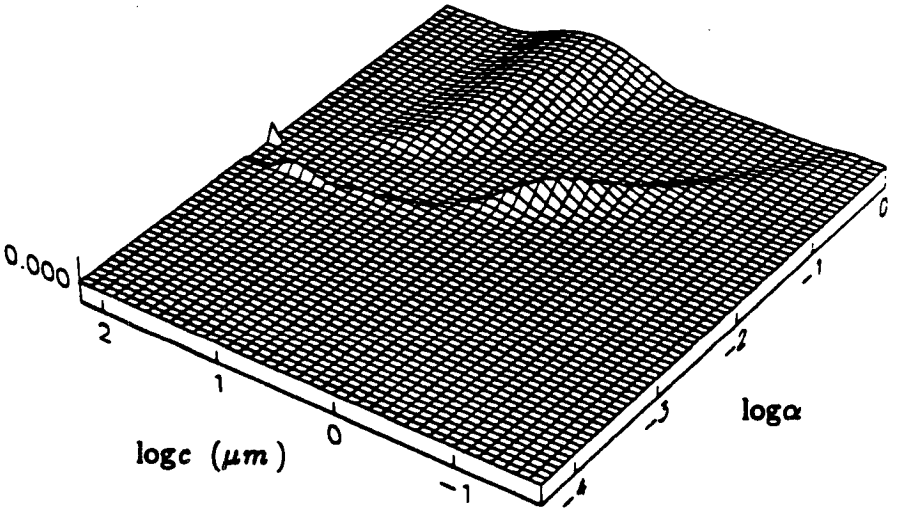

(b)

$s = 0.90 \qquad p \geq 25\ MPa$

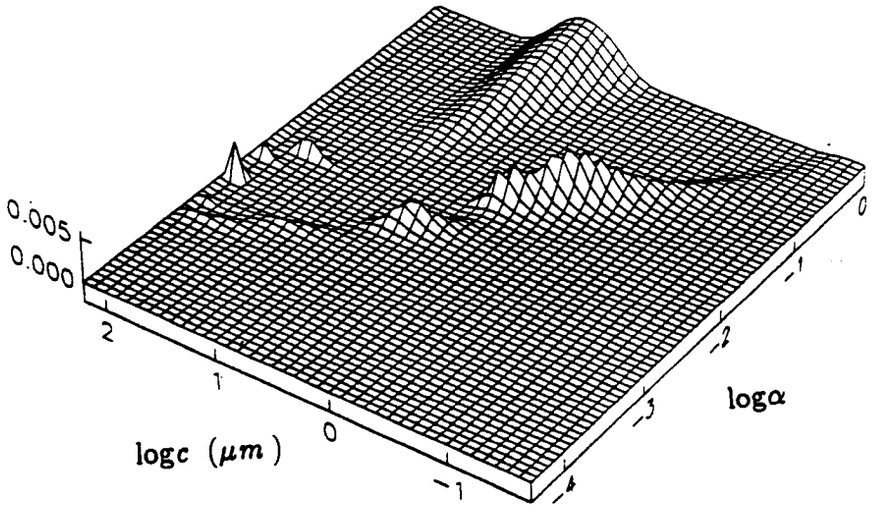

(c)

Figure 4

$s = 0.75 \qquad p \geq 0\ MPa$

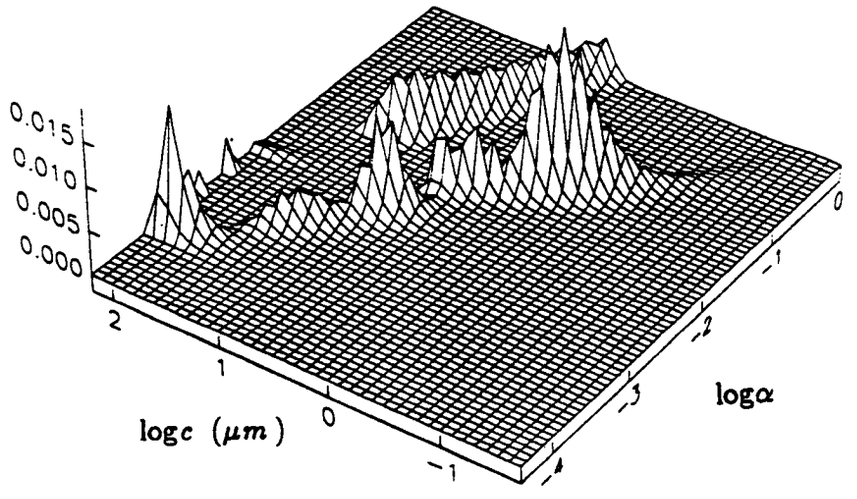

(d)

$$s = 0.81 \qquad p \geq 0\ MPa$$

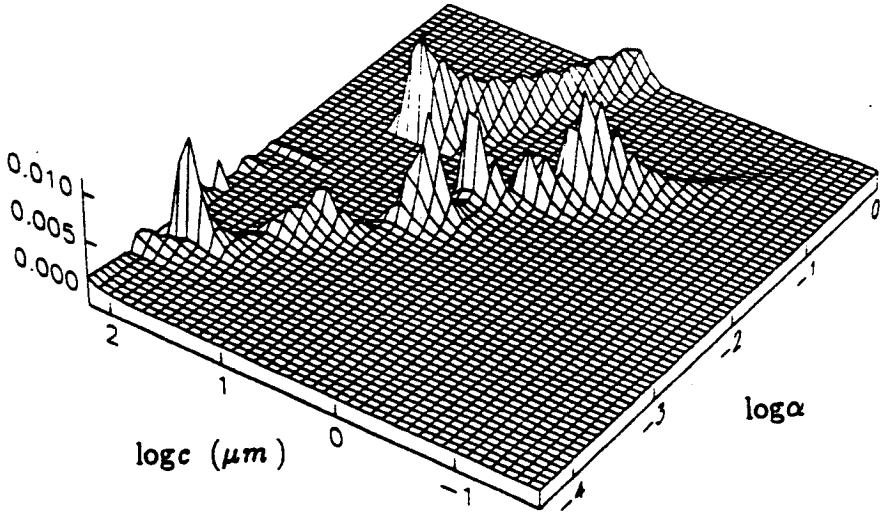

Figure 5

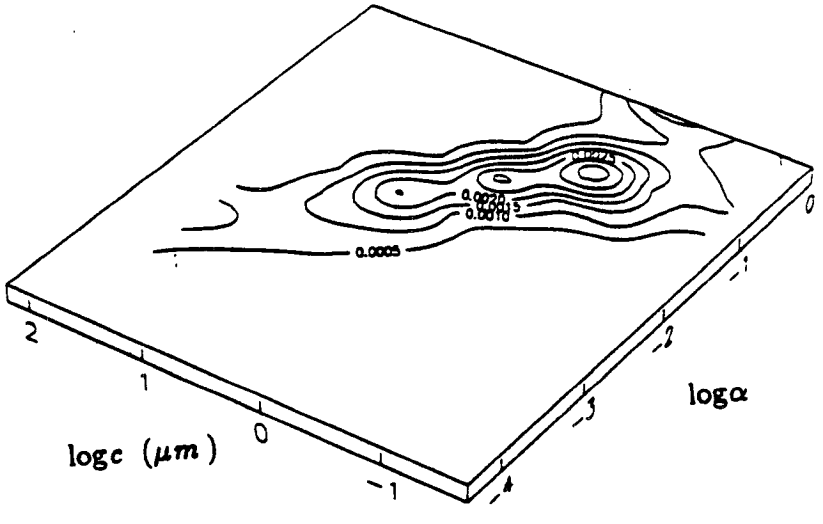

Figure 6

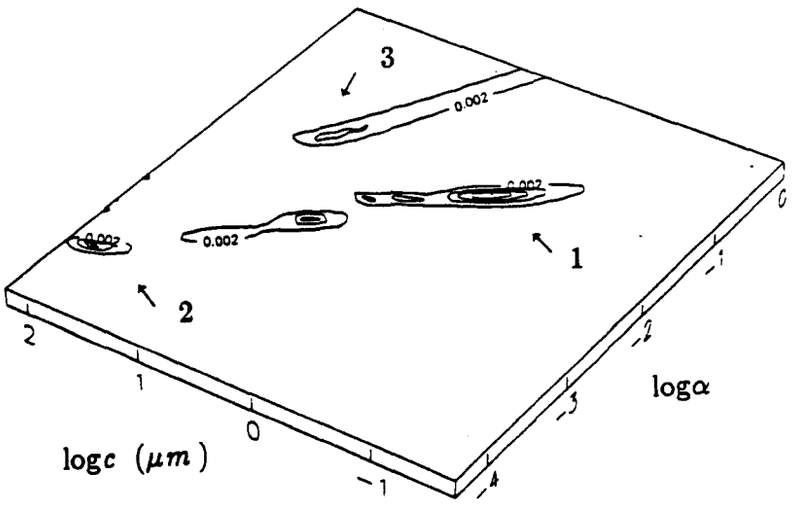

(a)

Figure 7

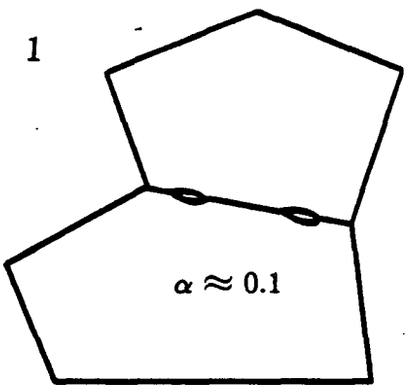

(b)

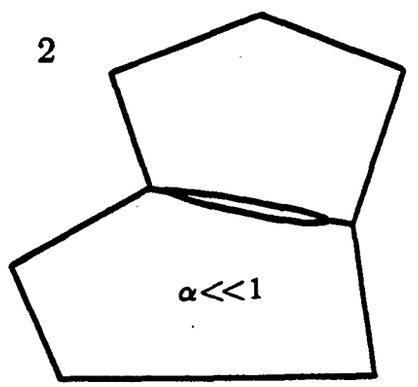

Figure 8

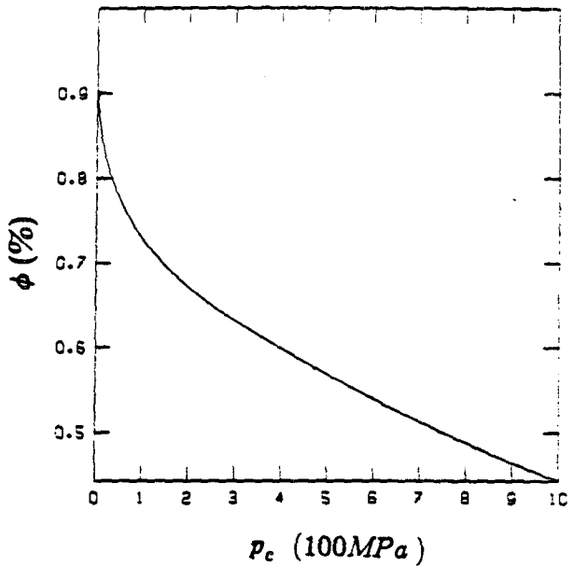

Figure 9

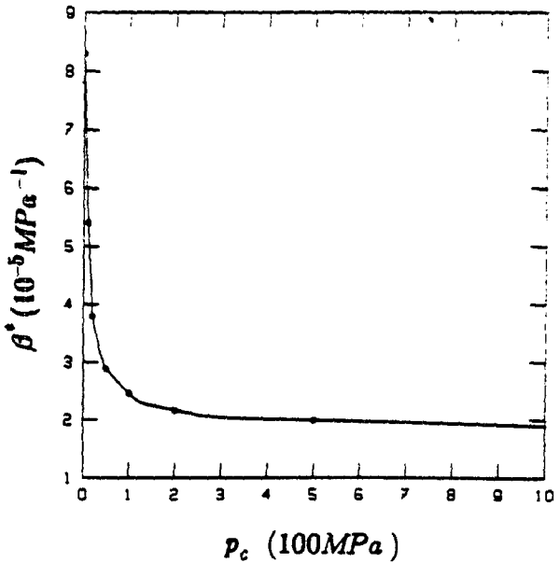

Figure 10

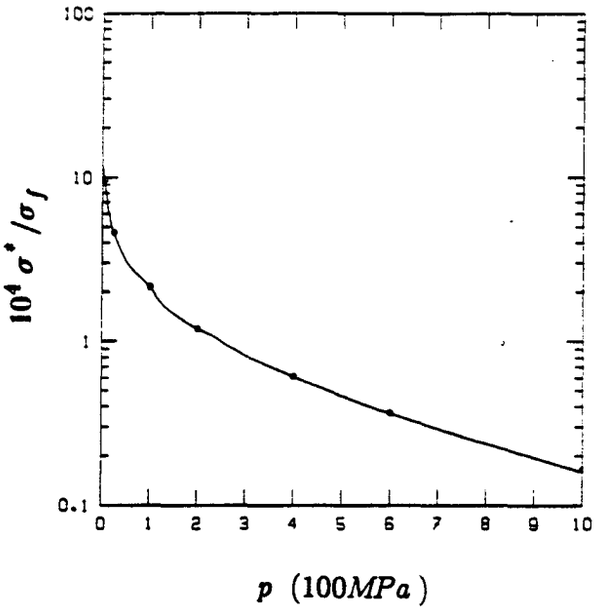

Figure 11

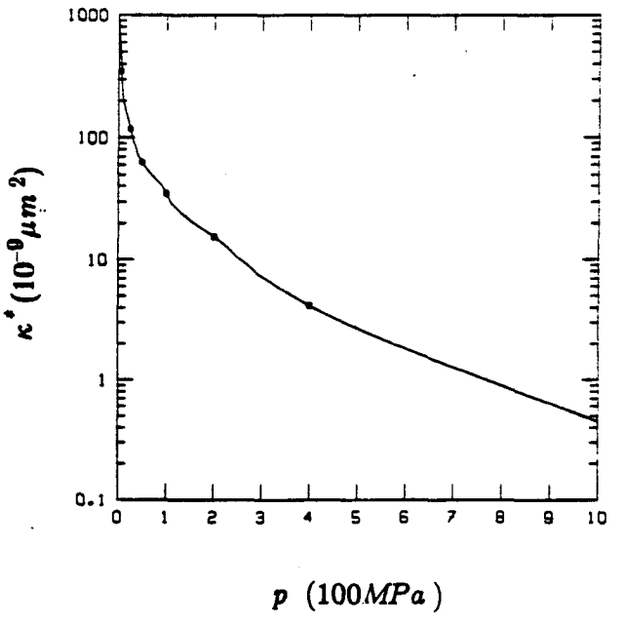

Figure 12

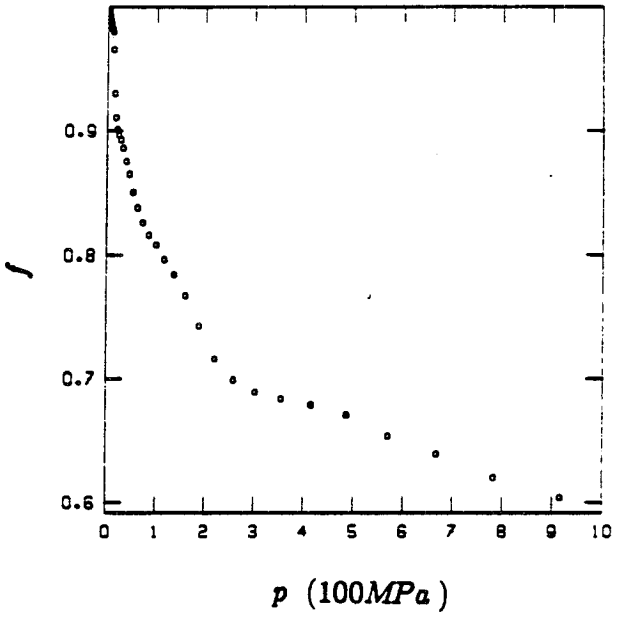

CHAPTER 4:

POROSITY MAPPING FROM SEISMIC VELOCITY DATA, AN APPROACH BASED ON SPATIAL CORRELATION FUNCTIONS

Abstract

A linear mean square estimation technique is presented for the mapping of porosity from seismic interval velocity data. The pattern of lateral variations of porosity and seismic transit time in the reservoir interval are first characterized by spatial correlation functions which are inferred from the well and seismic data. The porosity estimates are then expressed as weighted averages of porosity and transit time observations at nearby sample points. Based on the correlation structure and on the data configuration, the weights values are determined which minimize the mean square prediction error. The estimation technique is first tested on a numerically simulated reservoir model. Next, it is applied to the mapping of porosity in an oil-bearing channel-sand reservoir in Alberta. In each case, the areal distribution of porosity is first reconstructed from sparse porosity well measurements alone. It is next estimated from the interval transit time data by using a conventional least-squares procedure which ignores the lateral continuity in the variations of the reservoir parameters. Finally the porosity spatial distribution is predicted by combining linearly the transit time and porosity observations in a way which takes into consideration the actual correlation structure in the reservoirs. Compared with the well-derived mapping and with the standard seismically assisted mapping, the correlation-based reconstruction integrating well with seismic information gives rise to a far more detailed and accurate picture of the areal porosity distribution even in zones where no well control is available.

1. Introduction

The spatial description of petrophysical properties like porosity, permeability and state of saturation in oil-bearing reservoirs is of crucial importance for the forecasting of the reservoir performances as well as for the planning of the

production operations. Well-log and core measurements provide with an accurate sampling of the desired reservoir characteristics. But the information collected at the drilling sites is usually too fragmentary to give an accurate image of the reservoir heterogeneities which control the oil recovery operations. The limited depth of investigation of the logging tools, the smallness of the cored volume and the sparse distribution of drilled holes explain this lack of spatial resolution.

High resolution seismic methods can be used to obtain a detailed spatial sampling of the acoustical properties of the reservoir interval. The seismic attributes characterizing the reservoir zone, in particular the interval velocities, are known to be affected by variations in reservoir properties. The integration of the seismic measurements with the well and core data appears then naturally as one potential way of mapping the lateral changes of reservoir parameters like porosity with adequate resolution in zones where well control is not available. To this end, the spatial interdependence between the seismically derived interval velocities and the well porosities must first be modelled.

Conventional methods (Maureau and Van Wijhe, 1979; Angeleri and Carpi, 1982; De Buyl et al., 1986) to estimate porosity spatial variations from seismic data are based on empirical relations like Wyllie's time-average formula (Wyllie et al, 1958) or on regression equations between porosity and interval transit time. In these standard approaches, the seismic or well observations at one location in the reservoir are treated as being statistically independent of measurements made at other spatial positions. This amounts to assuming that the spatial variability of the reservoir characteristics is completely random. In this study, we propose instead a porosity mapping technique which uses spatial correlation functions (Matheron, 1965; Agterberg, 1970; Journel and Huijbregts,

1978; Ripley, 1981; Vanmarcke, 1983) to account for lateral continuity and structure in the spatial variations of rock properties. The mapping technique is tested on a two-dimensional reservoir model. A real case study is also presented.

In the second section, a numerical simulation method is used to generate the areal porosity distribution in the reservoir interval. A fictitious drilling program in the modeled oil field provides with sparse porosity observations. In addition, a simulated seismic survey across the reservoir yields the areal distribution of the transit time in the producing interval. The information gathered from the seismic survey and from the drilling campaign must then be combined to reconstruct the porosity spatial distribution in the simulated reservoir model. To this end, the patterns of variation of porosity and transit time across the reservoir are summarized by constructing spatial correlation functions from the well and seismic data. In particular, the spatial cross-correlation is used to model the transit time sensitivity to changes of porosity. In the third section, based on the correlation structure, linear mean square porosity estimates are derived which integrate the seismic with the well information. In section 4, the porosity areal distribution in the simulated reservoir model is first predicted from the well data alone. It is also estimated from the seismic data by using a conventional least-squares fitting procedure to the cross-plot transit time against porosity. The simulated porosity map is next reconstructed by combining porosity and transit time observations in a way which takes advantage of the spatial correlation structure. Finally, comparing the reconstructed porosity maps with the simulated porosity model, the performances of the three estimation methods are quantified.

In the last section, the analysis done in section 4 is applied to the areal mapping

of porosity in an oil-bearing reservoir in the Taber-Turin area of Alberta.

2. A statistical reservoir description

A simulation technique described in the appendix was used to generate the areal distribution of porosity p in a tabular sandstone reservoir covering an area of about $10\text{x}10km^2$. Figure 1 represents the porosity surface $p(x,y) = p(\vec{x})$ simulated at the nodes of a 50x50 square grid. The spacing between grid points in the N-S and E-W directions is $\Delta = 200m$. The porosities are average values over the vertical extension of the reservoir zone and (x,y) are the horizontal coordinates of a point at the vertical of the reservoir. The average porosity was measured at a few irregularly spaced fictitious drilling sites whose locations are depicted in figure 2. In addition to the fragmentary porosity information, seismically derived interval transit times in the reservoir layer are assumed to be known at all the nodes of the 50x50 grid covering the entire field. The transit times t are also average values across the known thickness of the reservoir interval. The acoustical measurements provide with a systematic sampling of a second spatial surface $t(\vec{x}) = t(x,y)$ related in some yet unknown way to the porosity surface. The simulated transit time ($\mu\text{sec}/m$) surface is shown in figure 3. In practice, the acoustical velocities in the reservoir interval must be extracted from the bandlimited and noisy seismic data. For thin intervals, this extraction requires the simultaneous determination of the bed thickness from the interfering wavelets associated with the closely spaced reflectors. More will be said about this problem in section 5.

Based on the sparse porosity data and on the more extensive seismic information, we must estimate the porosity areal distribution throughout the model reservoir, even in zones were the porosity is undersampled. To this end, we must first model the spatial variability and interdependence between p and

t. The simulated porosity map exhibits a complicated pattern of spatial variability well characteristic of a real reservoir. Furthermore as in a real reservoir environment, there is no simple relationship between transit time and porosity at the same location. The correlation diagram $t(\vec{x})$–$p(\vec{x})$ shown in figure 4 demonstrates clearly that there is no unique correspondence between porosity and transit time in the simulated reservoir. Considering the complexity of the lateral variations of porosity and the nonunique interdependence between p and t, a deterministic description of the reservoir spatial heterogeneities is inappropriate. Typically however, the irregular spatial variations of the reservoir parameters are neither purely random nor independent but their structure and interdependence are best modeled statistically. Figure 1 shows that porosity values at two neighbouring locations tend on the average to be more similar than they are at two distant positions. Comparing figure 1 and 3 or examining figure 4, we see also that clusters of high (low) porosity tend to coincide spatially with zones of large (small) seismic transit time. We will now see how the structure of variability of the porosity and transit time areal distributions can be summarized by using spatial correlation functions.

In our statistical reservoir description, the spatial distribution of porosity and transit time is interpreted as a particular realization $\{ (p(\vec{x}), t(\vec{x})), \vec{x} \in \textit{reservoir} \}$ of a bivariate random field (r.f.) $\{ (P(\vec{x}), T(\vec{x})), \vec{x} \in \textit{reservoir} \}$ which is simply a collection of random variables (r.v.) indexed by their position $\vec{x}$. The statistical regularity of the porosity surface $p(x, y)$ is then expressed by the positive auto-correlation existing between the random variables P at adjacent locations and the interdependence between p and t is modelled by a positive cross-correlation between the variables P and T.

From a single realization of the random field, the inference of the correlation structure is only possible under a stationarity assumption. We assume that the random field is homogeneous and isotropic (See for example Yaglom, 1962). Practically, the assumption of homogeneity is justified when the data do not exhibit any systematic component of spatial variations over distances much larger than the average sampling interval. The hypothesis of isotropy is appropriate if the data do not indicate a preferential direction of spatial variability. For a homogeneous r.f., the mathematical expectation of $P(\vec{x})$ and $T(\vec{x})$ are independent of the position $\vec{x}$:

$$E\ P(\vec{x}) = m_p \tag{1}$$

$$E\ T(\vec{x}) = m_t \tag{2}$$

and can be estimated respectively by the arithmetic means $\bar{p}$ and $\bar{t}$ of the available data. Homogeneity entails also that the centered correlation between two r.v. defined respectively at $\vec{x}$ and $\vec{x}+\vec{r}$ depends only on the lag $\vec{r}$ and not on the position $\vec{x}$. If we further assume isotropy, the correlation depends on the interdistance r but not on the direction of $\vec{r}$. For the bivariate r.f. $\{P(\vec{x}), T(\vec{x})\}$ we can then define the centered auto- and cross-correlation functions by:

$$C_{pp}(r) = E\,(P(\vec{x}+\vec{r}) - m_p)\,(P(\vec{x}) - m_p) \tag{3}$$

$$C_{tt}(r) = E\,(T(\vec{x}+\vec{r}) - m_t)\,(T(\vec{x}) - m_t) \tag{4}$$

$$C_{pt}(r) = E\,(P(\vec{x}+\vec{r}) - m_p)\,(T(\vec{x}) - m_t) \tag{5}$$

$$C_{tp}(r) = E\,(T(\vec{x}+\vec{r}) - m_t)\,(P(\vec{x}) - m_p) \tag{6}$$

The solid lines in figures 5 to 7 show the normalized correlation functions, C_{pp}/σ_p^2, C_{tt}/σ_t^2 and $C_{pt}/(\sigma_p\,\sigma_t)$, corresponding to the simulated reservoir model. Their analytical expression are given in the appendix (eq. (a-3) and (a-7)). $\sigma_p^2 = C_{pp}(0)$ and $\sigma_t^2 = C_{tt}(0)$ are respectively the variances of the porosity and transit time variables. The means and variances of the bivariate r.f. are given in table 1. The auto-correlations are by definition even functions of r but in

general, the cross-correlations are not. However, practically we do not expect a spatial lag effect in the porosity-transit time relationship and for the correlation model considered here C_{pt} is symmetrical about $r=0$, i.e., $C_{pt}(r)=C_{pt}(-r)=C_{tp}(\pm r)$. We then need only to display C_{pt} for $r \geq 0$. Figures 5 to 7 also show the sample correlation functions calculated from the 50x50 simulated porosity and transit time surfaces. These experimental correlations were calculated for distances $r=n\,\Delta$ which are multiple of the data spacing along lines and columns. A purely random porosity spatial distribution would be evidenced by an experimental correlation function close to a delta function at $r=0$. The positiveness of C_{pp} for distances $r \leq \xi$ is indicative of the spatial continuity of the porosity variations in the reservoir. The zones of high and low porosity form clusters with typical lateral extension on the order of ξ=4km. ξ is called the correlation length or range; it measures the degree of lateral continuity in the porosity areal distribution. The decrease of C_{pp} with increasing r suggests that on the average the porosity takes on closer values at adjacent locations than at two distant points. For distances $r > \xi$, porosity values are no more correlated and the sample correlation function oscillates about zero. The behavior of the correlation function near $r=0$ controls the smoothness of the porosity surface. It can be shown (see for example Yaglom, 1962) that the r.f. $\{P(\vec{x})\}$ is mean square differentiable if $C_{pp}(r)$ has a continuous second derivative at $r=0$. In figure 5, $C_{pp}\,\alpha\, r$ for small r and the porosity surface has a jagged aspect.

The cross-correlation function $C_{pt}(r)$ (figure 7) characterizes the seismic transit time sensitivity to lateral changes of porosity or the joint spatial variability of the two resevoir parameters. The correlation coefficient $C_{pt}(0)/\sigma_p\,\sigma_t$ is equal to 0.7 (table 1). The positive nature of the cross-correlation C_{pt} for $r < \xi$ shows that an increase of p tend to be accompanied by an increase of t.

In practice, the functions $C_{pp}(r)$ and $C_{pt}(r)$ must be estimated from a limited number of irregularly spaced porosity well data. A sample porosity auto-correlation function is obtained as follows. First, the products $c_{ij} = (p(\vec{x}_i) - \overline{p})(p(\vec{x}_j) - \overline{p})$ are formed for all pairs $(\vec{x}_i, \vec{x}_j)$ of data points. Then, the c_{ij} are grouped into distance intervals, $r - \delta \leq |\vec{x}_i - \vec{x}_j| \leq r + \delta$, with tolerance 2δ. Finally, the c_{ij} are averaged in each interval. Figure 5 shows the normalized experimental auto-correlation function calculated from the well data of figure 2. As a result of the small number of data pairs available, the fluctuations about the theoretical correlation model C_{pp} are much more pronounced than in the sample correlation function calculated from the 50x50 grid of porosity values. In practice, the sample correlations constructed from less than 20 to 30 pairs of data should not be considered. We have also seen that the behavior of the correlations at small distances is the most important. A meaningfull porosity auto-correlation function can only be constructed directly if the average well spacing is smaller than the correlation length. Otherwise, the porosity field will appear purely random. If the drilling sites are too sparsely distributed, a correlation model for $C_{pp}(r)$ can still be constructed indirectly from the seismic data. This point will be discussed in the case study presented (section 5) where only 10 wells are available in the reservoir field.

Before concluding this section, the important question of the scale of the observations and that of the adequate resolution in the porosity mapping must be addressed. On the one hand, the core or log-derived porosities integrate the pore volume over a rock domain with dimensions of only a few inches. On the other hand, the transit times measured at seismic frequencies are local averages over a spatial region with dimensions on the order of a few tens of meters. The spatial resolution achieved by the seismic survey determines evidently the maximum attainable resolution in the areal mapping of p. However, the spatial resolution

required in the porosity mapping is dictated by the length scale which controls the oil recovery operations. This scale is usually larger than the resolution afforded by the seismic survey. As a practical example, consider the mapping of the most porous regions in the reservoir. The detection of very localized porous zones has no economical interest. What matters for the production is the delineation of porous areas having large enough lateral extension. Accordingly, the variable P that we consider in the areal mapping represents a local average of the porosity over blocks of horizontal dimensions $\Delta = 200$ m and vertical extension equal to the thickness of the reservoir interval. The grid spacing Δ was taken larger than the subsurface coverage of 20 to 50 meters provided by a typical seismic survey. Additionally in practice, the correlation functions inferred from porosity measurements made on cores may need to be 'regularized' to determine the correlation function of the variable P which represents a local average over a volume much larger that that of a core (Journel and Huijbregts, 1978; Vanmarcke, 1983).

In this section, we have modelled statistically the lateral variations of the reservoir parameters. In particular, the auto-correlation functions summarize quantitatively the complex structure of spatial variability of the reservoir properties. The cross-correlation function provides with a measure of the spatial interdependence between the porosity and transit time surfaces. More generally, spatial cross-correlations are useful to assess the sensitivity of the reservoir acoustical properties not only to porosity but also to other petrophysical properties that need to be mapped. In the next section, the correlation functions will be used to derive risk-qualified porosity estimates which account for the spatial interdependence between the data.

3. Linear mean square estimation

The problem is now to reconstruct the surface $p(x,y)$ (figure 1) from a few irregularly spaced sample points of this surface (figure 2) and from densely and regularly spaced sample points from the transit time surface $t(x,y)$ (figure 3) cross-correlated with $p(x,y)$. We also wish to assess the quality of the estimation procedure. For now, we assume that the functions $C_{pp}(r)$, $C_{tt}(r)$ and $C_{pt}(r)$ are known and we restrict ourselves to linear mean square (LMS) estimators that can be calculated readily from the known correlation functions. The porosity estimates will be weighted averages of p and t values at nearby sample points and the mean square error (MSE) of estimation will be a quadratic function of the weights. We will then select the weight values for which the MSE function takes its minimum.

To simplify the algebra, we assume that the mean porosity and transit time, m_p and m_t, are known and we replace P and T by $P_c = P - m_p$ and $T_c = T - m_t$ respectively. The zero mean centered r.v. P_c and T_c will still be called porosity and transit time. To estimate the value of the r.v. $P_c(\vec{x})$, we form a linear combination of the values of the r.v. $\{ P_c(\vec{x}_i) ; i=1,...,n \}$ at n neighbouring wells and of the values of the r.v. $\{T_c(\vec{x}_j) ; j=n+1,...,n+m \}$ at m adjacent grid nodes. The linear estimator at location $\vec{x}$ is then given by:

$$P_c^*(\vec{x}) = \sum_{i=1}^{n} w_i \; P_c(\vec{x}_i) + \sum_{j=1}^{m} w_{n+j} \; T_c(\vec{x}_{n+j}) \qquad (7)$$

$$= \mathbf{W}^t(\vec{x}) \; \mathbf{Y}(\vec{x})$$

where $\mathbf{Y}(\vec{x}) = [\, P_c(\vec{x}_1) .... P_c(\vec{x}_n) \; T_c(\vec{x}_{n+1}) \; \cdots \; T_c(\vec{x}_{n+m}) \,]^t$ is the data vector and $\mathbf{W}^t(\vec{x}) = [w_1 \; \cdots \; w_{n+m}]$ is the weight vector. Both vectors are function of the position $\vec{x}$ where the porosity is estimated. The components of the random vector $\mathbf{Y}$ correspond to samples points of the porosity and transit

time surfaces in the vicinity of $\vec{x}$. The components of $\mathbf{W}$ depend on the spatial configuration of the data at $\vec{x}$. For the linear estimator P_c^*, the estimation error ϵ is given by:

$$\begin{aligned} \epsilon(\vec{x}) &= P_c(\vec{x}) - P_c^*(\vec{x}) \\ &= P_c(\vec{x}) - \mathbf{W}^t\ \mathbf{Y} \end{aligned} \tag{8}$$

We must now select a weight vector which minimizes some specified average measure of the error ϵ. The mean square error (MSE) has the advantage of being directly expressible in terms of the known second order moments. Taking the expected value of ϵ^2 in (8), we obtain the MSE as:

$$E\,\epsilon^2(x) = \sigma_p^2 - 2E(P_c\ \mathbf{Y}^t)\,\mathbf{W} + \mathbf{W}^t E(\mathbf{Y}\ \mathbf{Y}^t)\,\mathbf{W} \tag{9}$$

The MSE is a quadratic function of the components of the weight vector. The coefficients of the quadratic terms are the components of the symmetric $(n+m)$x$(n+m)$ correlation matrix of the data vector defined by:

$$\mathbf{C}(\vec{x}) = E(\mathbf{Y}\ \mathbf{Y}^t) = \left[\begin{array}{c|c} C_{pp}(\vec{x}_i - \vec{x}_j) & C_{pt}(\vec{x}_i - \vec{x}_{n+j}) \\ \hline C_{tp}(\vec{x}_{n+i} - \vec{x}_j) & C_{tt}(\vec{x}_{n+i} - \vec{x}_{n+j}) \end{array}\right] \tag{10}$$

The coefficients of the linear terms in (9) are the components of the following correlation vector:

$$\begin{aligned} \mathbf{S}^t(\vec{x}) &= E(P_c\ \mathbf{Y}^t) \\ &= [\ C_{pp}(\vec{x}-\vec{x}_1)\ \cdots\ C_{pp}(\vec{x}-\vec{x}_n)\ C_{pt}(\vec{x}-\vec{x}_{n+1})\ \cdots\ C_{pt}(\vec{x}-\vec{x}_{n+m})\ ] \end{aligned} \tag{11}$$

To achieve the smallest MSE, we select the weigth vector $\mathbf{W}^*$ for which the quadratic function (9) takes its minimum. Differentiating (9) with respect to each component of $\mathbf{W}$, we obtain the condition for the stationary point $\mathbf{W}^*$:

$$\mathbf{C}\,\mathbf{W}^* = \mathbf{S} \tag{12}$$

where $\mathbf{C}$, the positive definite correlation matrix is invertible. Substituting the optimal weight vector $\mathbf{W}^* = \mathbf{C}^{-1}\,\mathbf{S}$ in (9), we obtain the minimum MSE as:

$$[\ E\ \epsilon^2(\vec{x})\ ]_{\min} = \sigma_p^2 - \mathbf{S}^t\ \mathbf{W}^* \tag{13}$$

At each point $\vec{x}$ in the reservoir where a porosity estimate is required, we form the weighted average (7) of sample values p_c and t_c observed at adjacent locations. The optimal weight values are determined by solving the system (12) of $n+m$ linear equations constructed from the known correlation functions. The MSE provides with a measure of the accuracy of the porosity estimates. The term $-\mathbf{S}^t\ \mathbf{W}^*$ in (13) represents the reduction of error attainable by observing the data vector $\mathbf{Y}$ correlated with $P_c(\vec{x})$. As the mean square error reduction does not depend on the actual observations, the improvement in the estimation that an additional well may provide can be assessed prior to drilling. The MSE depends on the data configuration and on the degree of spatial correlation. For a purely random porosity field uncorrelated with transit time, the knowledge of p or t at one location does not provide with any information about p at another position. In that case, the best estimate of the porosity $p(\vec{x})$ is the mean m_p and the MSE is equal to the a priori variance σ_p^2.

As a simple illustrative example, consider the estimation of p at $\vec{x}$ from a single interval transit time t recorded a distance r away. The LMS porosity estimate is then given by:

$$p^*(\vec{x}) = m_p + \frac{C_{pt}(r)}{\sigma_t^2}\left(t(\vec{x}+\vec{r}) - m_t\right) \tag{14}$$

and the associated MSE is:

$$E\,\epsilon^2 = \sigma_p^2\left(1 - \frac{C_{pt}^2(r)}{\sigma_p^2\sigma_t^2}\right) \tag{15}$$

The weight value is proportional to the cross-correlation function evaluated at r. For an even and monotonically decaying function $C_{pt}(r)$, the maximum error reduction attainable depends on the square of the correlation coefficient $C_{pt}(0)/(\sigma_p\,\sigma_t)$. With increasing r, the MSE increases and becomes equal to the a priori variance σ_p^2 when r reaches the correlation length ξ. The increase in

MSE is accompanied by a reduction of the weight value which becomes zero for $r = \xi$. The equations (14) and (15) show that the correlation coefficient $C_{pt}(r)/(\sigma_p \sigma_t)$ measures the degree of linear dependence between $P(\vec{x})$ and $T(\vec{x}+\vec{r})$. If a linear functional relationship exists between $P(\vec{x})$ and $T(\vec{x})$, the coefficient of correlation is equal to ± 1 and the MSE vanishes. This simple example also shows that only neighbouring observations must be used in the estimator. In general, it is easy to see from (13) that for correlation functions with finite correlation length, data separated by a distance $r \geq \xi$ from the location of the estimation do not lead to a reduction of MSE. Another interesting property of the LMS estimator is that it is an exact interpolator: the porosity sample values are restored at the well locations with a zero MSE (See for example Journel and Huijbregts, 1978).

The reader familiar with time series analysis will recognize that the technique reviewed here is analogous to Wiener-Kolmogorov prediction theory. However the technique developed by Matheron (1965) and called cokriging in the geostatistics literature is more general. As it deals with irregularly distributed sample points, the filter weights are space-varying and must be adjusted to the data configuration at each location $\vec{x}$.

The calculation of the optimal weight vector $\mathbf{W}^*(\vec{x})$ requires an estimate of the data correlation matrix $\mathbf{C}(\vec{x})$ and of the correlation vector $\mathbf{S}(\vec{x})$. The elements of $\mathbf{C}$ are given by the correlations between all pairs of r.v. in the data vector $\mathbf{Y}$. These correlations depend only on the interdistances between the sample points. The vector $\mathbf{S}$ is formed by the correlation between $P_c(x)$ and the components of $\mathbf{Y}$. These last correlations depend on the distances from the data points to the position $\vec{x}$ where porosity is estimated. To estimate the elements of $\mathbf{C}$, we can not simply use sample correlations calculated as explained in the previous

section. With such estimates, **C** may not be positive definite. Furthermore, there may be distances for which too few or no pairs of sample points are available. In addition, as the data are usually irregularly spaced, the correlation matrix does not have a Toeplitz structure and we can not take advantage of Levinson recursion scheme [Makhoul, 1975; Ulrych and Bishop, 1975] to calculate a positive definite estimate of the data correlation matrix. The standard approach that we adopt here consists in fitting appropriate (see the appendix) continuous functions to the sample auto- and cross-correlation values. These functions are then evaluated for all distances appearing in the matrix **C** (or in the vector **S**). In the correlation model considered here, the functions C_{pp} , C_{tt} and C_{pt} are proportional to the same basis function $C(r)$ given in the appendix (eq. (a-7)). In general, the three correlation functions may be expressed as linear superposition of several basis functions whose weight must be choosen carefully so as to guarantee that the data correlation matrix is positive definite [Journel and Huijbregts, 1978]. Finally, in addition to the mean square estimation error predicted from the correlation model, there will be an error resulting from the difference between the fitted model and the true correlation structure.

4. Porosity Mapping in the Simulated Reservoir

The LMS estimation technique reviewed in the previous section is now used to map the lateral variations of porosity in the simulated reservoir model. The simulated map (figure 1) represents the perfectly known areal porosity distribution against which the estimates can be compared. The porosity spatial distribution is predicted first by interpolating between the porosity observations at the drilling sites then by using a single linear relationship between $p(\vec{x})$ and the interval transit time $t(\vec{x})$ at the same location and finally by constructing seismically derived porosity estimates which account for the actual correlation

structure. In addition, the quality of the reconstructed porosity surfaces is analysed and the influence of the prediction accuracy on future development of the reservoir is assessed.

Well derived mapping

The porosity surface shown in figure 1 is first reconstructed from the sample porosity values alone. Figure 2 shows that there are only 41 drilling sites in the reservoir field. A LMS porosity estimator of the form given in (7) but with $m = 0$ is evaluated at each node of the 50x50 simulated grid. At a grid point $\vec{x}$, the estimate is a weighted average of porosity observations made at distances from $\vec{x}$ smaller than ξ. Figure 8 shows the resulting reconstructed surface $p^*(x, y)$. In zones where well control is available, the LMS technique produces a smooth image of the actual porosity variations. As expected from the spatial configuration of the drilling sites, the well-derived map fails to detect the porous zone in the north-eastern corner of the reservoir. It also leaves undetected the low porosity cluster in the southern part of the field.

The MSE map (figure 9) calculated from (13) provides with a measure of the relative confidence that can be attached to the p estimates in different zones of the reservoir. This map reflects the spatial configuration of the data and the correlation length of the porosity field. At the drilling sites, the estimates coincide with the sample values and the MSE is zero. Away from the wells, the expected error level increases. When the distance to the closest well approaches ξ, the MSE converges to the a priori variance $\sigma_p^2 = 6\%^2$ and the porosity estimates approach the mean $m_p = 20\%$. In practice, the mapping from well data alone must be limited to distances from the wells which are small compared to the correlation length.

Conventional seismically based mapping

Conventional approaches to porosity mapping from seismic data are based on semi-empirical formula (like Wyllie's time-average equation) calibrated from the well data. One such technique consists in cross-plotting the core or log-derived porosities against the transit times which are derived from seismic traces recorded in the vicinity of wells. A single empirical relationship fitted to the correlation cloud is then used across the reservoir to predict $p(\vec{x})$ from the transit time $t(\vec{x})$ at the same location.

A linear least-squares fit to the correlation diagram $t(\vec{x})$–$p(\vec{x})$ is shown in figure 4. This regression line was used to calculate the porosity map shown in figure 10 from the surface $t(x,y)$ (figure 3). In area where well control is sparse or missing, the seismically derived map tend to be closer to the actual porosity surface (figure 1) than the map based on the well observations alone (figure 8). In particular, the porous zone in the upper corner of the field is detected. However, this map exhibits many spurious details and fails to reproduce the central high p zone clearly delineated by interpolating between the well data. In fact, the topography of this naive reconstruction of $p(x,y)$ is simply a scaled version of the transit time surface (figure 3). Consequently, the reproduction of the sample porosity values at the drilling locations is not even guaranteed.

This standard regression analysis does not take into consideration the spatial configuration and interdependence between the observations. By using the least-squares fit shown in figure 4, the implicit assumption is made that $\xi = 0$ and that the correlation functions are delta functions, i.e., $C_{pp}(r)/\sigma_p^2 = C_{tt}(r)/\sigma_t^2 = C_{pt}(r)/C_{pt}(0) = \delta(r)$. Under this unrealistic assumption, the best porosity linear estimator whose general form is (7) reduces to (14) with $r = 0$. This last equation is precisely the linear relationship displayed

in figure 4. The use of this regression equation amounts to ignoring completely the lateral continuity in the variations of the reservoir properties. With this estimator, the proximity of a drilling site does not reduce the error. The MSE. $E(\epsilon^2) = 3\%^2$, calculated from (15) is uniform in the reservoir field and simply measures the dispersion about the regression line of the points (t, p) in figure 4.

LMS seismically based mapping

We will now show that a more accurate reconstruction of the surface $p(x, y)$ is obtained by considering linear mean square estimates which account for the spatial continuity in the variations of p and t.

At each grid node $\vec{x}$, the porosity estimator is now a weighted sum of adjacent sample porosity points and of the transit time measurements made at the 9 closest grid points within a distance $\sqrt{2}\,\Delta$ from $\vec{x}$. The weights are calculated by solving the system of equations (12) which depends solely on the known data configuration and correlation functions. The resulting reconstruction of the simulated surface (figure 1) is shown in figure 11. The topography of the predicted surface now matches the main features of the actual spatial variations of p over the entire reservoir. Compared with the reconstruction from the sample porosities alone, the seismically controlled mapping is greatly improved in the southern region and along the borders of the field where the well coverage is sparse or inexistent. The improved resolution provided by the seismically assisted mapping may help planning the location of additional drilling sites.

The predicted MSE map (figure 12) still takes its zeros at the drilling sites. But as a result of the dense sampling of the surface $t(x, y)$ cross-correlated with $p(x, y)$, the predicted error level is overall about twice as low as for the well-derived map. A comparison between figures 10 and 11 shows that the LMS

technique outperforms the conventional least-squares fitting approach. It is important to realize that the two mapping methods use the same data. The dramatic improvement provided by the LMS estimation stems from the fact that it accounts for the structure in the joint variability of p and t by means of the spatial correlation functions.

Compared performances of the estimation methods

One interesting way to compare the quality of the three reconstructed porosity surfaces is to consider the scatter-diagram of true (simulated) versus predicted porosities for each estimation method. To each point $\vec{x}$ in the reservoir correponds a point of coordinates $(p^*(\vec{x}), p(\vec{x}))$ in each of figures 13, 14 and 15. The cloud of points represents the bivariate histogram of $P^*(\vec{x})$ and $P(\vec{x})$. For an ideal estimator, the bivariate distribution coincides with the diagonal $p - p^* = 0$. In pratice, except at the drilling locations, there is a non zero prediction error, $p(\vec{x}) - p^*(\vec{x}) = \epsilon(\vec{x})$. For a good estimator, we require that the correlation cloud be concentrated about the diagonal. As a measure of the dispersion of the estimates p^* about the true values p, we show in table 2 the experimental mean square error, $<\epsilon^2(\vec{x})>_{\vec{x}}$, for each reconstructed surface (figures 8, 10, and 11). This table shows that by accounting for spatial correlations, the error level has been dramatically reduced: the experimental MSE in the conventional reconstruction from seismic data is more than three times larger than in the LMS seismically derived map. As a result of the poor assumption of pure spatial randomness, the conventional seismically controlled map even exhibits a larger experimental MSE than the map constructed from the well data alone. Table 2 also shows that the LMS method based on the densely sampled t surface leads to an experimental MSE twice as small as in the well-derived map.

One important feature of the reconstructed surfaces is how well they reproduce

the extrema in the porosity field. On the one hand, the low porosity zones may act as barriers to the flow of fluid and their detection is important for the planning of the oil recovery operations. On the other hand, the very porous regions may constitute the prime targets for additional development wells in the reservoir. The detection of high or low porosity clusters in the reservoir depends on the amount of smoothing involved in the estimation procedure. The smoothing is itself related to the MSE level in the estimates. The solid line in figure 16 represents the fractional reservoir area where the porosity is above the value p specified in abscissa. The symbols o and + represent respectively the predicted area for the uncorrelated and correlated LMS reconstruction from the seismic data. The large smoothing resulting from the conventional estimation method is clearly apparent. Most area where $p > 22\%$ are left undetected by the conventional least-squares fit method. Based on this method, the predicted pore volume associated with the most porous zones would be dramatically underestimated.

In the development phase of the reservoir, the positions of new drilling sites may be selected in zones where the predicted porosity is high, e.g., $p^* > p_0$. We have just seen that with the conventional mapping technique, most of those zones may not be detected if the cut-off p_0 is high. However in the selected zones, it is important that the porosity estimates are not systematically lower or higher than the actual values. Mathematically, we require that $\phi(p^*) = E(P \mid p^*)$ be equal to p^*. This amounts to requiring that the center of mass of the points distributed along a vertical chord at $p = p^*$ coincides with the diagonal in the correlation diagrams p^* versus p. Figures 13 to 15 show that for the three reconstructed surfaces the experimental regression curve $\phi(p^*)$ is not substantially different from the diagonal. The unbiasedness of the conditional mean $E(P \mid p^*)$ has an important implication on the prediction of the reserves

in place. It means that the actual pore volume in selected zones where the estimated porosity is above p_0 can be estimated without bias by the predicted pore volume based on the estimates in the selected areas [Journel and Hujbregts, 1978].

5. Porosity Mapping in the Taber-Turin reservoir

The three estimation schemes are now applied to the areal mapping of the porosity in an oil-bearing reservoir in the Taber-Turin area of Alberta. A stratigraphic description of this reservoir has been given by De Buyl et al. [1986]. Core and well-log derived porosities were measured at eight producing wells in the northen part of the field and at two dry wells in its southern portion (figure 17). The high porosity producing area corresponds to a 15 to 30 m thick channel-sand trending approximately NW-SE. This porous sand is truncated to the south by a low porosity silt-filled channel.

A 3-di seismic survey covering an area of about 2x2 km^2 was acquired on the reservoir field. Figure 18 shows the spatial distribution of the inverse of the acoustic impedance averaged across the reservoir thickness. The impedances were extracted from the true amplitude seismic data using the seismic lithologic modelling method of Gelfand and Larner [1984]. They were then smoothed and gridded at a 50 m interval which is about 2.5 times the areal coverage provided by the seismic survey. In zones where the sand pinches out, the data processing sequence involved the unraveling of the reflections coming from the top and base of the reservoir interval [De Buyl, et al., 1986].

The circles in figure 19 represent the normalized sample auto-correlation function C_{tt} calculated from the inverse impedance map. To simplify the notation, the inverse of the acoustic impedance is also denoted by t. The solid line

corresponds to the fitted gaussian correlation model $C_{tt}(r)/\sigma_p^2 = \gamma(r) = \exp[-(r/\xi)^2]$ where $\sqrt{3}\xi \approx 1000m$ can be considered as the practical range of spatial correlation. The parabolic behaviour of C_{tt} near $r = 0$ is indicative of the smoothing which was applied to the impedance surface.

The low acoustic impedance zone trending E-W in the northen part of the seismic survey (figure 18) correlates spatially with the positions of the wells in the porous channel-sand (figure 17). The crosses in figure 19 correspond to the experimental cross-correlation function C_{pt}. A large coefficient of correlation of about 0.9 is observed. Although the fluctuations of the sample cross-correlations are more pronounced than for C_{tt}, a gaussian correlation structure is clearly visible with approximately the same correlation length $\sqrt{3}\xi \approx 1km$.

The drilling sites (figure 17) are too sparse to permit the construction of a reliable sample porosity auto-correlation function $C_{pp}(r)$. Still, the statistical structure of the porosity spatial variations must be modelled. It was shown that the conventional least-squares fit technique assumes implicitly that the porosity correlation length is zero. A more realistic model of spatial variability can be constructed indirectly from the seismic information. Figure 19 shows that $C_{tt}(r)$ and $C_{pt}(r)$ are approximately proportional to the same basis correlation function $\gamma(r) = \exp[-(r/\xi)^2]$. We then assume that the function $C_{pp}(r)$ which can not be inferred directly from the well data, is also proportional to $\gamma(r)$. This correlation model which is called intrinsic in the geostatistical literature [Matheron, 1965], is justified if the variations of the acoustic impedances in the reservoir interval are controlled in large part by changes of porosity. If, in addition to porosity, t is strongly affected by the variations of another petrophysical parameter with a different correlation structure, C_{tt} will appear as a superposition of two components which must be separated in order to estimate C_{pp}. In general, when

direct evaluation of the spatial correlation functions is impossible, indirect geological information must be used to model the structure of spatial variablity. The usual assumption of spatial randomness is rarely if ever appropriate in a reservoir environment.

One way of showing that the inrinsic correlation model,i.e., $C_{pp}(r)/\sigma_p^2 = C_{tt}(r)/\sigma_t^2 = C_{pt}(r)/C_{pt}(0) = \gamma(r)$, is more appropriate than the hypothesis of pure spatial randomness ($C_{pp}(r)/\sigma_p^2 = \delta(r)$) is to cross-validate the two models at the well locations. Each porosity sample point (figure 17) is deleted in turn and its value is estimated from the remaining porosity data and from the impedance measurements. Figure 20 compares the prediction errors in the cross-validation of the two correlation models. The estimates denoted by the symbol r were obtained under the assumption of uncorrelated porosity variations from the linear regression equation (14) between $p(\vec{x})$ and $t(\vec{x})$ at the well locations. The predictions denoted by the symbol l are based on the gaussian intrinsic correlation model (figure 19). In this case, the porosity estimate at each well location $\vec{x}$ is a weigted average of $t(\vec{x})$ and of the porosity sample points within a distance ξ=1km from $\vec{x}$. Based on this model, the mean square prediction error is twice smaller than that resulting from the conventional regression method. The improvement provided by the correlated model is naturally limited to the northen part of the field were the drilling sites are clustered in a high porosity zone. No significant reduction in the error level is to be expected at the two isolated low porosity sample points separated from the others by distances of the order of ξ. The validity of the intrinsic hyphothesis was also evaluated by predicting p at each well from the porosity at the other wells using the model $C_{pp}(r)\alpha\gamma(r)$. The prediction errors were then assessed and their squares were compared to the mean square error expected from the correlation model. Except at the two isolated drilling sites in the south of the

reservoir, the errors were within the range predicted from the gaussian correlation model. In this last cross-validation, the average square experimental error, $<\epsilon^2>_{\bar{z}}$ is 10 $\%^2$ when the two isolated wells are considered but only 1.3 $\%^2$ when the average is taken only over the 8 wells located in the high porosity zone. This last error is smaller than that resulting from the simple $p-t$ regression model.

Finally, the lateral variations of p in the reservoir interval are predicted from the three different estimation schemes discussed in the previous section (figure 21). The well derived map (LMS [P]) based on the gaussian porosity autocorrelation $C_{pp}(r)/\sigma_p^2=\gamma(r)$ exhibits a dome aligned in the E-W direction which correlates well with the high acoustic impedance zone (figure 18). The bowl-shaped depression in the porosity surface, centered approximately at an isolated well location, mimics the behaviour of the gaussian function $\gamma(r)$. This feature of the LMS method is easily understood by relacing t by p in equation (14). Figure 21 also shows the the seismically assisted reconstructions of $p(x,y)$ based on the linear regression $p(\vec{x})-t(x)$ and on the intrinsic correlation model. The well derived map and the seismically derived map based on the intrinsic model both clearly show two domes connected by a saddle-shaped structure. This feature is not captured by the conventional seismically based method which, in addition, fails to honor the sample porosity values. Overall, except in the southern region of the field, the amount of details provided by the two seismically derived surfaces is not much larger than the well based mapping. This follows from the fact that there is little structure in the impedance map (figure 18) which is not already underlined by the well data (figure 21, LMS [P]). However, from the cross-validation study summarized above, we expect that the the pore volume estimated from the impedance derived LMS map will be much more accurate than the estimate based on the well derived map or on the regression reconstruction.

Conclusion

A statistical technique integrating the well measurements and the seismic information has been studied for porosity mapping in oil-bearing reservoirs. The most important feature of the estimation method is that it takes into account the structure of joint lateral variability of porosity and transit time in the reservoir interval. Taking advantage of this information condensed in the spatial correlation functions, accurate and risk-qualified linear mean square estimates of porosity are derived across the reservoir, even in zones where well control is sparse or absent.

The new seismically assisted mapping technique was tested on a numerically simulated reservoir model and compared first with the mapping derived from well data alone then with a conventional least-squares fitting procedure based on the correlation diagram porosity-transit time. The new method detects subtle porosity lateral variations that can not be mapped from the well data alone. In addition, the seismically derived porosity estimates based on the correlation functions provide with a far more accurate and detailed reconstruction of the porosity areal distribution than the standard uncorrelated least-squares approach. Furthermore, the delineation of porous zones and the estimation of their pore volume is greatly improved with the technique based on spatial correlations.

The correlation-based estimation method was also applied to the mapping of porosity in an oil-bearing sand reservoir from acoustic impedance measurements extracted from a 3-di seismic survey. The cross-validation study at the drilling sites shows that a significant error reduction is expected in the calculation of the oil reserves based on the proposed intrinsic correlation model. The gain in prediction accuracy stems from the fact that the LMS estimation procedure takes into consideration the lateral continuity in the changes of rock properties.

Appendix

We briefly underline the simulation technique used to generate the spatial distribution of porosity and transit time depicted in figures 1 and 3. A detailed account of the method is given by Luster (1986). The satistical properties which are reproduced in the simulation are the means, m_p and m_t, and the spatial auto- and cross-correlation functions of the r.f. $\{ P(\vec{x}), T(\vec{x}) \}$.

We assume that the principal cause of variability of the transit time in the reservoir interval is the change in porosity. Accordingly, all the correlation functions are taken proportional to the same function $C(r)$, i.e., $C_{pp}(r)/\sigma_p^2 = C_{tt}(r)/\sigma_t^2 = C_{pt}(r)/C_{pt}(0) = C(r)$. The normalized isotropic correlation function $C(r)$ is depicted as the solid line in figure 5. In order to obtain a realization of the bivariate r.f. $\{P, T\}$ with the specified correlation structure, we combine linearly the realizations of two independent r.f. $\{Z_1(\vec{x})\}$ and $\{Z_2(\vec{x})\}$ with auto-correlation function $C(r)$, unit variance, i.e., $C(0)=1$ and zero mean. $P(\vec{x})$ and $T(\vec{x})$ are given respectively by :

$$P(\vec{x}) = \alpha_1 Z_1(\vec{x}) + \alpha_2 Z_2(\vec{x}) + m_p \qquad \text{(a-1)}$$

$$T(\vec{x}) = \beta_1 Z_1(\vec{x}) + m_t \qquad \text{(a-2)}$$

As the variables Z_1 and Z_2 are independent, the centered correlation functions of $\{P, T\}$ are given by:

$$\begin{aligned} C_{pp}(r) &= \sigma_p^2 C(r) = (\alpha_1^2 + \alpha_2^2) C(r) \\ C_{tt}(r) &= \sigma_t^2 C(r) = \beta_1^2 C(r) \\ C_{pt}(r) &= C_{pt}(0) C(r) = \alpha_1 \beta_1 C(r) \end{aligned} \qquad \text{(a-3)}$$

With the selected values of σ_p^2, σ_t^2 and $C_{pt}(0)$ given in table 1, the above equations can be solved uniquely for the three constants α_1, α_2 and β_1. The Schwarz's inequality, $C_{pt}(0) < \sigma_p \sigma_t$ must be verified to guarantee that any linear combination of the r.v. P and T has a variance larger than zero.

The last problem to tackle is the simulation of the two r.f $\{Z_1\}$ and $\{Z_2\}$ with mean $m_z = 0$ and auto-correlation $C(r)$. Each simulation is performed by convolving a two-dimensional white noise process with a weighting function whose auto-correlation is equal to the desired $C(r)$. We consider a purely random field $\{U(\vec{x})\}$ with mean $m_u = 0$ and auto-corellation function $E\ U(\vec{x}+\vec{r})U(\vec{x}) = \delta(r)$. The convolution of this field with the weighting function $h(x,y) = h(r=(x^2+y^2)^{1/2})$ gives rise to the r.f $\{Z\}$:

$$Z(\vec{x}) = \int h(\vec{x}-\vec{u})\ U(\vec{u})d\vec{u} \tag{a-4}$$

As $m_u = 0$, the mean of Z is also zero. Using the fact that $C_{zz}(r) = \delta(r)$, the auto-correlation function of the field $\{Z\}$ is given by:

$$C(r) = E\ Z(\vec{x}+\vec{r})Z(\vec{x}) = \int h(\vec{x}+\vec{u})\ h(\vec{u})d\vec{u} \tag{a-5}$$

which is by definition the spatial auto-correlation of h. The weighting function considered here is defined by:

$$h(r) = \begin{cases} \dfrac{1}{\pi^{1/2}\xi/2} & \text{if } r \leq \xi/2 \\ 0 & \text{if } r > \xi/2 \end{cases} \tag{a-6}$$

and the function C evaluated at r is simply proportional to the area of overlap between two circles of diameter ξ with centers separated by a distance r. When $r = 0$, the two circles overlap completely and from (a-5) and (a-6), we see that $C(0) = \sigma_z^2 = 1$ as required. When the distance r exceeds ξ, the area of intersection between the two circles is null and the variables $Z(\vec{x})$ and $Z(\vec{x}+\vec{r})$ become uncorrelated. ξ is simply the correlation length of the r.f $\{Z\}$. For distances r between 0 and ξ, $C(r)$ is given by:

$$C(r) = 1 - \frac{2}{\pi}\left(\frac{r}{\xi}\left(1 - \left(\frac{r}{\xi}\right)^2\right) + arsin\frac{r}{\xi}\right) \tag{a-7}$$

In summary, the simulation of $\{P, T\}$ goes as follows. Two independent fields of random numbers $\{U_1\}$ and $\{U_2\}$ with zero mean and unit variance are

generated at the nodes of the 50x50 two-dimensional grid. At each node $\vec{x}$, $Z_1(\vec{x})$ and $Z_2(\vec{x})$ are obtained by summing respectively the random numbers u_1 and u_2 located within a distance $\xi/2$ from $\vec{x}$. The areal distributions of p and t characterized by the normalized correlation function (a-7) are finally obtained by forming the linear combinations (a-1) and (a-2) of the realizations of $\{Z_1\}$ and $\{Z_2\}$.

References

Agterberg, F.P., Autocorrelation functions in geology, in *Geostatistics,* 113-141, D.F. Merriam, Ed., Plenum, New York, 1970.

Angeleri, G.P., and R. Carpi, Porosity prediction from seismic data, *Geophysical Prospecting, 30,* 580-607, 1982.

De Buyl, M., T. Guidish, and F. Bell, Reservoir description from seismic lithologic parameter estimation, *SPE 15505,* 1-7, 1986.

Gelfand, V., and K. Larner, Seismic lithologic modeling, *The Leading Edge, 3,* 30-35, 1984.

Journel, A.G., and C.J. Huijbregts, *Mining Geostatistics,* p. 600, Academic. London, 1978.

Luster, G., Raw materials for Portland cement: applications of conditional simulation of coregionalization, p. 531, Ph.D. Thesis, Stanford University. Stanford, California, 1985.

Makhoul, J., Linear prediction: a tutorial review, *IEEE Proc., 63,* 561-580.

Matheron, G., *Les Variables Régionalisées et leur Estimation,* p. 305, Masson. Paris, 1965.

Maureau G.T.F.R., and D.H. Van Wijhe, The prediction of porosity in the Permian carbonate of eastern Netherlands using seismic data, *Geophysics, 44,* 1502-1517, 1979.

Ripley, B.D., *Spatial Statistics,* p. 252, Wiley, New York, 1981.

Ulrych, T.J., and T.N. Bishop, Maximum entropy spectral analysis and autoregressive decomposition, *Rev. Geophys. Space Phys., 13,* 183-199. 1975.

Vanmarcke, E., *Random Fields,* p. 382, MIT press, Cambridge, 1983.

Yaglom, A.M., *An Introduction to the Theory of Stationary Random Functions,* p. 235, Prentice-Hall, Englewood Cliffs, New Jersey, 1962.

Wyllie, M.R., A.R. Gregory, and G.H.F. Gardner, An experimental investigation of factors affecting elastic wave velocities in porous media, *Geophysics, 23.* 459-493, 1958.

Figure 1 : Simulated areal distribution of porosity (%) in a sandstone reservoir. The underlying square grid has 50x50 nodes. The spacing between nodes is 200 m.

Figure 2 : Posting of the porosity (%) measured at 41 fictitious drilling sites in the reservoir.

Figure 3 : Simulated areal distribution of the seismic transit time ($\mu sec/m$) in the reservoir interval. The underlying grid is the same as in figure 1.

Figure 4 : Cross-plot transit time against porosity. Each point in the diagram represents one position $\vec{x}$ in the reservoir and its coordinates are $(t(\vec{x}),p(\vec{x}))$. The solid line represents a linear least-squares fit to the correlation cloud.

Figure 5 : Spatial auto-correlation function of the porosity areal distribution. The solid line is the theoretical correlation function. The o 's are the sample correlations calculated from the surface $p(x,y)$. The +'s are the sample correlations calculated from the well data.

Figure 6 : Spatial auto-correlation function of the transit time areal distribution. The solid line is the theoretical correlation function. The o 's are the sample correlations calculated from the surface $t(x,y)$.

Figure 7 : Spatial cross-correlation function between porosity and transit time. The solid line is the theoretical correlation function. The o 's are the sample correlations calculated from the surfaces $p(x,y)$ and $t(x,y)$.

Table 1

Statistical properties
of
the simulated random fields

$\{P(x,y)\}$	$m_p = 20\ \%$ $\sigma_p^2 = 6\ \%^2$
$\{T(x,y)\}$	$m_t = 290\ \mu\text{sec}\,m^{-1}$ $\sigma_t^2 = 65\ (\mu\text{sec}\,m^{-1})^2$ $C_{pt}(0) = 14\ \%\mu\text{sec}\,m^{-1}$

Table 2

Experimental mean
of
the squared estimation error

$P^*(x,y)$	$<\epsilon^2(\vec{x})>_{\vec{x}}$ $(\%^2)$
well derived map	2.1
conventional mapping from seismic data	3.0
LMS mapping from seismic data	0.9

Table 1

Statistical properties
of
the simulated random fields

$\{P(x,y)\}$	$m_p = 20\ \%$ $\sigma_p^2 = 6\ \%^2$
$\{T(x,y)\}$	$m_t = 290\ \mu sec m^{-1}$ $\sigma_t^2 = 65\ (\mu sec m^{-1})^2$ $C_{pt}(0) = 14\ \% \mu sec m^{-1}$

Table 2

Experimental mean
of
the squared estimation error

$P^*(x,y)$	$<\epsilon^2(\vec{x})>_{\vec{x}}$ $(\%^2)$
well derived map	2.1
conventional mapping from seismic data	3.0
LMS mapping from seismic data	0.9

Figure 1 : Simulated areal distribution of porosity (%) in a sandstone reservoir. The underlying square grid has 50x50 nodes. The spacing between nodes is 200 m.

Figure 2 : Posting of the porosity (%) measured at 41 fictitious drilling sites in the reservoir.

Figure 3 : Simulated areal distribution of the seismic transit time ($\mu sec/m$) in the reservoir interval. The underlying grid is the same as in figure 1.

Figure 4 : Cross-plot transit time against porosity. Each point in the diagram represents one position $\vec{x}$ in the reservoir and its coordinates are $(t(\vec{x}),p(\vec{x}))$. The solid line represents a linear least-squares fit to the correlation cloud.

Figure 5 : Spatial auto-correlation function of the porosity areal distribution. The solid line is the theoretical correlation function. The o 's are the sample correlations calculated from the surface $p(x,y)$. The +'s are the sample correlations calculated from the well data.

Figure 6 : Spatial auto-correlation function of the transit time areal distribution. The solid line is the theoretical correlation function. The o 's are the sample correlations calculated from the surface $t(x,y)$.

Figure 7 : Spatial cross-correlation function between porosity and transit time. The solid line is the theoretical correlation function. The o 's are the sample correlations calculated from the surfaces $p(x,y)$ and $t(x,y)$.

Figure 8 : reconstructed porosity (%) areal distribution from the well data alone.

Figure 9 : Predicted mean square error ($\%^2$) for the estimation of porosity from the well data.

Figure 10 : Reconstruction of the surface $p(x, y)$ based on the regression line shown in figure 4.

Figure 11 : LMS reconstruction of the surface $p(x, y)$ based on the seismic and well data.

Figure 12 : Predicted mean square error ($\%^2$) for the LMS reconstruction shown in figure 11.

Figure 13 : Cross-plot $p^* - p$ for the well derived mapping. The curve is the experimental conditional expectation $E(P \mid p^*)$

Figure 14 : Cross-plot $p^* - p$ for the conventional mapping from the seismic data. The curve is the experimental conditional expectation $E(P \mid p^*)$.

Figure 15 : Cross-plot $p^* - p$ for the LMS mapping from the seismic and well data. The curve is the experimental conditional expectation $E(P \mid p^*)$.

Figure 16 : Fractional area of the reservoir where the porosity is above the value specified in abscissa. The solid line is the true area. The o's and the +'s correspond respectively to the area predicted by the conventional and LMS

mapping from the seismic data.

Figure 17 : 3-di seismic survey areal map with porosities (%) measured at the well locations. The distance between labelled thick marks is $200m$.

Figure 18 : Areal distribution of the inverse of the acoustic impedance in the reservoir interval. The distance between labelled thick marks is $200m$.

Figure 19 : Normalized sample auto- and cross-correlations. The solid lines are the fitted gaussian correlation functions.

Figure 20 : Cross-plot porosity estimate against true value in the cross-validation study.

Figure 21 : Estimated areal distribution of the porosity in the reservoir. (a) perspective views. (b) contours.

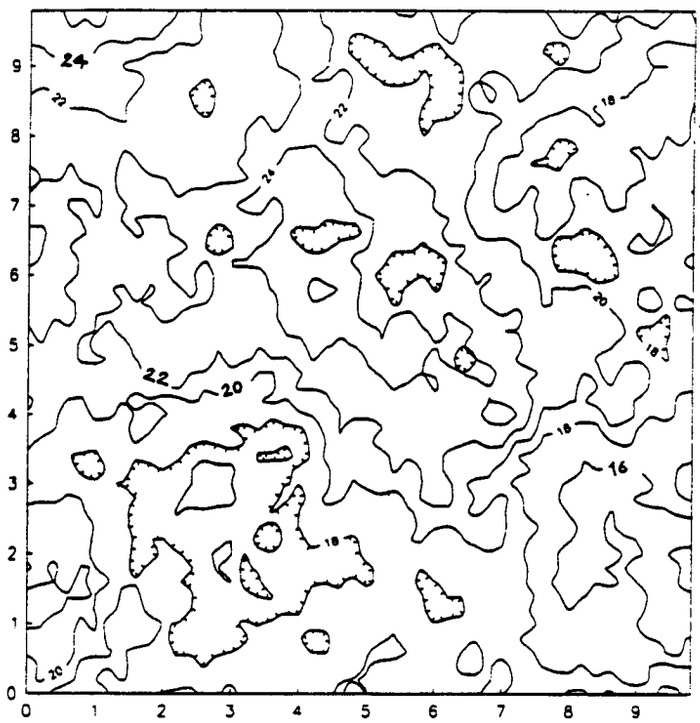

Figure 1 **Simulated porosity surface (%)**

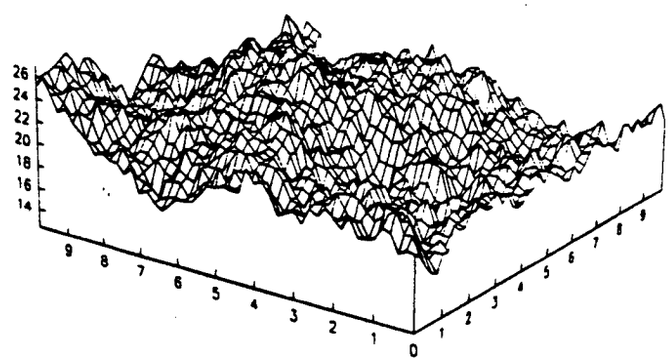

Figure 2

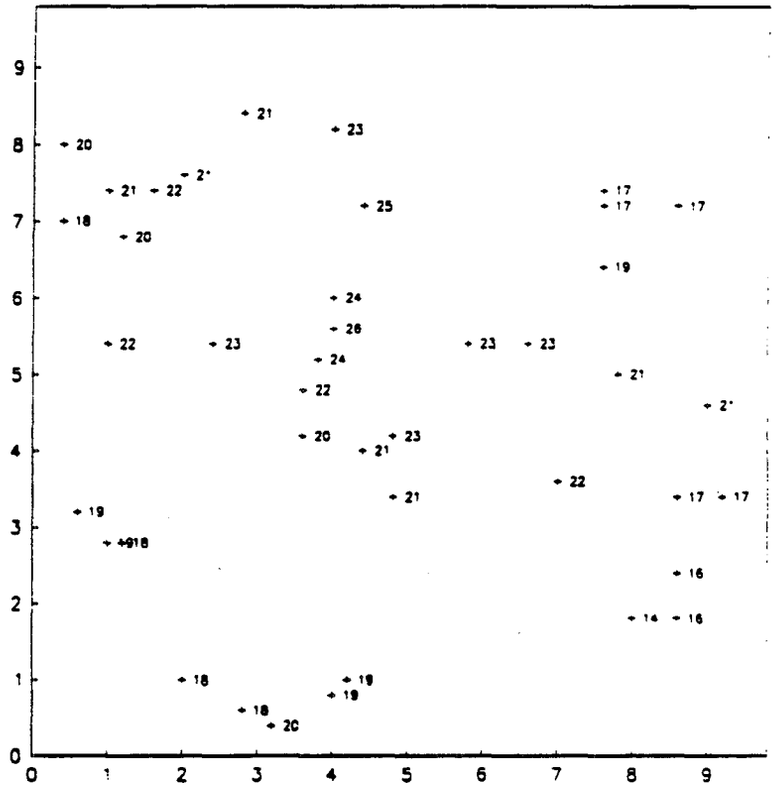
9
8
7
6
5
4
3
2
1
0
0 1 2 3 4 5 6 7 8 9
21 23 20 2* 21 22 25 18 20 17 17 17 19 24 26 22 23 24 23 23 22 21 2* 20 23 21 22 21 19 4918 17 17 16 14 16 18 19 19 18 20

Figure 3

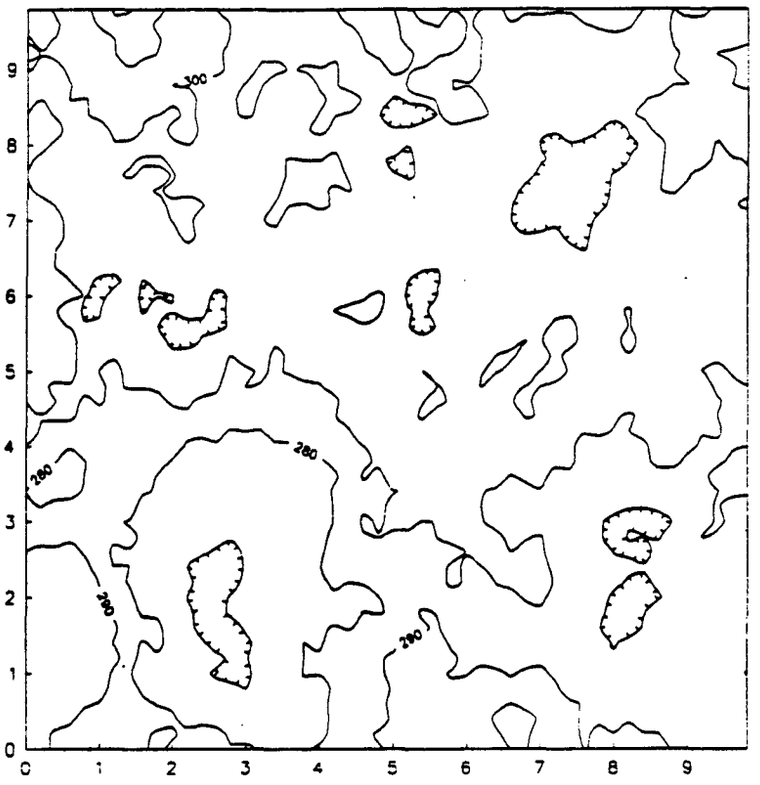

Figure 4

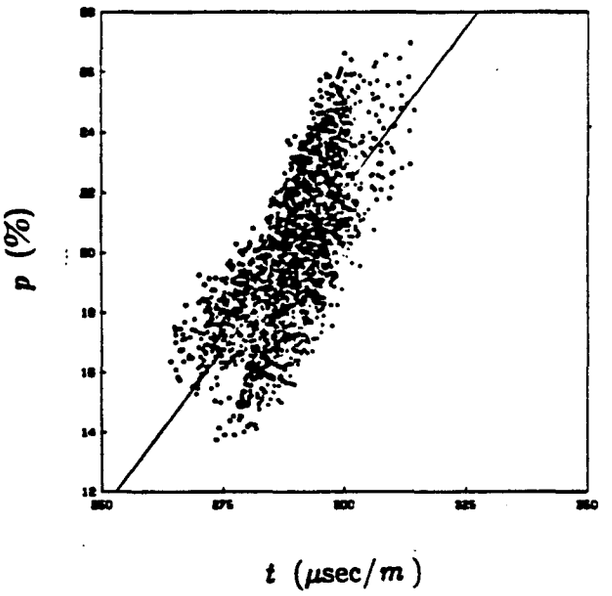

Figure 5

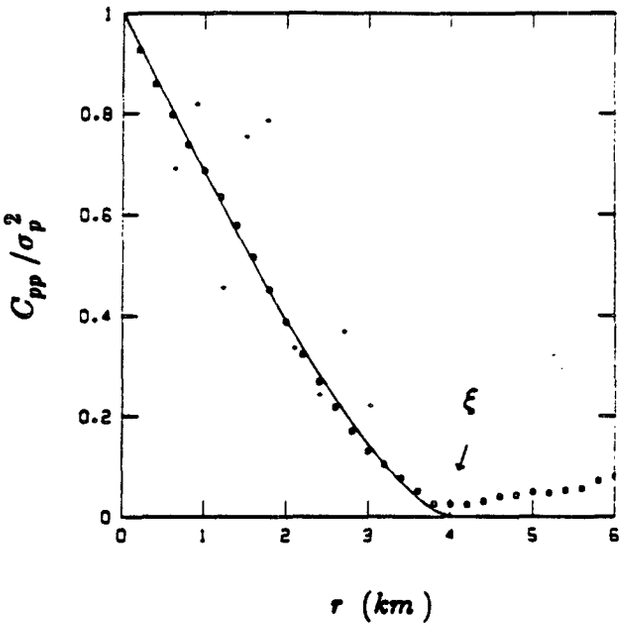

Figure 6

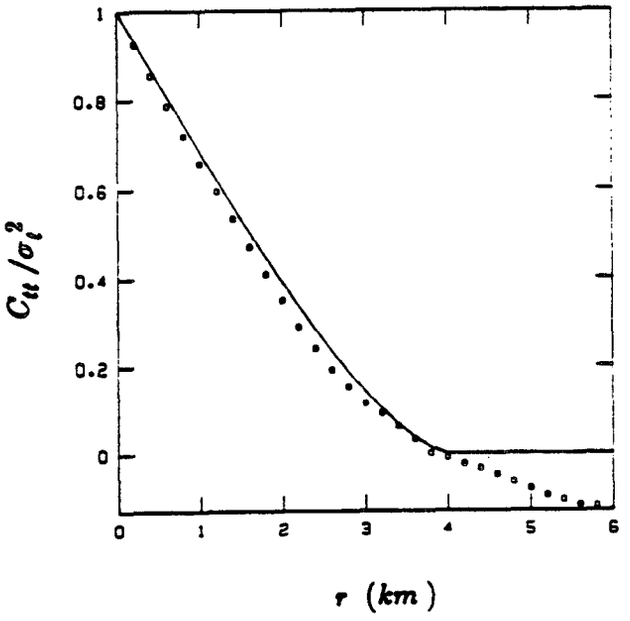

Figure 7

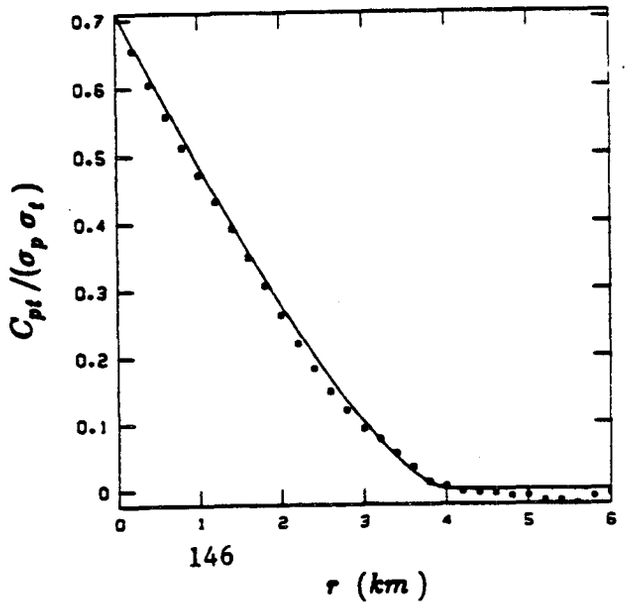

Figure 8

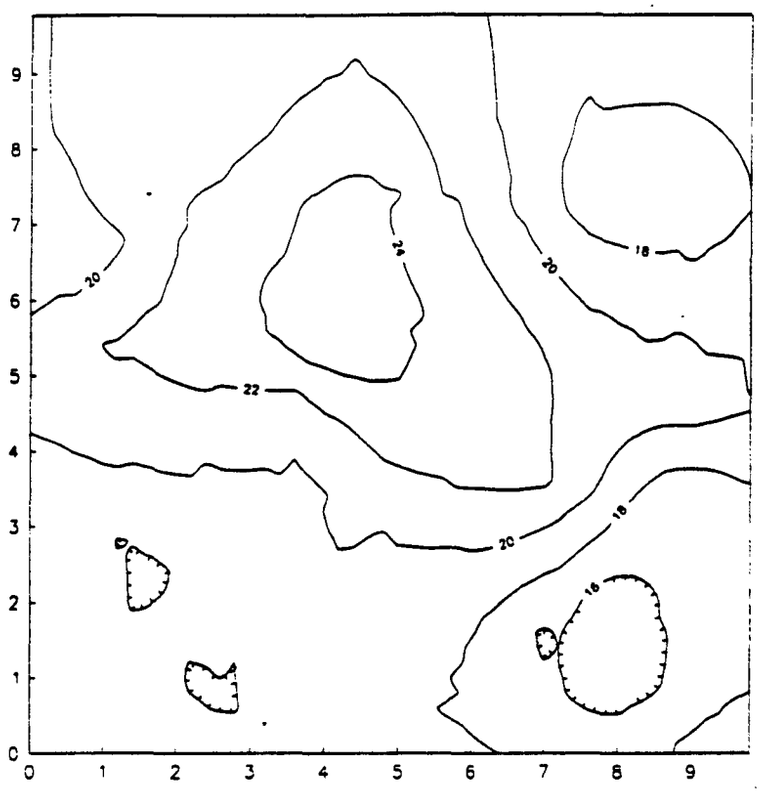

Figure 9

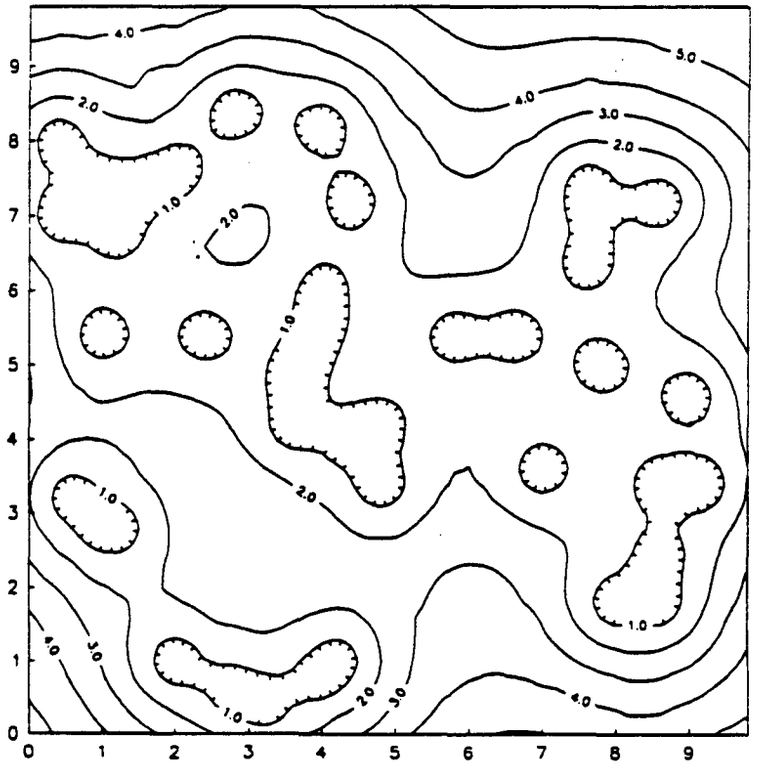

Figure 10

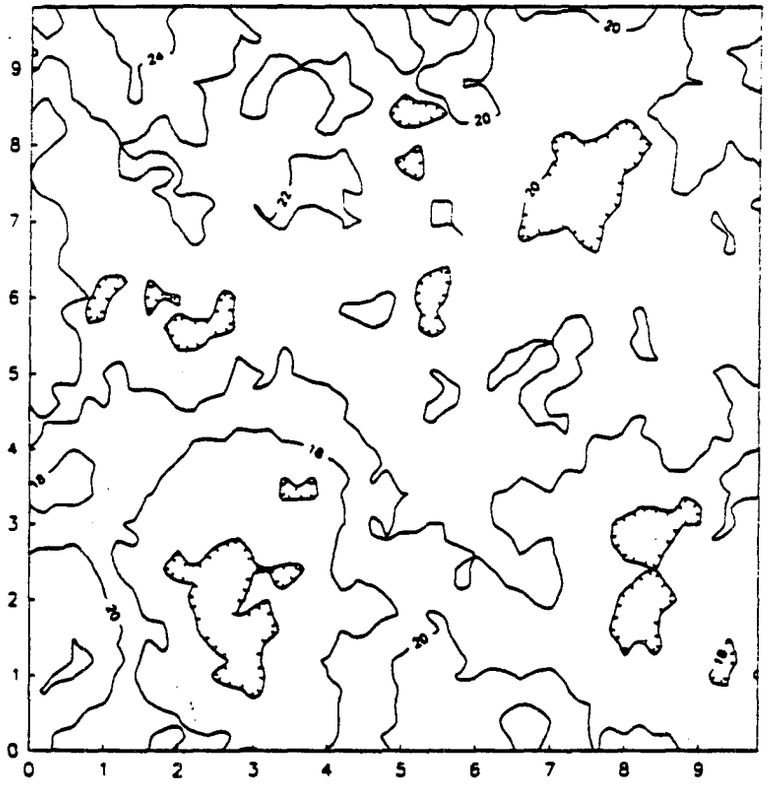

Figure 11

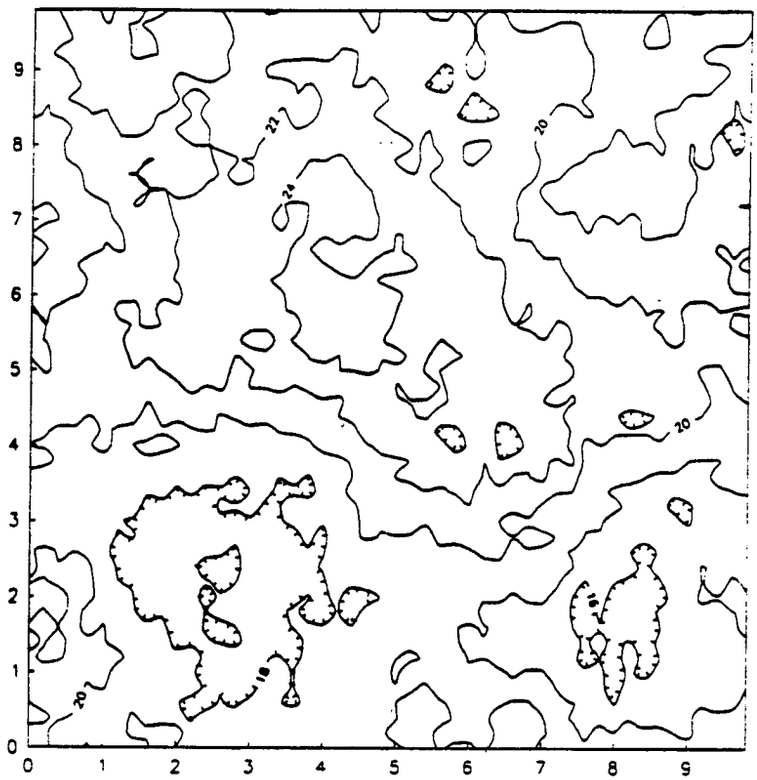

Figure 12

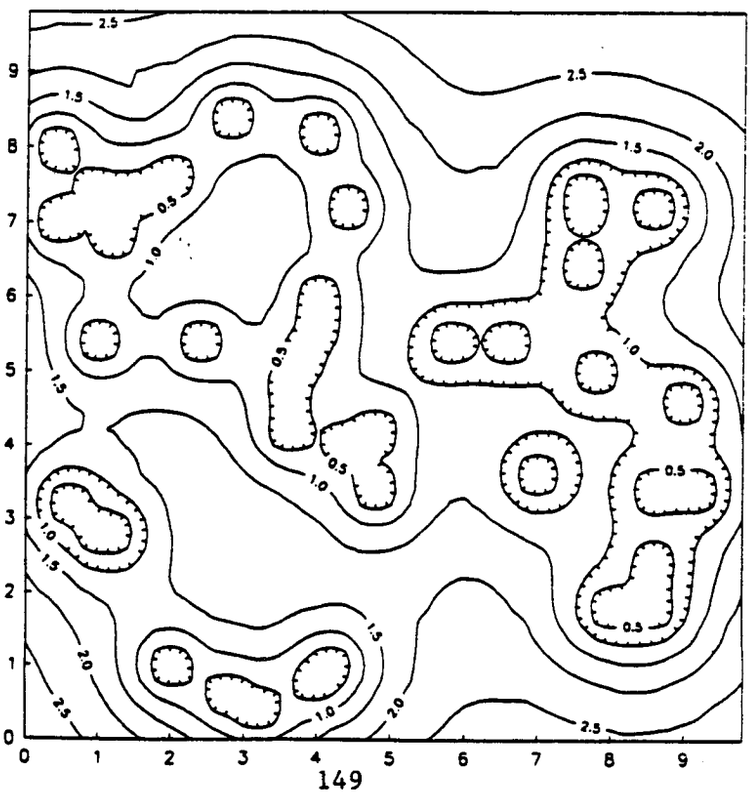

Figure 13

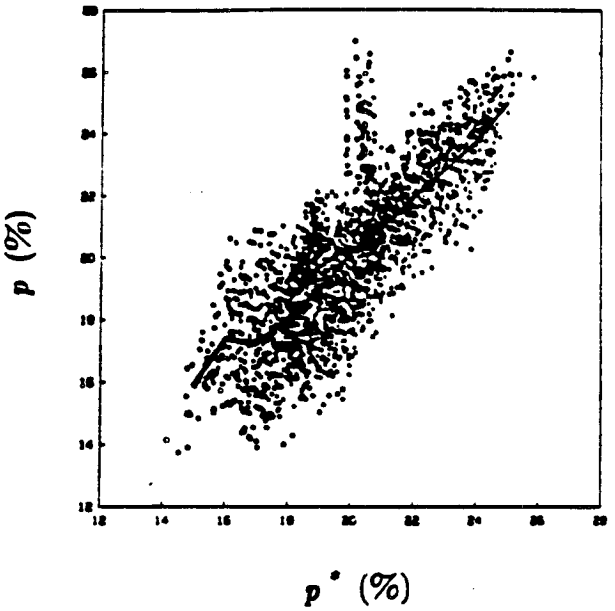

Figure 14

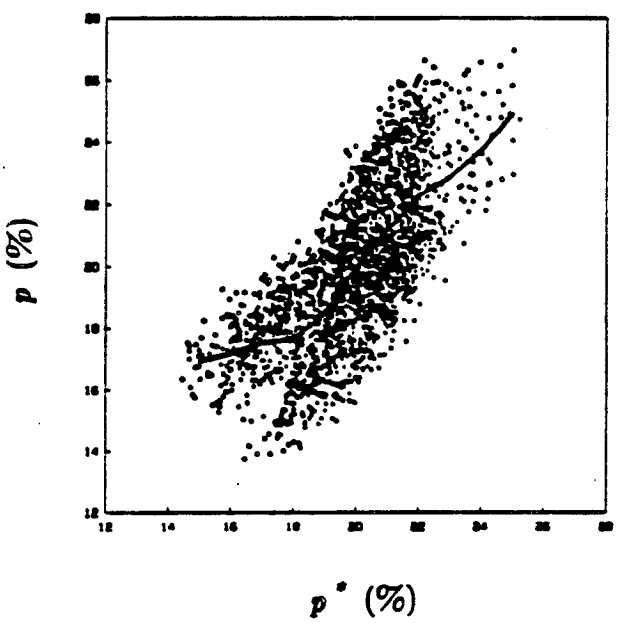

Figure 15

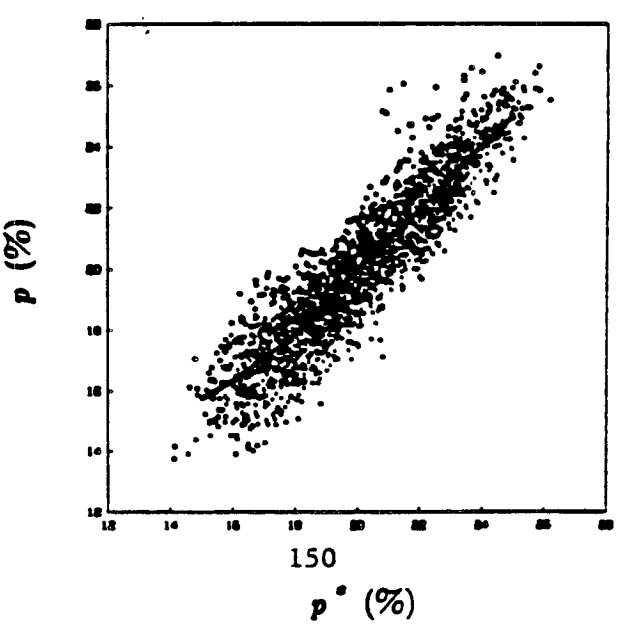

Figure 16

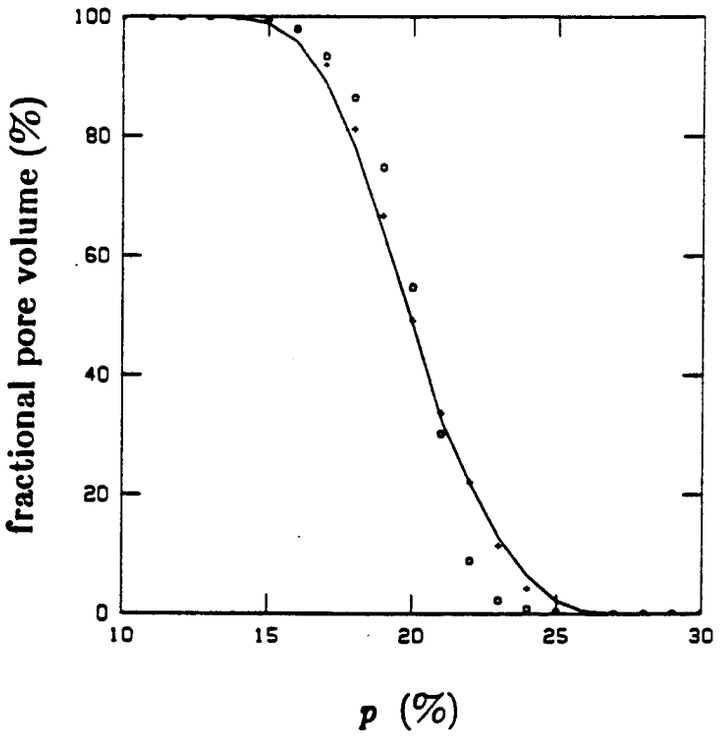

Figure 17

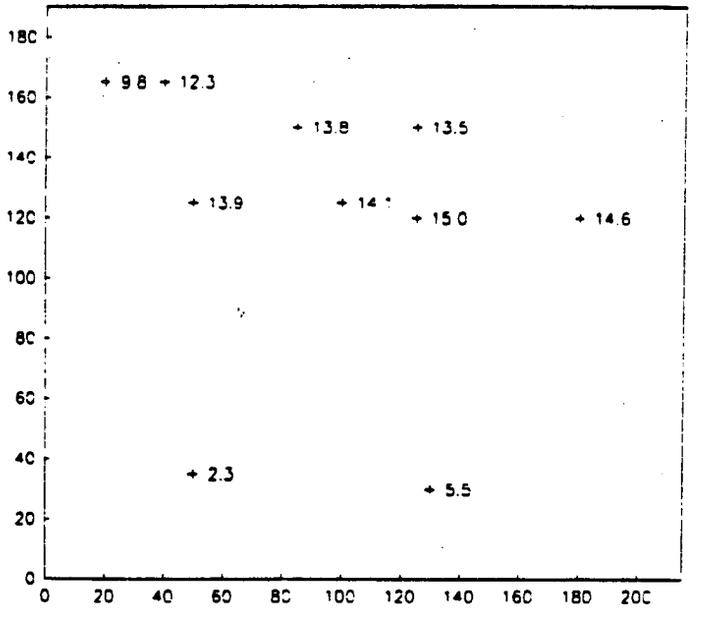

Figure 18

Inverse of the smoothed acoustic impedances

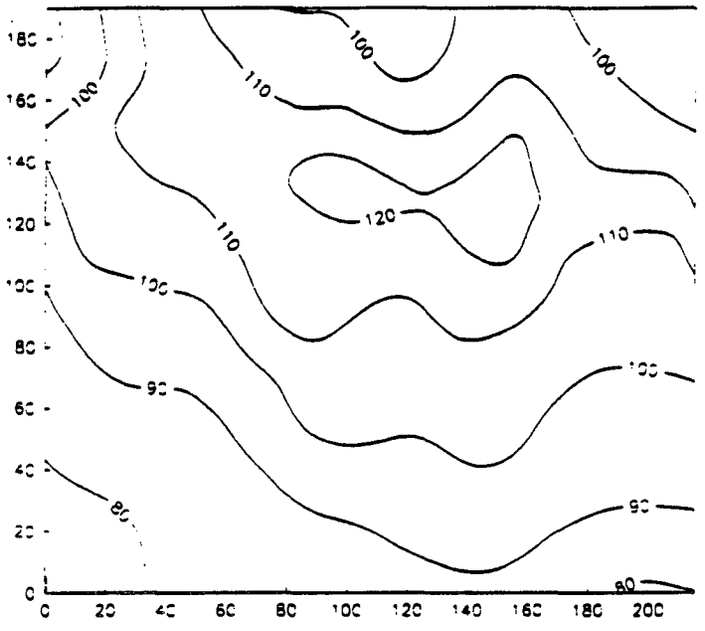

$80 \rightarrow 12500\ [grcm^{-3}\ .\ m\ \mathrm{sec}^{-1}]$

$120 \rightarrow 8500$

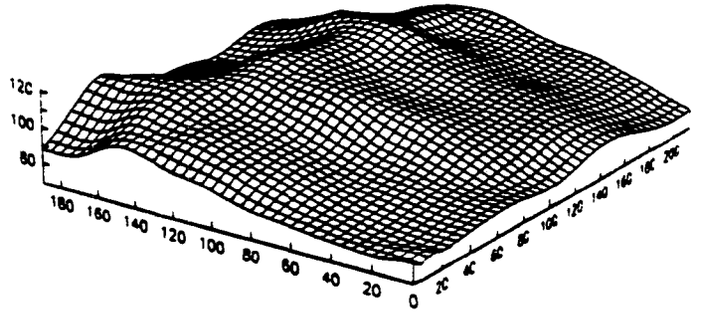

Figure 19

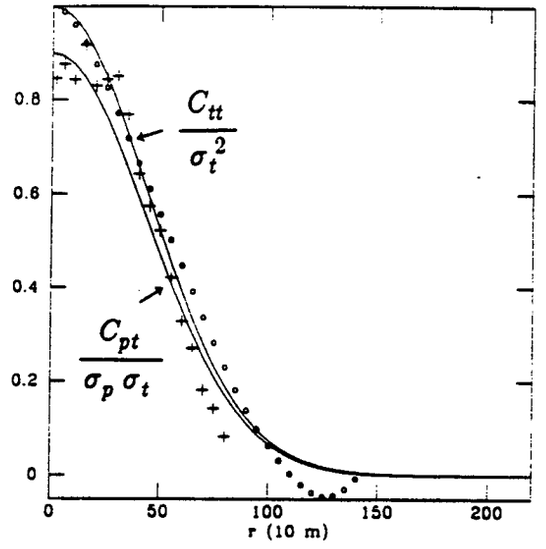

$<\epsilon^2>_{lms} = 1\%^2$

$<\epsilon^2>_{reg} = 2\%^2$

Figure 20

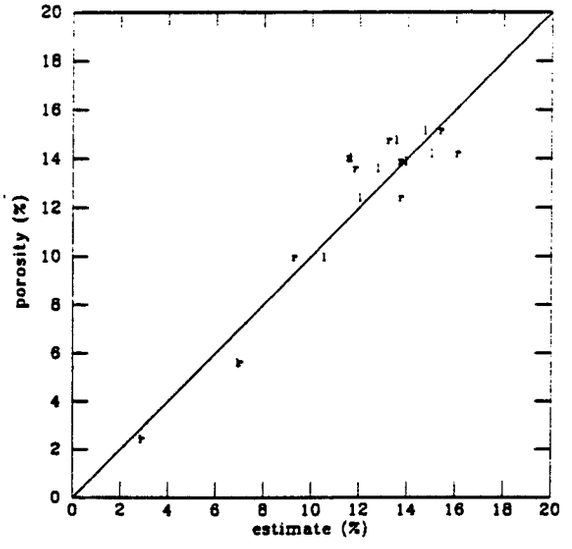

Figure 21

LMS [P]

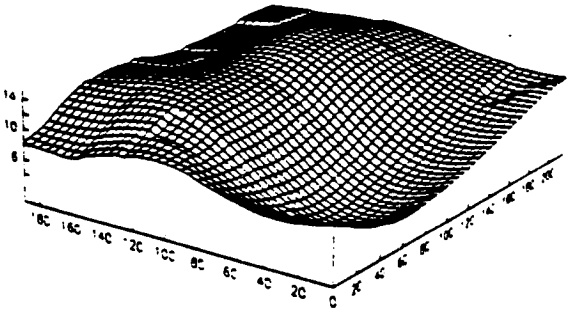

Regression [P - T (smoothed)]

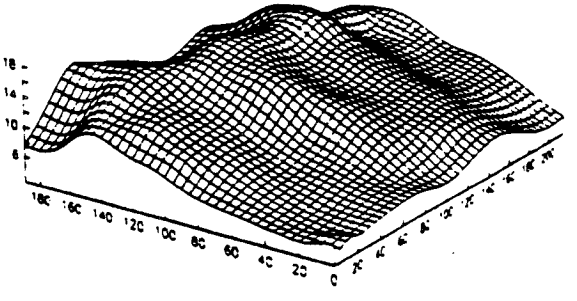

LMS [P and T (smoothed)]

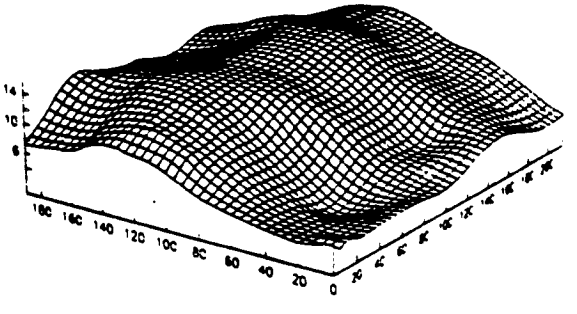

Figure 21 (cont.)

LMS [P]

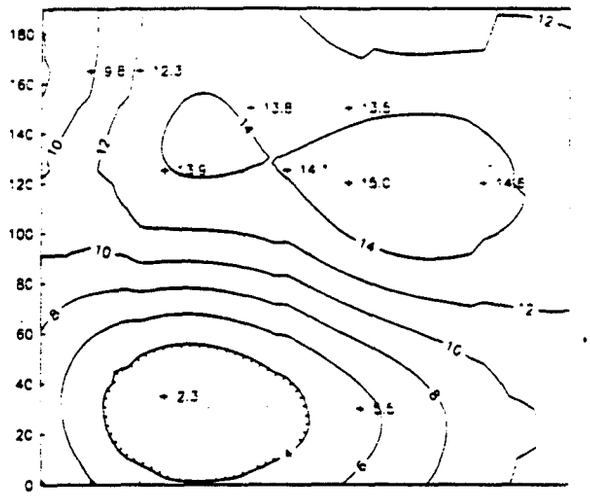

Regression [P - T]

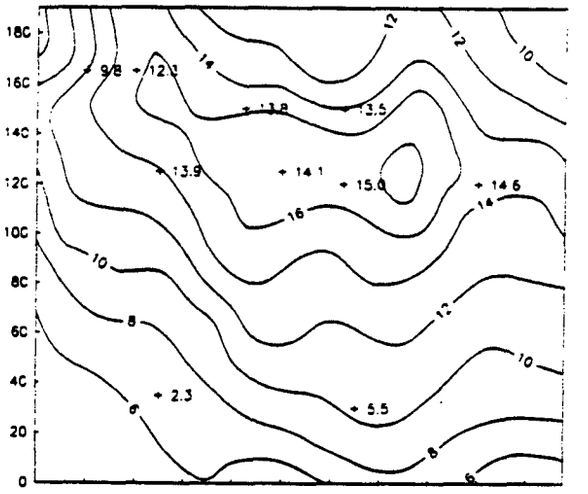

LMS [P and T]